Constraining external photoevaporative winds of proplyds with high-resolution integral field spectroscopy

Mari Liis Aru

SIGILL: UNIVERSITAT: LUDOVIC: MAXIM:

München 2025

Constraining external photoevaporative winds of proplyds with high-resolution integral field spectroscopy

Mari Liis Aru

Dissertation
an der Fakultät für Physik
der Ludwig–Maximilians–Universität
München

vorgelegt von
Mari Liis Aru
aus Tallinn, Estland

München, den 11. September 2025

Erstgutachter: Prof. Dr. Barbara Ercolano
Zweitgutachter: Prof. Dr. Tilman Birnstiel
Tag der mündlichen Prüfung: 27. Oktober 2025

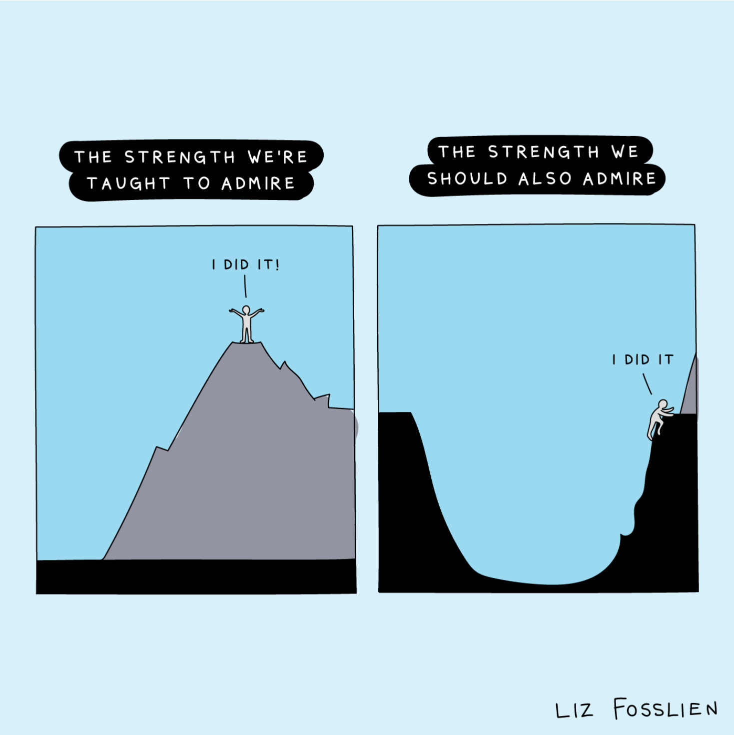

To those who rise from the valleys of loss and grief.
Neile, kes on kaotuse ja leina sügavikest jalule tõusnud.

Armsa M.'i mälestuses

This work was carried out at the European Southern Observatory (ESO) in Garching bei München under the supervision of Carlo Manara, as part of the European Research Council (ERC) funded WANDA project 101039452, and additional support from Karina Maucó.

Contents

List of Figures

List of Tables

Zusammenfassung

Astronomen haben Tausende von Planeten jenseits unseres Sonnensystems entdeckt – Exoplaneten, die äußerst vielfältige Planetensysteme bevölkern. Um den Ursprung solcher Systeme zu verstehen, wenden wir uns den protoplanetaren Scheiben zu, rotierenden Strukturen aus Gas und Staub, die das Grundmaterial für Planeten bereitstellen. Protoplanetare Scheiben entstehen als Folge des Sternentstehungsprozesses und umgeben junge Sterne aufgrund der Erhaltung des Drehimpulses in Form einer Scheibe. Mehrere Prozesse beeinflussen, wie sich die Scheiben im Laufe der Zeit entwickeln. Innerhalb des Systems können energiereiche Photonen des Zentralsterns photoevaporative Winde antreiben, während Magnetfelder, die die Scheibe durchziehen, magnetohydrodynamische Winde auslösen können. Diese Mechanismen wurden in nahen Sternentstehungsgebieten eingehend untersucht. Allerdings entstehen Scheiben selten isoliert. In massereichen Sternhaufen erhitzen UV-Photonen von OB-Sternen das Gas in den äußeren Regionen der Scheiben und führen zu einem Abbau der Scheibe von außen nach innen. Dieser extern photoevaporative Wind beeinflusst Größe, Masse und Lebensdauer protoplanetarer Scheiben. Inzwischen gilt es als wahrscheinlich, dass die meisten Sterne in Haufen entstehen, und Hinweise deuten darauf hin, dass auch die Sonne in einer solchen Umgebung geboren wurde. Externe Photoevaporation ist daher eine Schlüsselingredienz in Modellen der Planetenentstehung.

Bis vor Kurzem wurden dieselben Beobachtungsdiagnostiken verwendet, um sowohl intern als auch extern angetriebene photoevaporative Winde zu untersuchen. In dieser Arbeit beabsichtige ich, die beiden Typen von Winden zu unterscheiden, indem ich hochinformative und neuartige Beobachtungen von extern bestrahlten Scheiben, sogenannten Proplyds, im Orionnebelhaufen (ONC) analysiere – dem nächstgelegenen Sternhaufen mit massereichen Sternen. Proplyds werden zwar bereits seit den 1990er-Jahren untersucht, doch die Integral-Feld-Spektroskopie bringt etwas Neues: Informationen über ein Zielobjekt werden nicht nur in einem Band oder bei einer Wellenlänge gesammelt (wie es bei Bildgebung oder einfacher Spektroskopie der Fall ist), sondern über ein gesamtes Wellenlängenspektrum hinweg.

Basierend auf Daten des MUSE-Integral-Feld-Spektrographen mit adaptiver Optik präsentiere ich die Morphologie der Proplyds im optischen Bereich, wobei eine Vielzahl von Elementen und deren Ionisationszuständen abgedeckt wird. Zunächst habe ich die Radien der Ionisationsfronten gemessen und gezeigt, wie die Schichten des ionisierten Sauerstoffs geschichtet sind. Auch Obergrenzen für die Massenverlustraten wurden abgeleitet, die mit bisherigen Beobachtungsschätzungen übereinstimmen. Anschließend stellte ich die verbotene Linie des neutralen Kohlenstoffs [C i],8727 Å als diagnostisches Mittel für externe Photoevaporation vor. Erstmals wurde ihre räumliche Verteilung mit [O i]-Linien und ALMA-Kontinuumemission verglichen, wobei sich zeigte, dass die [C i]-Emission mit der Scheibe kospatiell ist. Das Fehlen der Kohlenstofflinie in isolierten Scheiben, im Gegensatz zur allgegenwärtigen Detektion der [O i]-Linien, stützt ihre Rolle als deutlicher Indikator für extern angetriebene Winde. Schließlich erweiterte ich die Analyse auf häufig beobachtete verbotene Linienverhältnisse und wandte dabei eine verfeinerte Methode der Hintergrundsubtraktion an. Unter diesen erwies sich das [N ii]/[S ii]-Verhältnis als besonders robuster diagnostischer Indikator für externe Photoevaporation. Während MUSE allgemeine Einschränkungen zur Temperatur und Elektronendichte der Proplyds ermöglicht, wäre ein breiteres Wellenlängenspektrum im kürzeren Bereich noch aufschlussreicher.

Insgesamt etablieren diese Ergebnisse neue Tracer, die eindeutig für externe Photoevaporation stehen. Die vorgestellten Beobachtungen liefern Referenzwerte für bestehende Modelle und treiben zugleich die Entwicklung neuer Modelle voran, die externe Winde und deren Signaturen in die Scheibenevolution einbeziehen. Die Etablierung dieser Diagnostiken im ONC legt das Fundament für zukünftige Studien in massereicheren und weiter entfernten Haufen, in denen Scheibenmorphologien nicht räumlich aufgelöst werden können und in denen externe Photoevaporation voraussichtlich eine zentrale Rolle spielt.

Abstract

Astronomers have discovered thousands of planets beyond our solar system—exoplanets, which populate planetary systems of great diversity. To understand the origin of such systems, we look to protoplanetary disks, rotating structures of gas and dust that provide the foundational material for planets. Protoplanetary disks emerge as a consequence of the star formation process, surrounding young stars in the shape of a disk due to angular momentum conservation. Several processes influence how the disks evolve in time.

Internally to the system, high-energy photons from the central star can drive photoevaporative winds, while magnetic fields threading the disk can launch magneto-hydrodynamic winds. These mechanisms have been studied thoroughly in nearby star-forming regions. However, disks rarely form in isolation. In massive star clusters, UV photons from OB-type stars heat the gas of the disk outer regions, depleting the disk outside-in. This externally photoevaporative wind influences the size, mass, and lifetime of protoplanetary discs. It is now considered that most stars form in clusters, and evidence points this also as the birth environment of the Sun. External photoevaporation is therefore a key ingredient in planet formation models.

Until recently, the same observational diagnostics have been used for studying both internally and externally driven photoevaporative winds. The aim of this thesis is to disentangle the two types of winds by analyzing highly informative and novel observations of externally irradiated disks known as proplyds in the Orion Nebula Cluster (ONC), the closest cluster with massive stars. Whereas proplyds have been studied since the 1990s, integral field spectroscopy introduces novelty: information about a target is not gathered in one band or wavelength (as is the case with imaging and spectroscopy alone), but across an entire wavelength range.

Based on data from the MUSE adaptive optics-enabled integral field spectrograph, this thesis presents the morphology of proplyds in the optical, covering a variety of elements and their ionization states. First, the ionization front radii were measured, and the stratification of the ionized oxygen layers was demonstrated. The upper limits of mass-loss rates were also derived, consistent with previous observational estimates. Secondly, the forbidden line of neutral carbon [C I] 8727 Å was presented as a diagnostic of external photoevaporation. For the first time, its spatial distribution was compared with [O I] lines and ALMA continuum emission, showing that the [C I] emission is co-spatial with the disk. The absence of the carbon line in isolated disks, in contrast with the ubiquitous detection of [O I] lines, supports its role as a tell-tale tracer of externally driven winds. Finally, the analysis was extended to commonly observed forbidden-line ratios, using a refined background-subtraction method. Among these, the [N II]/[S II] ratio emerged as a particularly robust diagnostic of external photoevaporation. While MUSE allows to put general constraints on the temperature and electron density of proplyds, a wider range in shorter wavelengths would be more informative.

Together, these results establish new tracers uniquely for external photoevaporation. The presented observations provide benchmarks for existing models, and also drive the development of new models that incorporate external winds and its signatures into disk evolution. Establishing these diagnostics in the ONC sets the foundation for future studies in more massive and distant clusters, where disk morphologies cannot be spatially resolved, and where external photoevaporation is expected to play a central role.

Kokkuvõte

Astronoomid on avastanud tuhandeid eksoplaneete ehk planeete, mis tiirlevad muude tähtede ümber kui Päike. Tuvastatud eksoplaneedid kuuluvad Päikesesüsteemiga võrreldes väga erinevatesse süsteemidesse: neid on ainult Maa-tüüpi planeetidega koosseisust kuni sellisteni, kus on gaasihiiud, mis tiirlevad oma ematähele ekstreemselt lähedal. Selliste süsteemide algupära aitavad selgitada vaatlused protoplanetaarsetest ketastest, mis on planeetide tekkekohad. Need on gaasist ja kosmilisest tolmust koosnevad struktuurid, mis ümbritsevad noori tähti. Mitmed protsessid mõjutavad seda, kuidas kettad arenevad ja kuidas nende materjal jaotub ning neid ümbritsevasse keskkonda hajub.

Planeeditekke-ketta keskel olev noor täht mõjutab ketast seest väljaspoole, kuumutades osakesi, kuni nad ketta pealmistest kihtidest voona vabanevad. Samuti võivad ketast läbivad magnetväljad käivitada magnetohüdrodünaamilisi vooge. Neid protsesse on põhjalikult uuritud Päikesesüsteemile kõige lähemal asuvates, molekulipilvedest tähetekkepiirkondades, kus ei leidu massiivseid tähti. Ent uued tähed ja nende kettad ei teki kõige tüüpilisemalt sellistes tingimustes, vaid täheparvedes. Viimastes kuumutavad O- ja B-tüüpi tähed ketta välimisi kihte süsteemiväliselt, tekitades materjali ärakandumist väljast sissepoole: seda nimetatakse fotoaurustumiseks. Massiivselt tähelt lähtuv ultraviolett- ehk UV-kiirgus mõjutab jätkuvalt kettast ärakanduvat gaasi, tekitades ketta ümber komeedisarnase kujuga pilve. Kirjeldatud süsteeme nimetatakse inglise keeles terminiga “proplyd” ehk propliit. Fotoaurustumise protsess kahandab ketta suurust, massi ja eluiga. Praegu peetakse tõenäoliseks, et enamik tähti tekib kõrge UV-kiirgusega keskkondades, ning uuringud viitavad, et sellistes tingimustes tekkis tõenäoliselt ka Päike. Seega on süsteemi välise tähe poolt tekkiv fotoaurustumine oluline koostisosa planeeditekke mudelites.

Kuni hiljutise ajani kasutati samu kiirgusjooni nii ematähe kui ka välise tähe poolt tekitatud fotoaurustumise uurimiseks. Antud doktoritöö eesmärk on neid kahte protsessi eraldada, analüüsides uusi informatiivseid vaatlusi planeeditekke-ketastest Orioni udukogus, mis on meile lähim massiivsete tähtedega parv. Kuigi sealseid süsteeme on uuritud juba 1990. aastatest, pakub käesolevas töös kasutatud integraalvälja spektroskoopia midagi uut: teavet ei koguta üksikutes kitsastes lainepikkuse vahemikes (nagu ainuüksi pildistamise või spektroskoopia puhul), vaid üle laia lainepikkuste vahemiku. Seeläbi on võimalik eraldada lainepikkusi, millele vastavad propliitide eri osad nagu ionisatsioonifront, ketas ja gaasipilv.

Antud töös esitlen MUSE adaptiivoptikaga varustatud integraalvälja spektrograafi andmete põhjal Orioni propliitide morfoloogiat nähtavas valguses, mis hõlmab mitmesuguseid elemente ja nende ionisatsioonitasemeid. Esiteks mõõtsin ionisatsioonifrontide raadiused ja näitasin, kuidas ioniseeritud hapnik on kihistunud vastavalt ionisatsioonitasemele. Samuti tuletasin massikao ülempiirid, mis on kooskõlas varasemate vaatluslike hinnangutega. Teiseks esitlesin neutraalse süsiniku keelatud joont [C I] 8727 Å kui välise fotoaurustumise tunnusliku märki. Töös võrreldakse esmakordselt selle joone ruumilist jaotust [O I] joonte ja ALMA vaatluste vahel, näidates, et [C I] kiirgus kattub ketta asukohaga. Süsinikujoone puudumine ketastes, mis ei asu massiivsete tähtedega piirkondades toetab selle joone rolli välise fotoaurustumise tuvastamises. Viimasena laiendasin analüüsi sagedasti kasutatavatele keelatud joonte intensiivsussuhetele, rakendades täpsustatud taustkiirguse eraldamise meetodit. Nende seas osutus [N II]/[S II] suhe täiendavaks välise fotoevaporatsiooni tunnusmärgiks. Kuigi MUSE võimaldab seada üldisi piiranguid propliitide temperatuurile ja elektronitihedusele, oleks laiema katvusega lühemates lainepikkustes saadav teave veelgi väärtuslikum.

Kokkuvõttes tagavad need tulemused uued tunnuslikud märgid sellest, et väline fotoaurustumine leiab aset, võimaldades seda eraldada protsessist ketta sisemises osas.

Esitatud vaatlused pakuvad olemasolevatele mudelitele suuniseid ning suunavad ka uute mudelite arendamist, mis hõlmavad väliseid tuuli ja nende mõju planeeditekke-ketaste arengus. Nende diagnostikate kinnistamine Orioni udukogus loob aluse tulevastele uuringutele massiivsemates ja kaugemates täheparvedes, kus propliitide struktuuri ei ole võimalik ruumiliselt lahutada ja kus väline fotoaurustumine mängib eeldatavasti keskset rolli.

1

Introduction

A beloved quote among astronomy enthusiasts asks us to pause and reflect on an image of the Earth from space, taken by the Voyager 1 spacecraft before venturing out of the Solar System: “Look again at that dot. That’s here. That’s home. That’s us.”[1] In the context of this thesis, let us turn to the Orion Nebula, visible south from the Orion’s Belt. Look again at that dot. That’s not here. That’s not us—but it could have been what our origin story looked like.

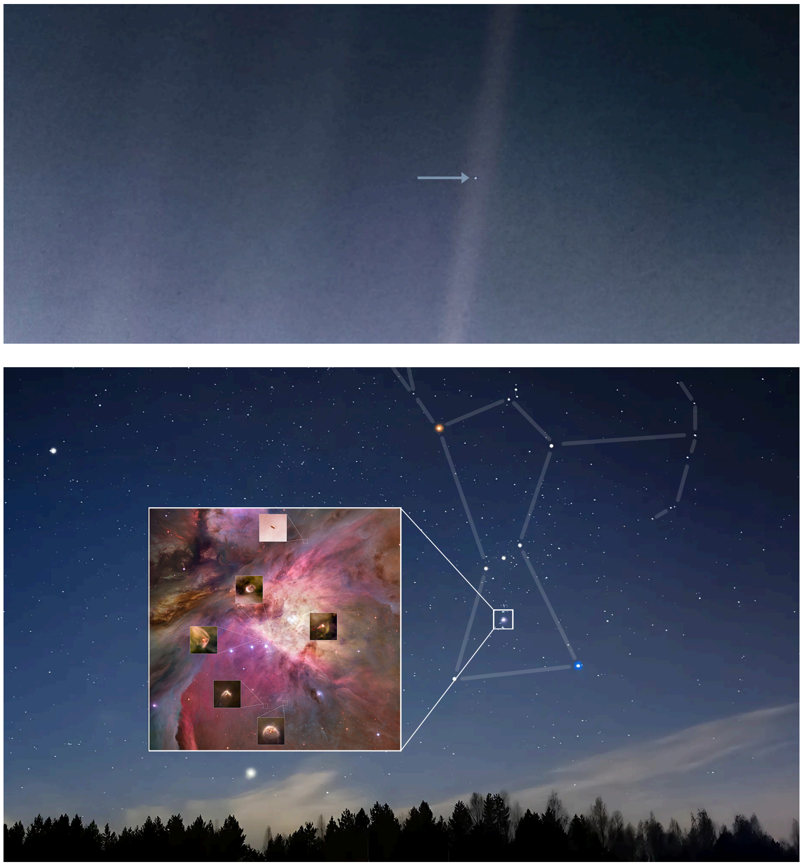

Figure 1.1: Above: Earth seen from beyond the orbit of Neptune, at ∼40 au, on 14 February 1990. Credit: NASA/JPL-Caltech. Below: The constellation of Orion with the Orion Nebula Cluster, and newly forming planetary systems marked. Background: Eerik/iStock/Getty. Inset: NASA, ESA, M. Robberto (STScI/ESA), HST Orion Treasury Project Team and L. Ricci (ESO)

---

[1] *Pale Blue Dot*, Carl Sagan

The images above illustrate how astronomy and space exploration inform us in two complementary ways. By investigating celestial objects, we can address fundamental questions such as how stars and planets form. At the same time, these studies help us understand the origin of our own home planet and its place in the Universe.

The existence of other planets within the Solar System was established centuries ago. The earliest hints of planets came from their movement, which is encapsulated in the word *planet* itself. In ancient Greek, *asteres planētai*, "wandering stars" referred to the few stars that moved differently across the night sky compared to the "fixed" stars. Over time, naked-eye observations turned into detailed analyses with increasingly powerful tools, from early telescopes to the addition of spectroscopy, and eventually to space-based observatories. With these advances, the orbital arrangement and compositions of the planets became known: rocky planets orbit close to the Sun, while gas and ice giants reside much farther out.

In the 1990s, our understanding about planets expanded beyond the Solar System. Wolszczan & Frail (1992) discovered a pair of rocky planets orbiting around a star other than the Sun—exoplanets. Whereas the pair orbited a rapidly spinning pulsar[2], the first known exoplanet to orbit around a star like our own was discovered shortly afterwards (Mayor & Queloz 1995). Since then, the detection of nearly 6,000 exoplanets has been confirmed as of 2025, and the detections continue to grow rapidly[3].

The upsurge of detections is tied to dedicated surveys with an effective method in which exoplanets transit their host stars, i.e. pass directly between us as observers and the host star, periodically dimming the host star's observable brightness. These numerous discoveries revealed an impressive diversity of planetary systems. In sharp contrast to the Solar System, astronomers found many Jupiter-type exoplanets orbiting extremely close to their stars. To this day, these findings challenge the theories of planet formation, traditionally built on the basis of the Solar System.

To understand the planet formation process and its diverse outcomes, we need to turn to protoplanetary disks, the birthplaces of planets. These disks are composed of gas (mostly hydrogen and helium) and dust grains, and arise during star formation: the material remaining from the formation of a protostar settles into orbit and flattens into a rotating disk. The star and planet formation processes are therefore closely connected.

Although some stars and planets form in isolation, most new stars form in clusters, i.e., stellar groupings, where other, massive stars emit powerful (ultraviolet) light. The light of the massive star is energetic enough to erode the protoplanetary disks in a process called external photoevaporation. This way, some of the material available for the planets is removed from the disk, therefore influencing how and where planets can form.

The first direct observations of protoplanetary disks were made in the early 1990s in a setting just like that: the Orion Nebula Cluster (ONC). The Hubble Space Telescope (HST) observations showed objects nearby the most massive star of the cluster, and revealed their nature: disks surrounded by a cloud of ionized gas, often with a droplet- or comet-like shape. These objects became known as *proplyds* for "PROtoPLanetarY DiskS".

This thesis draws on a new development in the study of proplyds: integral field spectroscopy.

---

[2] Pulsars are extremely dense remnants of stars that emit radio waves at regular intervals.

[3] See the Exoplanet Archive for the latest count: https://exoplanetarchive.ipac.caltech.edu/

In this chapter, I summarize the key concepts relevant to this work, and describe the role of this thesis in the context of external photoevaporation studies, and star and planet formation in general.

1.1 Protoplanetary disks and their lifetime

Protoplanetary disks, composed of gas and dust, emerge as a result of the star formation process and surround young stars in the shape of a disk due to angular momentum conservation. In the early observations, disks were not spatially resolved: their presence was inferred by investigating the spectral energy distribution (SED) of embedded young stellar objects in the infrared (Lada 1987). In particular, the observed SEDs became quantified by their spectral indices $\alpha = d\log(\lambda F_\lambda)/d\log(\lambda)$ in the infrared ($\sim 2-25\,\mu$m). The different types of SEDs led the way to divide star and planet formation into four simplified classes, which begin with a protostar forming through the gravitational collapse of a prestellar core in a massive (M$\sim$ 10^4–$10^{6.5}$ M$_\odot$) and cold (T$_{gas}$ $\sim$ 10–40 K) molecular cloud. The classes and their corresponding SEDs are illustrated in Figure 1.2.

- Class 0. When a protostar has newly formed, it is embedded inside an envelope, which can be observed at sub-mm wavelengths. We can deduce the presence of the protostar itself only indirectly via jets and outflows that arise as a consequence of the material accreting onto the star from the parental envelope.
- Class I. As the material from the envelope continues to accrete onto the protostar, the optical depth of the envelope decreases. An infrared excess with respect to the black-body spectrum (expected from the stellar effective temperature) can be observed due to the gas and dust in the disk and envelope. Although the dust is expected to make up only 1% of the circumstellar material, it is the main contributor to the infrared emission.
- Class II. Once the envelope is dissipated, the emission of the central star can be observed at optical wavelengths, and the presence of a protoplanetary disk can be inferred via an infrared excess (which is smaller than at Class I).
- Class III. At this stage, the protoplanetary disk has dissipated and planets have formed. The SED shape becomes dominated by the emission from the photosphere of the pre-main sequence star.

In addition, inter-Class objects, transition disks, became known through the observation of a dip in some SEDs. These objects were initially suggested to be a transitional stage between the Class II and III stages (e.g., Skrutskie et al. 1990; Calvet et al. 2002), but subsequent observations proved them to be more nuanced (reviewed by van der Marel 2023).

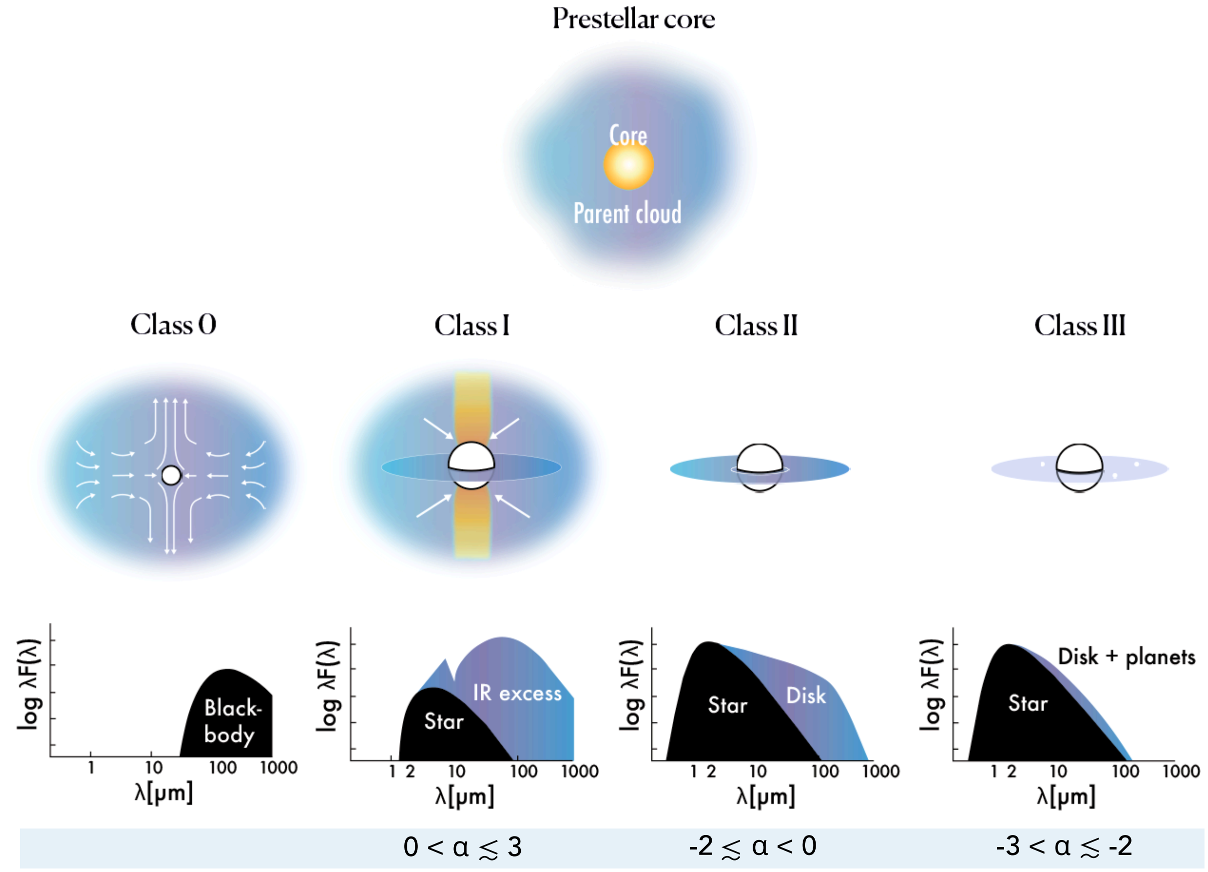

Figure 1.2: Classification scheme of young stars and the corresponding SEDs. Illustrations are not to scale. Credit: S. Brophy Lee, adapted from André (2002) and Persson (2014).

Traditionally, the Classes were tied to ages: e.g., Class 0 objects were assumed to be younger than 0.1 Myr, and Class I between 0.1 and 0.5 Myr (building on works of e.g., Greene et al. 1994; Evans et al. 2009), and Class II between 0.5 and 5 Myr (e.g., Mamajek et al. 2009). While these timescales provide a convenient framework, mapping the Classes 0–III onto an evolutionary timeline has turned out to be more complex.
Firstly, the substructures within the disk, such as cavities, are not necessarily exhibited in the SED. High-resolution observations revealed rings, gaps and other substructures already in Class I and young Class II objects, which challenged traditional models of planet formation (ALMA Partnership et al. 2015; Andrews et al. 2018). Understanding the origin of the substructures is an ongoing effort (Bae et al. 2023, for a review).
Secondly, the local environment of a disk introduces limitations for interpreting its SED. In some cases, disks may be replenished by infalling material from the surrounding molecular cloud. As a result, the observed SED may appear as an earlier Class than the true evolutionary stage of the source: Kuffmeier et al. (2023) demonstrated that a Class II object can be misclassified as Class I, or even Class 0.

To assess disk evolution and lifetimes statistically, Haisch et al. (2001) carried out an imaging survey in L-band (3.4 μm) in six nearby young clusters with mean ages 0.3–30 Myr. They presented that the fractions of disks, which they estimated based on L-band excess emission, decreased with the cluster age. About half the disks disappeared by ~3 Myr, and nearly all by ~6 Myr. This pioneering method was adopted by a number of studies for more clusters, expanding the age range. The reported disk lifetimes span from 1–3 Myr (e.g., Hernandez et al. 2007; Mamajek et al. 2009; Ribas et al. 2014) to as long as 5–10 Myr (Michel et al. 2021; Pfalzner & Dincer 2024). This spread may be explained by several factors. Evidence emerged that the lifetimes depend on the mass of the host star, with higher mass stars losing their disks more quickly (e.g., Carpenter et al. 2006; Dahm & Hillenbrand 2007; Yasui et al. 2014; Ribas et al. 2015). Pfalzner et al. (2022) also suggests that the cluster sample selection may affect the outcome, with young, distant clusters potentially being prone to observational effects which lead to a bias towards high-mass stars.

To interpret these trends, it is also necessary to understand the underlying physical processes that drive disk evolution and dispersal.

Disk evolution mechanisms While it is known that accretion of material onto the central star is a principal driver of disk evolution, the physical process that governs it is under debate. There are two main frameworks: viscous evolution and magneto-hydrodynamic (MHD) wind-driven evolution (Manara et al. 2023, for a review). Whereas the viscous evolution involves the redistribution of angular momentum (Hartmann et al. 1998; Alexander et al. 2014; Ercolano & Pascucci 2017), MHD winds have been proposed as a mechanism to remove angular momentum from the disk (e.g., Lesur 2021). The main mechanism that drives the evolution of disks remains under debate.

Disk dispersal mechanisms Importantly for the context of this thesis, it is also debated which process governs the dispersal of the disks (Alexander et al. 2014; Pascucci et al. 2023, for a review). The central star influences the innermost part of the disk (up to about 5 au), and gives rise to internally photoevaporative winds (see Sect. 1.3.2).

In addition to the influence of the central star, cluster environments introduce the radiation from massive stars (external to the young stellar objects), which affects the outer disk. Several studies observed disk fractions across clusters with several O-type stars, and demonstrated that the fraction of disk-hosting stars decreases in higher UV field strength (Stolte et al. 2004; Fang et al. 2012; Guarcello et al. 2023). Next, we look into these different conditions in which planetary systems can emerge.

1.2 Birth environments of stars and planets

Molecular clouds, rich in H_2, form in the interstellar medium from diffuse gas. Several mechanisms have been proposed for the initiation of cloud formation, such as converging flows driven by stellar feedback or turbulence, agglomeration of smaller clouds, gravitational instability and magnetogravitational instability. These processes can create density enhancements of varying spatial and mass scales, and lead to different cloud properties (e.g., Dobbs et al. 2014, for a review).

Within these molecular clouds, star formation occurs in density concentrations. In giant molecular clouds, stellar clusters are born when many stars form in proximity, nearly simultaneously (e.g., Krumholz et al. 2019). The distribution of stellar masses within these clusters is described by the initial mass function (IMF) (Kroupa 2000, for a review). The IMF follows a log-normal distribution, peaking at 0.3 $M_\odot$, with progressively fewer stars at higher masses. While most of the total stellar mass resides in numerous low-mass stars, the luminosity is contributed by the comparatively rare massive stars.

In stellar clusters, newly-formed massive stars (>8 $M_\odot$) significantly influence their environment: first through ionization and stellar winds (e.g., Matzner 2002), and eventually through supernovae explosions (e.g., McKee & Ostriker 1977). Here, we focus on the effect of photoionization. Stars emit in far ultraviolet (FUV; 6 eV $< h\nu <$ 13.6 eV), extreme ultraviolet (EUV; 13.6 eV $< h\nu <$ 100 eV), and X-ray ($h\nu >$ 100 eV) regimes. The EUV photons ionize the surrounding matter—i.e., the atoms or molecules of neutral matter gain or lose an electron by interacting with light to form an ion, which creates an H ɪɪ region. The hot ($T \approx 10^4 K$) ionized gas expands into the surrounding neutral matter as it travels at sound speed. On a smaller scale, photoionization leads to the heating and eroding the outer disk material of protoplanetary disks (Sect. 1.3.3). On a larger scale, it can break down star-forming cloud clumps, hindering star formation as a consequence. On the other hand, the shocks incident on neutral gas clouds could lead them to gravitationally collapse and trigger star formation (e.g., Elmegreen & Lada 1977; Gorti & Hollenbach 2002). At the borders of illuminated clouds, photodissociation regions (also known as photon-dominated regions; PDRs) appear (Tielens et al. 1993). In PDRs, UV photons govern the temperature and chemistry of neutral interstellar gas. The feedback processes of massive stars therefore have large-scale impact, while also shaping the evolution of protoplanetary disks.

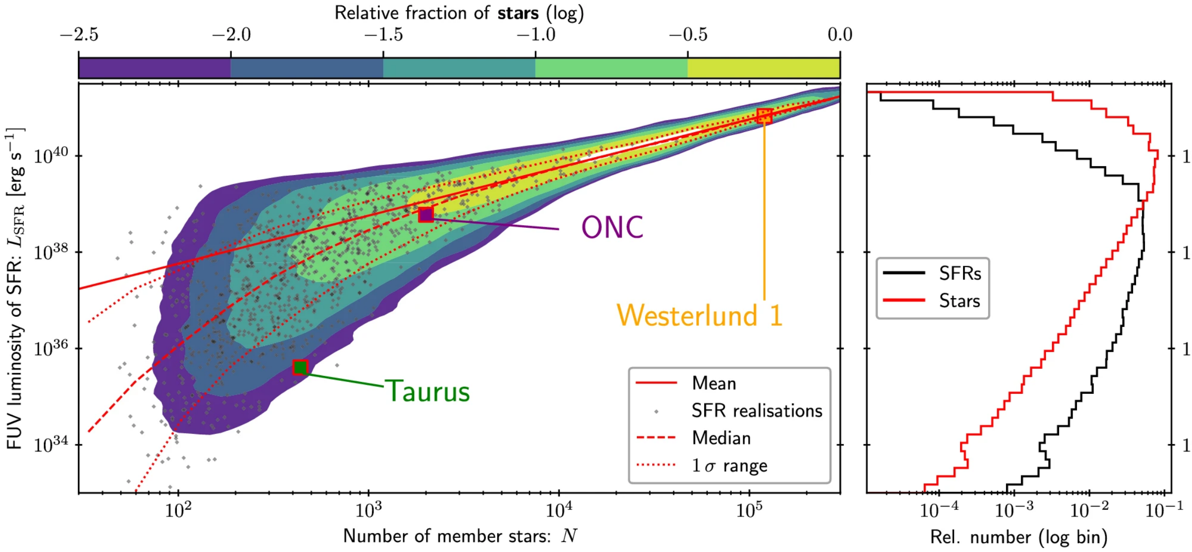

Figure 1.3: FUV luminosities at an age of 1 Myr of 6×10^4 realisations drawing star-forming regions (SFRs), with the number of members drawn from Eq. 1.2 (Winter & Haworth 2022).

Given the above, protoplanetary disks can emerge under a range of UV fluxes. To understand the typical conditions for star and planet formation, Winter & Haworth (2022) recently analyzed the distribution of the UV luminosity of SFRs experienced by their member stars. They simulated this distribution by drawing N member stars for each SFR from the Schechter (1976) function:

$$\frac{dn_{\rm SFR}}{dN} \propto N^{-\beta} \exp\left(-\frac{N}{N_{\rm max}}\right) \exp\left(-\frac{N_{\rm min}}{N}\right), \tag{1.1}$$

where $N_{min} = 280$, $N_{max} = 7 \times 10^4$, and $\beta \approx 2$ arises from the hierarchical collapse of molecular clouds (Elmegreen & Falgarone 1996). The equation was coupled with the stellar mass dependent luminosity:

$$\langle L_{\rm SFR} \rangle = N \langle L \rangle = N \int \frac{dn}{d \log m_*} \cdot L(m_*)\, d \log m_*, \tag{1.2}$$

where L is the luminosity of a single star, m_* is its mass. The resulting distribution is shown in Fig. 1.3.

The low-UV, low-density portion of Fig. 1.3 corresponds to nearby SFRs such as Taurus, Lupus, and Chameleon, located at distances of d ~150–200 pc and hosting a few hundred members. For example, in Taurus, the local luminosity is dominated by four B-type and three A-type stars, despite the total population of 438 members (Luhman 2018).

The closest region of massive star formation is the ONC at ~400 pc with an estimated total UV luminosity of $\sim 10^{38}$ erg s^{-1}, which is dominated by the O-type star θ^1 Ori C; more details follow in Sect. 1.2.2. The number of members in a cluster reach to 10^5 in starburst clusters such as Westerlund 1 at d~ 4 kpc (Navarete et al. 2022), with its FUV luminosity being $\sim 10^{40}$erg s^{-1} at a 1 Myr-age.

Although the protoplanetary disks in Taurus are the best studied cases due to their proximity to the Sun, Fig. 1.3 shows that such regions are uncommon environments of star formation with respect to the UV luminosity. It is therefore important to understand star and planet formation better in clusters—further motivated by the evidence that this was the type of environment where the Solar System may have formed, summarized in the next section.

1.2.1 Solar System formation

Which conditions gave rise to the Solar System? Several aspects aid us in reconstructing the solar birth environment and point to the influence of a clustered environment, described briefly as follows (largely based on the detailed reviews by Adams 2010; Pfalzner et al. 2015; for a comprehensive recent review, see Morbidelli et al. 2024).

Orbital evidence and the sharp edges of the Solar System From the solar protoplanetary disk, a substantial number of planets emerged: now ordered with the rocky, terrestrial planets near the Sun and the gas giant planets in the outer regions. The outermost planet Neptune orbits at a semi-major axis of about 30 au. The orbits of the planets are all nearly in the same plane of the Solar System; with inclinations $\Delta i \leq 3.5^\circ$ and eccentricities $e \leq 0.2$.
Extending from the orbit of Neptune up to a distance of about 50 au, we find the Kuiper Belt. The distant, rocky objects of the Kuiper belt are numerous but their total mass is estimated to be low (Bernstein et al. 2004), and their orbits as a group have much larger eccentricities and inclination angles than those of the planetary orbits (Luu & Jewitt 2002).
The properties above constrain the size of the protoplanetary disk from which the Solar System formed. The distinct zones suggest that the planetary orbits were not perturbed after the giant planets had formed, whereas the outward regions experienced external influences. In particular, a dwarf planet with an unusual orbit—Sedna—resides well beyond the Kuiper belt with an eccentricity of 0.84 (Brown et al. 2004). Such a high value has been estimated by numerical models to result from a stellar encounter, that is, an approach made by a passing star. The estimates for the approach distance vary depending on the model. Studies suggest that this stellar encounter and the resulting orbital elements of Sedna could be explained by a birth cluster of size $N \approx 10^3 - 10^4$ (Brasser et al. 2006). The orbit of Sedna has further been used to deduce an upper limit of 10^5 $M_\odot \mathrm{pc}^{-3}$ for the central density of the cluster (Schwamb et al. 2010). Another way to estimate the upper limit comes from the extent of the Solar Systems planets and their unperturbed orbits.

Meteoritic samples: radioactive isotopes Meteorites provide one of the most instructive evidence for reconstructing the timeline of Solar System formation. Meteoritic samples essentially act as a time capsule, as their age can be calculated through radiometric dating. The technique is based on measuring the excesses of specific daughter isotopes, produced by the decay of parent isotopes, whose half-lives are known. In chondrite meteorites, light-colored, millimeter- to centimeter-sized specks are trapped, known as calcium-aluminum–rich inclusions (CAIs). These objects contain isotopic evidence of short-lived radionuclides ^{26}Al and ^{60}Fe (half-lives of a few million years), which are produced either externally—in supernova explosions and evolved stars, or by internal irradiation processes. It has been suggested that the early solar nebula was likely enriched by these methods. Curiously, the abundance of ^{26}Al is high, ^{26}Al/^{27}Al= $4.5-5.2\times10^{-5}$, compared to the Galactic background (MacPherson et al. 1995; Jacobsen et al. 2008). At the same time, the abundance of ^{60}Fe is much lower; ^{60}Fe/^{56}Fe= $3.8 \pm 6.9 \times 10^{-5}$ (Trappitsch et al. 2018).

Several different chains of events have been proposed to explain the cosmochemical evidence and the injection of the nuclei to the solar nebula, including an early pre-solar enrichment through a Wolf-Rayet star and its subsequent supernova — from early works (Dearborn & Blake 1988) to more recent (Dwarkadas et al. 2017). Given this scenario, the number of member stars is placed on the order of $N \approx 10^3$ (e.g., Gounelle & Meynet 2012). However, Portegies Zwart (2019) argue that the scenario above would lead to an anomalously high abundance in ^{60}Fe. They suggest that at least two supernovae are needed to explain the observed characteristics of the Solar System, and estimate that clusters which are most likely to form a solar system analog contain $N = 2500 \pm 300$ stars ($\sim$900 $M_\odot$).

Here, it is fitting to note that CAIs have been dated based on both the short-lived aluminum - magnesium ^{26}Al-^{26}Mg chronology, and a long-lived radioisotope system, a lead-lead (Pb-Pb) isotope chronometer. In the latter, two isotopes of uranium decay in a chain to stable lead isotopes. The Pb-Pb method yields an age of 4567.30 ± 0.16 million years (Connelly et al. 2012), with a re-evaluated age of 4568.7 million years based on unified Al-Mg and Pb-Pb chronology (Piralla et al. 2023). This value of approximately 4.5 billion years is interpreted as the age of the Solar System.

In addition to the above, several isotopic and compositional signatures point specifically to an environment with intense UV flux:

- **^{15}N enrichment:** Measurements of primitive meteorites and cometary material reveal their enrichment in ^{15}N compared to the Sun. Such fractionation is difficult to reproduce without UV photodissociation of N_2, requiring exposure to a strong ultraviolet radiation field (Chakraborty et al. 2014; Füri & Marty 2015; Cordiner et al. 2024).

- **Oxygen isotopes:** An unusual distribution of oxygen isotopes ^{16}O, ^{17}O, and ^{18}O in primitive meteorites (CAIs and chondrules) compared to the terrestrial material. This oxygen isotope anomaly has been attributed to the dissociation of CO molecules in externally irradiated regions, altering the isotopic composition of the remaining oxygen reservoir (Yurimoto & Kuramoto 2004; Lyons & Young 2005; Young 2007).

- **Abundances in Jupiter's atmosphere:** Using the *in situ* atmospheric measurements of Jupiter by the *Galileo* probe, an enrichment of noble gases (Ar, Kr and Xe) was found, by a factor of $\sim$3 compared to the solar composition relative to H. This pattern suggests inward drift of icy grains that had been processed in the UV-irradiated outer disk, together with mass loss driven by strong photoevaporation (e.g., Guillot & Hueso 2006; Monga & Desch 2014).

These independent lines of evidence point to the influence of a clustered environment, which was likely to have enriched and sculpted the emergent Solar System. According to the estimates, the formation took place in a cluster with a typical lower limit of 1000 member stars. To substantiate these findings, the effects of clusters on forming planetary systems must be assessed statistically. The observations of protoplanetary disks beyond the Solar System allow us to investigate the initial conditions for planet formation, and move towards establishing the probability distributions for the various processes at work. This framework motivates studies of protoplanetary disks in clusters, and in particular the Trapezium Cluster in Orion, which provides the closest analog to the Sun's birth cluster.

1.2.2 Orion Nebula Cluster

The Orion Nebula is found in the south of Orion's Belt in the constellation of Orion. It extends over 1° in the sky, while being part of the much larger Orion Molecular Cloud complex (Fig. 1.4). It is a remarkable target for observations, providing a rich factory of star formation at its various stages while located at a relatively convenient distance. The Orion region has numerous subgroups; their ages and location hint that star formation has propagated through the proto-Orion cloud sequentially (Bally 2008). Indeed, Beccari et al. (2017) and Jerabkova et al. (2019) confirm three episodes of star formation, each separated in age by about 1 Myr, in area of $\sim$1.5 deg radius centered on the ONC.

The term Orion Nebula Cluster dates to Haro (1953), centering the region at the four bright OB stars — Trapezium stars. ONC is estimated to be approximately 1–3 Myr old (Da Rio et al. 2010; Reggiani et al. 2011). Its membership is estimated to be 4000 stars down to mass 0.02 $M_\odot$ (Hillenbrand & Hartmann 1998; Hillenbrand & Carpenter 2000). The true population may be considerably higher with stars potentially being obscured or staying uncounted in binary systems (Kroupa 2000). The most massive star of ONC and Trapezium is θ^1 Orionis C (shortened as θ^1 Ori C), a binary in which the primary star has a spectral class O7V and a mass of 34 $M_\odot$(Balega et al. 2015). θ^1 Ori C is ionizing part of the molecular gas within the ONC, creating a hot bubble (O'Dell et al. 2009). Proceeding in the direction toward the observer, there is a layer of ionized gas (Abel et al. 2019; O'Dell et al. 2020), followed by several layers of neutral atomic gas (collectively called the Veil; O'Dell 2001).

Structures Due to the UV light, structures such as the Orion Bar and the Orion-S cloud have formed in the ONC and can be observed in nebular emission lines. The Orion Bar is a dense (10^4 to 10^6 cm^{-3}), nearly edge-on PDR at about 2 southeast of the Trapezium, which has been extensively studied as it is referred to as the prototypical PDR (e.g., Tielens et al. 1993; Hogerheijde et al. 1995; Van der Werf et al. 1996, in the 1990s). The Orion Bar has been recently explored in unprecedented detail as part of the PDRs4All Early Release Science Program with the James Webb Space Telescope (JWST), in which NIRspec, NIRCam (Fig. 1.5), and MIRI/MRS IFU mosaics across the Orion Bar were obtained of a roughly 3" x 25" area (Berné et al. 2022; Habart et al. 2024; Peeters et al. 2024). These observations have allowed studies on various aspects of the region. Chown et al. (2024) presented an inventory of aromatic infrared bands – a rich set of emission features in the wavelength range from around 3 to 20 μm. This range also includes features of polycyclic aromatic hydrocarbons (PAHs). The study also presented mid-IR template

Figure 1.4: The Orion constellation and the surrounding nebulas of the Orion Molecular Cloud complex. Credit: Rogelio Bernal Andreo, via Wikimedia Commons, licensed under CC BY-SA 3.0.

Figure 1.5: A NIRCam view of the Orion Bar region. The brightest star here is θ^2 Orionis A, and proplyd 244-440 can be seen north-west to it. Credit: ESA/Webb, NASA, CSA, M. Zamani (ESA/Webb), the PDRs4All ERS Team

spectra from five distinct regions in the Bar: the molecular PDR, the atomic PDR, and the H II region. Van De Putte et al. (2024) identified around mid-IR 100 emission lines of various ionization and showed how certain line ratios vary between the different physical regions. Complementary studies include those carried out with Keck II telescope (Habart, Emilie et al. 2023) and ALMA (Goicoechea et al. 2025).

Distance Estimating a precise distance to the ONC has several challenges, and different methods have yielded a spread in published distances; these methods and their resulting values are reviewed in (e.g., Muench et al. 2008). Luminosity-based distance estimates face uncertainty from the spatially variable extinction within the nebula. The complex geometry and kinematics of the Orion region, plus the unclear boundaries between individual stellar subgroups further pose challenges. Several stellar subgroups of different ages have been identified, and they overlap

along the line of sight. Methods such as the comparison of radial velocities and proper motions of stars were implemented. Trigonometric parallax—the standard technique for measuring astronomical distances—was not accurate enough until the development of the very long baseline interferometry (VLBI). Menten et al. (2007b) used radio Very Long Baseline Array (VLBA) observations of four non-thermal emitting stars in the Trapezium region, placing ONC at a distance of 414 ± 7 pc. In the past decade, Kounkel et al. (2017) measured a distance of 388 ± 5 pc to the ONC as part of the Gould's Belt Distances Survey with VLBA.
The *Gaia* astrometry mission opened another era in parallax measurements. Based on *Gaia* Data Release 2, Kounkel et al. (2017) reported average distances of $d = 386 \pm 3$ pc for the ONC, and Kuhn et al. (2019) reported $d = 403^{+7}_{-6}$ pc; the latter author notes that these analyses differ in the member stars included in the studies and the corrections applied. In conclusion, while the estimation of distance to the ONC continues to be under study, the values agree with roughly 400 pc.

Proplyds In 1979, Laques & Vidal acquired optical images of an area within 10" from θ^1 Ori C with an electronographic camera (Fig. 1.6). They discovered six "knots" bright in [O III] emission. These objects of ionized gas, with more discovered in the following works, were further detected in the radio continuum (e.g., Churchwell et al. 1987), and the optical (Meaburn 1988). Two theories stemmed: either these objects are dense clumps or globules of gas and dust, or low-mass stars surrounded by evaporating disks of circumstellar material. The near-infrared observations of (McCaughrean & Stauffer 1994) settled the question by confirming that the knots had stellar counterparts.

Owing to then recently-launched Hubble Space Telescope (HST), O'Dell et al. (1993) analyzed a set of sub-arcsecond narrow-band images of a region near Trapezium and found these objects to have distinct morphology with ionization fronts, disk silhouettes, and comet-like tails pointing away from the UV source (Fig. 1.7). These objects were the first protoplanetary disks to be observed, and the authors introduced the term proplyds. The repair mission of HST was successfully performed shortly afterwards, and numerous observations of enhanced resolution followed: confirming an abundance of proplyds, surveying and cataloging them, and estimating properties such as electron densities and mass-loss rates (O'Dell & Wen 1994; Bally et al. 1998; Bally et al. 2000; O'Dell & Wong 1996; Ricci et al. 2008).

The six objects discovered by Laques & Vidal (1979) became designated as LV 1–6 in the studied that shortly followed. The numbers of detected proplyds climbed higher in the HST study O'Dell et al. (1993), with their names listed as HST 1–18. By 1998, about 150 young stellar objects had been found in the Trapezium region. As the findings continued in the confines of the Orion Nebula, proplyds eventually started to be cataloged with a coordinate-based, six-digit designation. Introduced by O'Dell & Wen (1994), the first three digits indicate the position of right ascension, and the second three correspond to the position in declination. For example, an object located at coordinates 5:35:23:12.3 and -5:27:38.9 becomes 231-739 (rounded to the closest value). In the case of multiple objects, the suffices N, S, E, W are added.

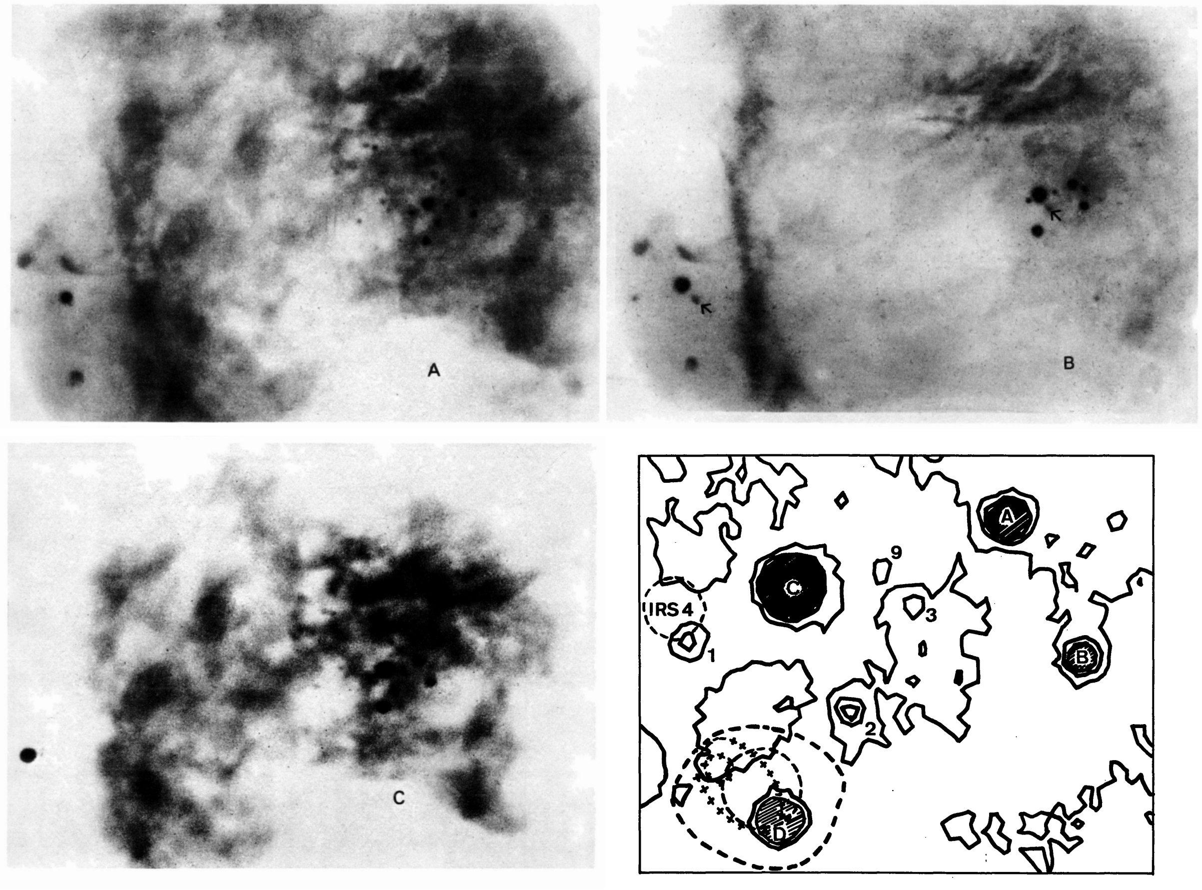

Figure 1.6: Optical images of the Trapezium taken with an electronographic camera (Laques & Vidal 1979). Image A: Hα, B: [N II] 6584 Å(the arrows point to reflections and are not the targets). C: [O III] 5007 Å. The bottom right panel is an isodensity map, where the numbers indicate the detected targets.

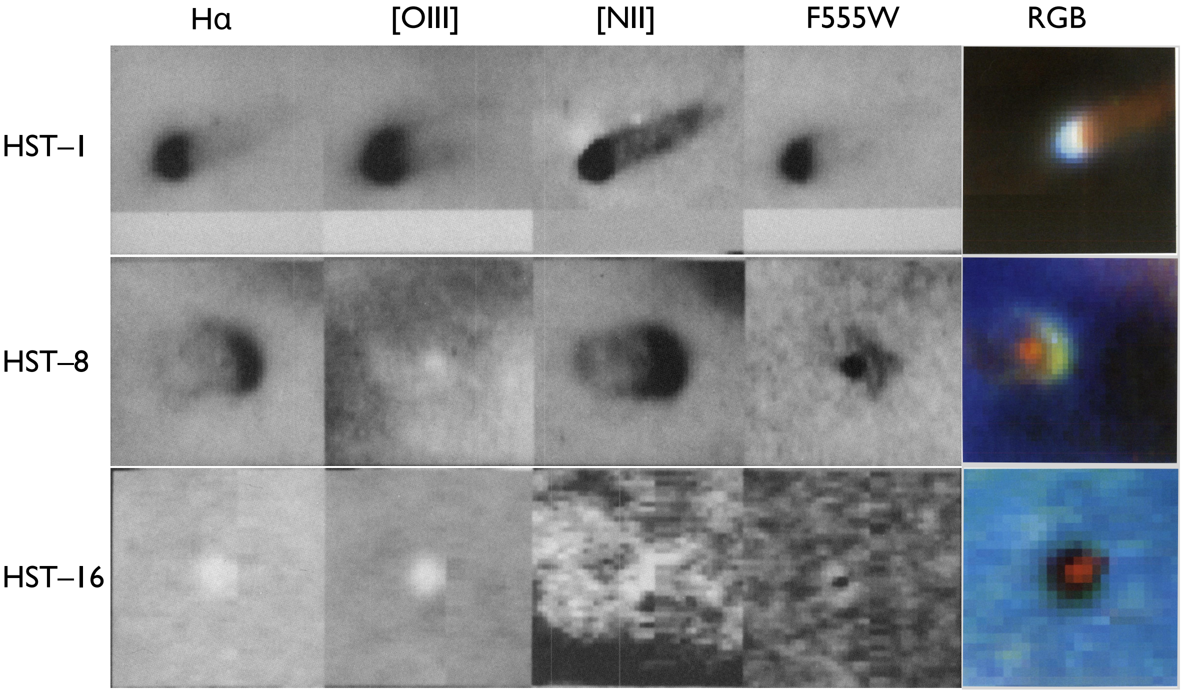

Figure 1.7: Hubble Space Telescope images of three proplyds before the telescope was refurbished; adapted from O'Dell et al. (1993).

1.3 Photoevaporative winds and their observation

The motivation for this thesis stems from the fact that thermally driven photoevaporative winds of different origin in protoplanetary disks can lead to the same emission lines. This is a setback in the study of systems that are not spatially resolved, as the underlying mechanism of the observed spectral lines cannot be determined. This ambiguity limits our ability to build reliable models of disk evolution.

As one mechanism is caused due to the radiation from the central protostar or processes brewing in disks, it is here referred to as internal wind, as opposed to the external winds driven by massive stars outside the YSO system. The following subsections first outline the mechanism of forbidden line emission, and then discuss the physical processes that drive stellar winds.

1.3.1 Forbidden emission lines

In general, emission lines are produced when an atom or a molecule undergoes a transition between discrete energy states, from upper to lower levels, and emits the excess energy as a photon: $h\nu = E_2 - E_1$. The de-excitation of an electron depends on the local particle density and the Einstein coefficient A_{21}, which quantifies the probability for a spontaneous decay from the upper level to the lower per unit time. The decay of the excited state E_2 can be described by the equations

$$\frac{dN_1}{dt} = -A_{21}N_2 \tag{1.3}$$

and

$$N_2(t) = N_2(t=0)e^{-A_{21}t} \tag{1.4}$$

The lifetime of the excited state is defined as the time in which the level population N reduces by a factor of 1/e. Hence, the lifetime can be defined as

$$\tau = \frac{1}{A_{21}} \tag{1.5}$$

Transitions with high probabilities are those that satisfy the rules for electric dipole radiation: the orbital angular momentum quantum number must change by $\Delta l = \pm 1$, and in some cases the spin quantum number by $\Delta s = \pm 1$. For these transitions, referred to as *permitted*, the excited states result in lifetimes on the order of nanoseconds. However, when the surrounding medium has a low enough density, some excited states can persist much longer, at least for seconds. These long-lived states are called metastable, and the associated transitions have very low probability, occurring through weaker mechanisms such as magnetic dipole or electric quadrupole radiation. They are denoted as *forbidden* transitions. In spectroscopic notation, forbidden lines are denoted by square brackets around the atomic species, where I designates a neutral atom and higher Roman numerals indicate successive ionization states. A prime example of environments that favor forbidden line emission are H II regions, where densities are typically only a few atoms per cubic centimeter. Additionally, their emission can be observed in nebulae, the solar corona and the Earth's aurora.

To date, forbidden emission lines are the principal tracers of both internal and external winds with optical and near-infrared spectroscopy. There are two mechanisms known to lead to forbidden line emission in a photoionized cloud. In collisional excitation, a free electron excites a bound electron through a collision, which is subsequently followed by radiative decay. Forbidden lines are emitted in this way from ions within the H II region (Osterbrock & Ferland 2006). Another mechanism is FUV pumping, wherein an excited state is reached by the absorption of FUV photons. The excited state then decays through a series of radiative transitions, i.e., de-excitation cascades (Ferland et al. 2012). A Gotrian diagram of FUV-pumped neutral carbon lines is shown in Fig. 1.8.

Forbidden line ratios are widely used to determine the electron temperature and density of H II regions, serving as diagnostic tools even without detailed modeling Osterbrock (1989); Osterbrock & Ferland (2006). The relative strengths of emission lines from the same ion, but originating from different energy levels, depend on the energy separation of those levels. Because the level populations follow a Boltzmann distribution, such line ratios are sensitive to the electron temperature and can therefore be used as its diagnostic. An example in the optical is [N II](λ6548+λ6583)/[N II] λ5755 (e.g., McLeod et al. 2015). The downward transitions from the ^1S level produces the λ5755 line, and the transition from ^1D to ^3P levels leads to the emission of the two other lines. The ratio of the line emissivities j can be expressed via the transition

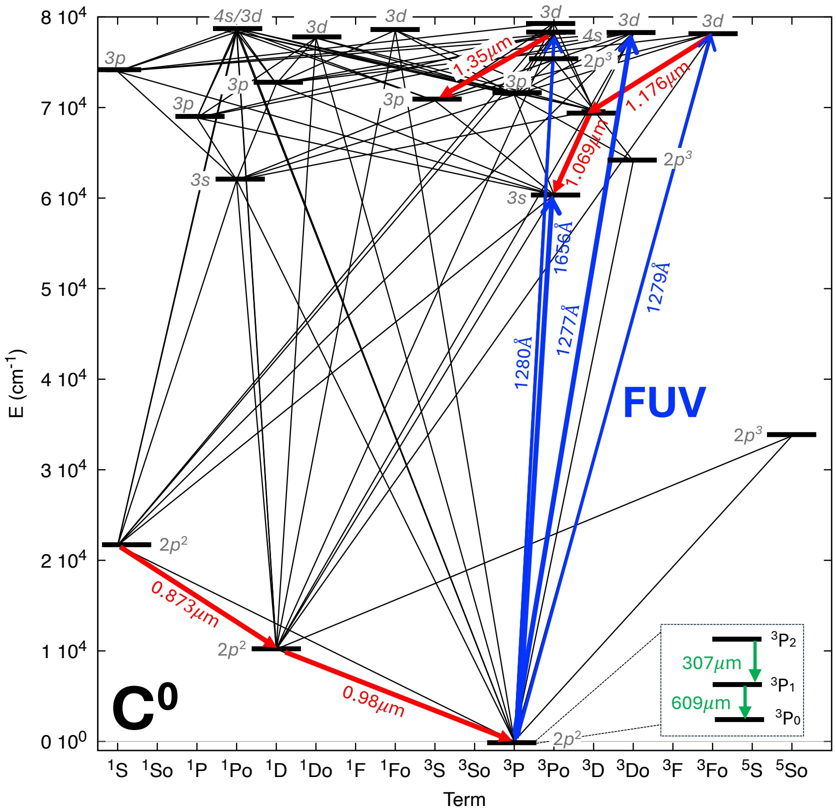

Figure 1.8: Reduced Gotrian diagram of neutral carbon, including FUV-pumping lines in blue, and the transitions through which the FUV-pumped electrons eventually decay (red) (Goicoechea et al. 2024).

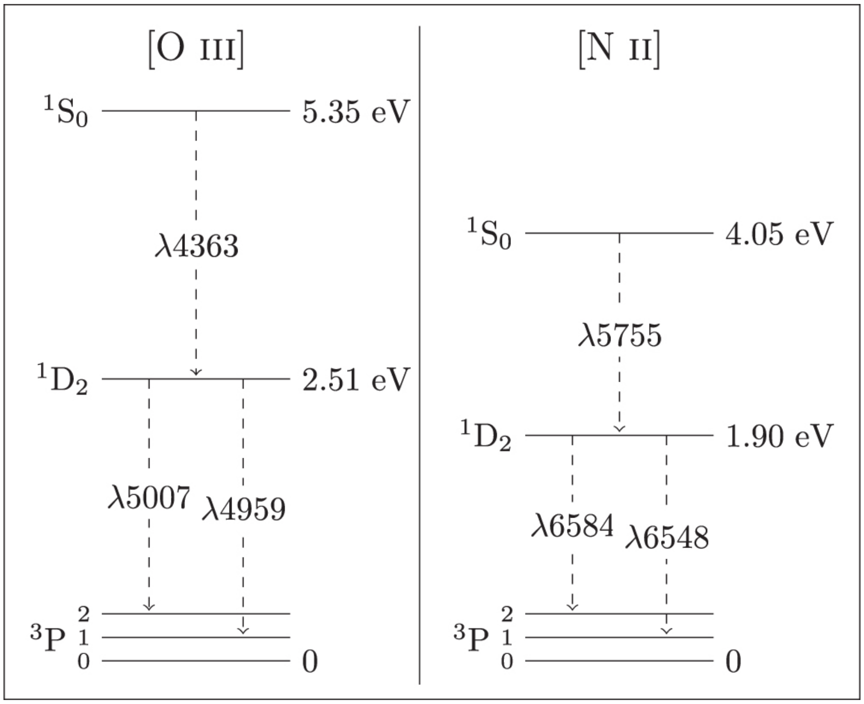

Figure 1.9: Energy-level diagram for [O III] and [N II] ions. Credit: Douglass and Vogeley (2017).

probabilities:

$$\frac{j(^1D \rightarrow {}^3P_1) + j(^1D \rightarrow {}^3P_2)}{j(^1S \rightarrow {}^1D)} = \frac{\gamma(^3P,^1D)}{\gamma(^3P,^1S)} \left[\frac{A_{1S,1D} + A_{1S,3P}}{A_{1S,1D}} \right] \frac{\bar{\nu}(^3P,^1D)}{\bar{\nu}(^1D,^1S)} e^{-h\nu/kT} \tag{1.6}$$

where γ is the collision strength corresponding to each level and $\bar{\nu}$ is the mean emission line frequency. After incorporating the numerical values, the ratio of the [N II] lines becomes

$$\frac{j_{\lambda 6548} + j_{\lambda 6583}}{j_{\lambda 5755}} = \frac{8.23\, e^{2.5\times 10^4/T}}{1 + 4.4 \times 10^{-3} n_e / T^{1/2}} \tag{1.7}$$

where n_e is the electron density. Another diagnostic ratio considered in literature is [O III]λ4959+λ5007/λ4363 (which is however out of the range in the case of MUSE studies). The energy-level diagrams for these emission lines are shown in Fig. 1.9.

On the other hand, estimating the density relies on using lines with very similar excitation potentials. That way, their relative strengths depend mainly on the ratio of their collision strengths, which is determined by the electron density through the collision cross section. This diagnostic is most effective below a threshold called *critical density*, since in that case, each collisional excitation leads to an emission. Above critical density, the downward transition by collisions occurs more quickly than radiative decay. Critical densities for selected diagnostic lines are given in Table 1.1.

Ion	λ	n_e^{crit}
[N II]	6548, 6584	9×10^4
[O II]	7318, 7329	4×10^6
[O III]	4959, 5007	7×10^5
[S II]	6717, 6731	2×10^3, 4×10^3
[S III]	6312	10^7
[Ar III]	7135	5×10^6

Table 1.1: Critical densities of diagnostic emission lines in the optical (Mesa-Delgado et al. 2012), atomic data of García-Rojas, Peña & Peimbert (2009).

1.3.2 Internal photoevaporative winds and MHD winds

The late evolution and final dispersal of (isolated) protoplanetary disks are thought to be shaped and set by the central star-driven photoevaporation (e.g., Ercolano & Pascucci 2017, for a review). In the case of internal photoevaporation, radiation from the central protostar heats the gas content of a disk inside-out, ionizing its upper layers. This process was modeled by Hollenbach et al. (1994), considering photons in the EUV regime. When UV radiation and X-rays heat the gas up to T~ $10^3 - 10^4$ K, much hotter than the disk midplane below, the sound speed of the gas becomes comparable to or exceeds the local escape speed. The corresponding characteristic length scale, also known as the gravitational radius, is (Shu et al. 1993; Hollenbach et al. 1994):

$$r_g = \frac{GM_\star}{c_s^2} = \frac{GM_\star m}{k_B T} \tag{1.8}$$

where $M_\star$ is the mass of a central star, k_B is Boltzmann constant, mass m the mean mass per gas particle, T the gas temperature at the base of the flow, and G the universal gravitational constant. Beyond this radius, thermal pressure can overcome gravitational binding energy, and the gas escapes in the outflow. This is a simplified view, as more detailed models have shown that mass loss can also occur already within the gravitational radius (Liffman 2003). A variety of models describing photoevaporation have been developed, categorized by the dominant wavelength regime: EUV heating, X-ray heating, FUV heating, and combinations of these (Alexander et al. 2014, for a review). While EUV photons are energetic enough to ionize hydrogen atoms, FUV photons are non-ionizing and H_2-dissociating. The EUV models are thus limited to the EUV-ionized layer only. To further constrain the winds, X-ray heating must be included, as X-rays are able to pierce larger columns of neutral material.

The models differ not only in the heating mechanism but also in the resulting radial mass-loss profile, that is, how efficiently material is removed as a function of distance from the star. In the EUV photoevaporation model, the mass-loss profile peaks at around 1 au, the gravitational radius (e.g., Alexander & Pascucci 2012). Photoevaporation operates throughout the disk's lifetime, but it becomes dominant once the accretion rate of material from the disk onto the star slows down and approaches the mass-loss rate due to the wind. At this stage, material flowing inward from the outer disk is photoevaporated once it reaches the gravitational radius (a 5–10 au region),

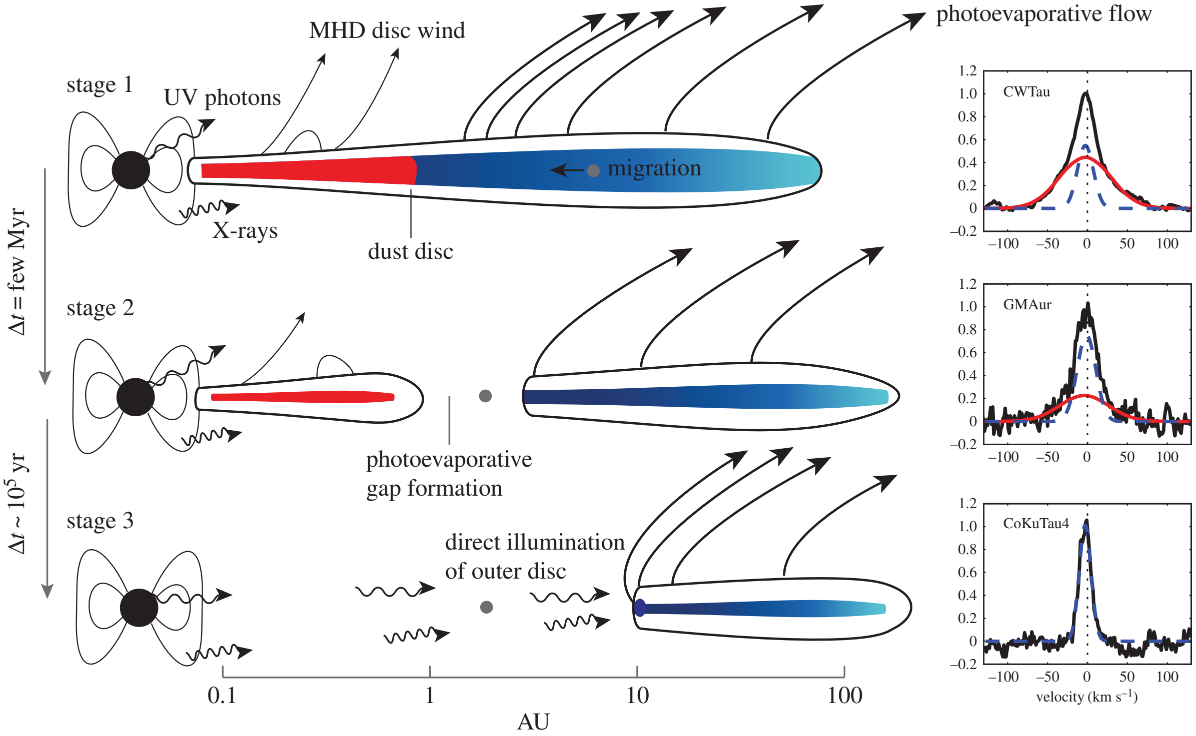

Figure 1.10: Disk evolution stages under the influence of internal photoevaporative winds and MHD winds: a Class II YSO, an accreting transitional disk with a gap, and a non-accreting transitional disk (Ercolano & Pascucci 2017). The right panels show examples of low-velocity [O I] 6300 Å emission, which could be linked to these stages (Simon et al. 2016).

cutting off the resupply of material from the outer disk. The wind then opens a gap in the disk, and the inner disk is dispersed in a $\sim 10^5$ yr-time scale (following a disk lifetime of a few Myr). Observationally, this two-timescale behavior was first inferred from disk surveys: the transition from a disk-bearing to a diskless system was found to be faster than the typical disk lifetimes. A theoretical model by Clarke et al. (2001) coupled the EUV mass-loss profile to viscous evolution models, reproducing the observed behavior.
In the case of X-ray heating, the mass-loss profile is broader for the EUV model, and peaks at ~3 au (Owen et al. 2012). FUV photoevaporation peaks at the outer edge of the disk, where it removes less bound gas (Gorti & Hollenbach 2009).

The heating mechanism is tied to which of the following ingredients is included in the models: hydrodynamics, thermal calculations, and chemistry calculations. Performing thermochemical calculations simultaneously with hydrodynamics is computationally expensive, leading different models to compromise on different factors. The EUV models assume isothermal gas temperature and focus on hydrodynamics. The FUV models focus on chemistry, which the X-ray models do not include. Regarding the outcome, models of X-ray and FUV mechanisms predict much higher photoevaporation rates ($10^{-8} - 10^{-7}$ $M_{\odot}yr^{-1}$, Owen et al. 2010, 2011, 2012) than in the case of the EUV regime ($10^{-10} - 10^{-9}$ $M_{\odot}yr^{-1}$, Hollenbach et al. 1994). Recent advancements will be discussed below, related to the observational signatures.

Winds can also be launched via large-scale magnetic fields. MHD winds are suggested to alter disk angular momentum as they exert torque, as opposed to pressure-driven photoevaporative winds which only remove mass (Blandford & Payne 1982; Bai & Stone 2013, more recently). Provided that gas near the disk surface becomes coupled to inclined magnetic field lines, the gas can be accelerated outward along them, launching a jet perpendicular to the disk. The loss of angular momentum in the disk allows the remaining gas to radially accrete onto the star (Lesur et al. 2023). While photoevaporative winds become most effective at late stages, MHD winds can influence the disk at all stages of its lifetime by regulating accretion rates and mass-loss simultaneously. For this reason, MHD winds have become a major focus of recent theoretical, numerical, and observational studies of protoplanetary disk evolution. The scope of this thesis is limited to disentangling internal and external winds, and the more complex case of MHD-driven winds is not elaborated here. To conclude, the different internal photoevaporation mechanisms and the subsequent stages of disk evolution are shown in Fig. 1.10.

Observational signatures

Internal winds can be observationally identified through velocity shifts in the emission lines such as [Ne ɪɪ] 12.81 μm, [S ɪɪ] 4068 Å, [O ɪ] 5577 Å and [O ɪ] 6300 Å (e.g., Pascucci & Sterzik 2009; Natta et al. 2014; Simon et al. 2016; Fang et al. 2018; Banzatti et al. 2019; Gangi et al. 2023). In addition to blueshifted [Ne ɪɪ] 12.81 μm line, recent JWST observations report the first detection of [Ar ɪɪɪ] in a disk (Bajaj et al. 2024). The origin of the ionization of these species and the role of MHD winds as opposed to photoevaporation is a long-debated question. Ercolano & Owen (2010) and Owen et al. (2010) created synthetic input spectra and obtained fluxes and profiles of emission lines from detailed photoionization calculations. Their results implied that the [O ɪ] 6300 Å and [Ne ɪɪ] 12.8 μm lines are predominantly emitted in the X-ray-driven wind, which however was debated (Alexander et al. 2014).

The models above perform hydrodynamical calculations but are not coupled with chemistry beyond the atomic state. More recent efforts aim to unite them. Picogna et al. (2019) reported that the [O ɪ] 6300 Å observations are consistent with EUV+X-ray photoevaporation models. Sellek et al. (2024) built a comprehensive photoevaporation model (PLUTO+PRIZMO), focusing on X-ray–driven winds, by combining hydrodynamics with simultaneously calculated thermochemistry. They demonstrated that the comprehensive model reduces the resulting X-ray driven mass-loss rates. Based on line flux ratios, Bajaj et al. (2024) report that neon is most likely ionized by X-rays, and argon ionized by EUV. Indeed, the thermal wind models agree that the [Ne ɪɪ] emission is likely to trace an X-ray-driven wind (Sellek et al. 2024). The origin of the Ar emission is more nuanced, as they reproduce the wind's column density if the wind is optically thin to hard X-rays in the outer parts of the wind, and optically thick to soft X-rays and EUV in the inner parts of the wind.

Given sufficiently high spectral resolution, the spectral profiles can be separated into multiple components (Fig. 1.11). High-velocity components (HVC) trace fast-moving winds with blueshifts up to 150 km s^{-1}, associated with jets (Hartigan et al. 1995). Slow disk winds (~10 km s^{-1}) are associated with the low-velocity component (LVC) of optical forbidden lines.

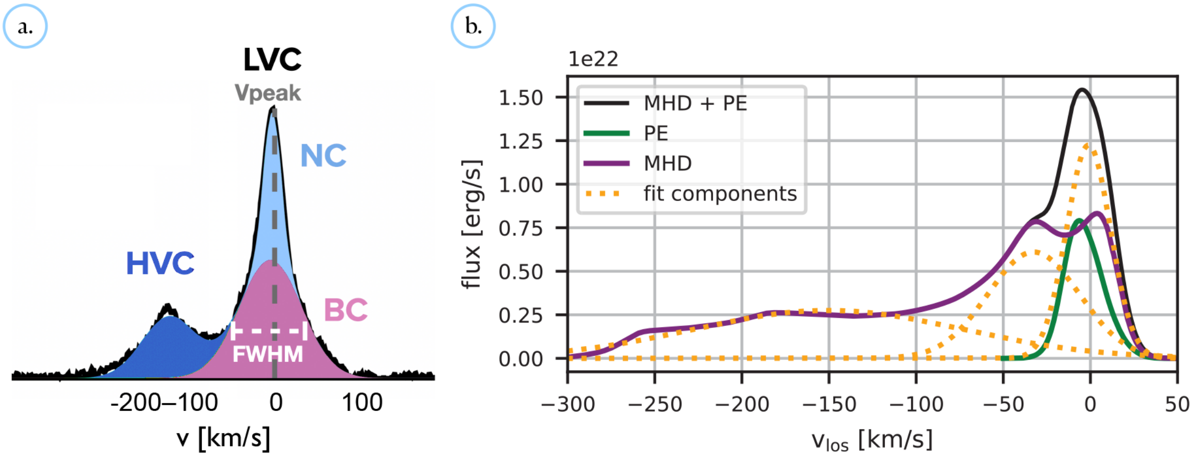

Figure 1.11: [O I] 6300 Å line profiles from: (a) observations, showing multiple Gaussian components (Banzatti et al. 2019); (b) models, showing simulated spectral profiles which include MHD and photoevaporative winds; v_{los} marks line-of-sight velocity of the gas (Weber et al. 2020).

The LVC can further be decomposed into two Gaussian profiles: a broad component (LVC-BC) and a narrow component (LVC-NC) (Rigliaco et al. 2013). The broad component is blueshifted and linked to an MHD wind in the innermost ($\lesssim$0.5 au) region of the disk (e.g., Simon et al. 2016; Whelan et al. 2021; Banzatti et al. 2019). The origin of the narrow low-velocity component is more elaborate. Rigliaco et al. (2013) suggested that the LVC narrow component originates from photoevaporation, whereas the LVC broad component does not. Banzatti et al. (2019) argued that both the broad and narrow components may originate from the same process, an MHD wind. However, Weber et al. (2020) suggested that, the narrow component may be related to photoevaporative winds, and the broad component produced by an MHD wind. An additional consideration in the study of the [O I] 6300 Å line profile is that it evolves with age and the SED (Banzatti et al. 2019). Indeed, a single component line profile of [O I] 6300 Å has been observed in older regions (Nisini et al. 2024).

1.3.3 External photoevaporation

The basic theoretical picture of external photoevaporation is similar to the case of the internal counterpart, however with the depletion of the disk taking place outside-in (Fig. 1.12). If a fully bound disk is externally irradiated by the star(s) lying outside the system, the temperature and hence sound speed of the gas particles in the outer disk increases. Given the Eq. 1.8 above, the gravitational radius r_g decreases until it is interior to the disk edge, setting material beyond r_g unbound. FUV photons photodissociate molecules and drive the mass loss from the disk, and EUV photons ionize the outflowing gas—they exceed the necessary energy threshold.

The resulting mass loss can be estimated in several different ways. One of the ways involves the readily observable ionization front. Its size, R_{IF} can be defined by the photoionization equilibrium (Johnstone et al. 1998). The external flux incident upon the proplyd (with ionizing

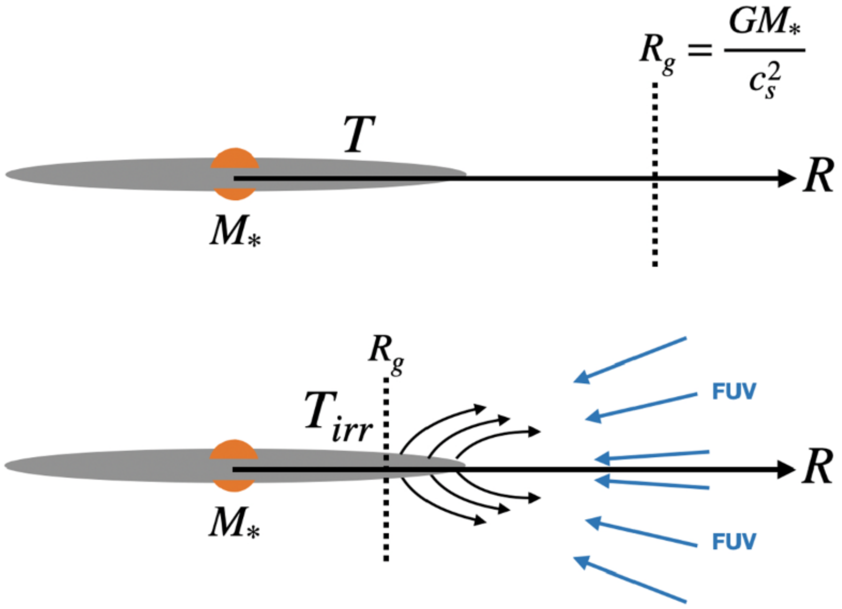

Figure 1.12: Upper figure: Material of the disk fully bound within the gravitational radius (R_g). Lower figure: Gravitational radius shifted inwards to the disk, outer material becoming unbound (Winter & Haworth 2022).

photons assumed not to be absorbed by dust) is

$$F = \frac{\dot{N}_{\mathrm{EUV}}}{4\pi D^2} \tag{1.9}$$

where $\dot{N}_{\mathrm{EUV}}$ is the rate of EUV photons emitted from the external star, and D is the distance from the ionizing source. The flux is balanced by the recombinations in the ionized outflow of density n_{II}:

$$\frac{\dot{N}_{\mathrm{EUV}}}{4\pi D^2} = \alpha \int_{R_{IF}}^{\infty} n_{II}^2(R) dR, \tag{1.10}$$

with $\alpha = 2.58 \times 10^{-13}\ \mathrm{cm}^3\ \mathrm{s}^{-1}$ as the recombination coefficient.

Assuming a spherically symmetric, steady flow with constant radial velocity:

$$n_{II} = n_{\mathrm{IF}} \left(\frac{R_{\mathrm{IF}}}{R}\right)^2 \tag{1.11}$$

$$\frac{\dot{N}_{\mathrm{EUV}}}{4\pi D^2} = \alpha R_{IF}^4 \int_{R_{IF}}^{\infty} n_{IF} R^{-4} dR, \tag{1.12}$$

$$\frac{\dot{N}_{\mathrm{EUV}}}{4\pi D^2} = \frac{\alpha}{3} n_{\mathrm{IF}}^2 R_{\mathrm{IF}} \tag{1.13}$$

The density at the ionization front can be expressed as

$$n_{\mathrm{IF}} = n_0 \left(\frac{R_0}{R_{\mathrm{IF}}}\right)^2 \tag{1.14}$$

where n_0 is the density at the base. We can then rewrite R_{IF} as:

$$R_{IF} = \left[\alpha \frac{4\pi D^2}{3} \frac{R_0^4 n_0^2}{\dot{N}_{\mathrm{EUV}}}\right]^{1/3} \tag{1.15}$$

The mass-loss rate from the disk is given by:

$$\dot{M} = 4\pi R_0^2 \mu m_H n_0 v \tag{1.16}$$

Combining the above, the mass-loss rate is related to the R_{IF}, the ionizing flux, and the projected separation:

$$\dot{M} \propto R_{IF}^{3/2}\, \dot{N}_{\mathrm{EUV}}^{1/2}\, D^{-1} \tag{1.17}$$

When including the numerical value of α and switching into au instead of cm, the size can further be presented as:

$$\frac{\dot{M}}{10^{-8}\mathrm{M}_\odot \mathrm{yr}^{-1}} = 1200^{-3/2} \left(\frac{R_{\mathrm{IF}}}{au}\right)^{2/3} \left(\frac{\dot{N}_{\mathrm{EUV}}}{10^{45}\mathrm{s}^{-1}}\right)^{1/2} \left(\frac{D}{\mathrm{pc}}\right)^{-1} \text{ au.} \tag{1.18}$$

Equation 1.18 was applied to estimate mass-loss rates in NGC 2024 (Haworth et al. 2021), NGC 1977 (Haworth et al. 2022), and the ONC (Aru et al. 2024b, MUSE), (Ballering et al. 2023, ALMA). This relation provides an upper limit on the mass-loss rate due to the projected separation and the exclusion of extinction. Yet the ionization front is readily observe, and this method provides a quick estimate. The derived mass-loss rates have been in reasonable agreement with others (Ballering et al. 2023, e.g.,).

Sophisticated models comprising photoionization, hydrodynamics and radiative transfer calculations have also been presented for this task (Henney et al. 2002). The values remain high across the methods, on the order of $10^{-7} - 10^{-6} M_\odot \mathrm{yr}^{-1}$.

The outflow of material from the disk is first neutral and becomes increasingly ionized. The stellar wind of the massive star continues to act on the expanding gas, shaping the cloud into a comet-like tail. This morphology of is illustrated in Fig. 1.13. However, the observed shape is not always as straightforward, and a diverse selection of proplyds have been noted (Fig. 1.14.

Observational signatures

The observational signatures of external photoevaporation can be categorized into the following.

- **Ionized gas tracers.** The emission lines tracing the ionization front of proplyds are straightforward observational signatures of ongoing external photoevaporation. These include Hα and forbidden lines of neutral and ionized species of oxygen, nitrogen, and sulfur,

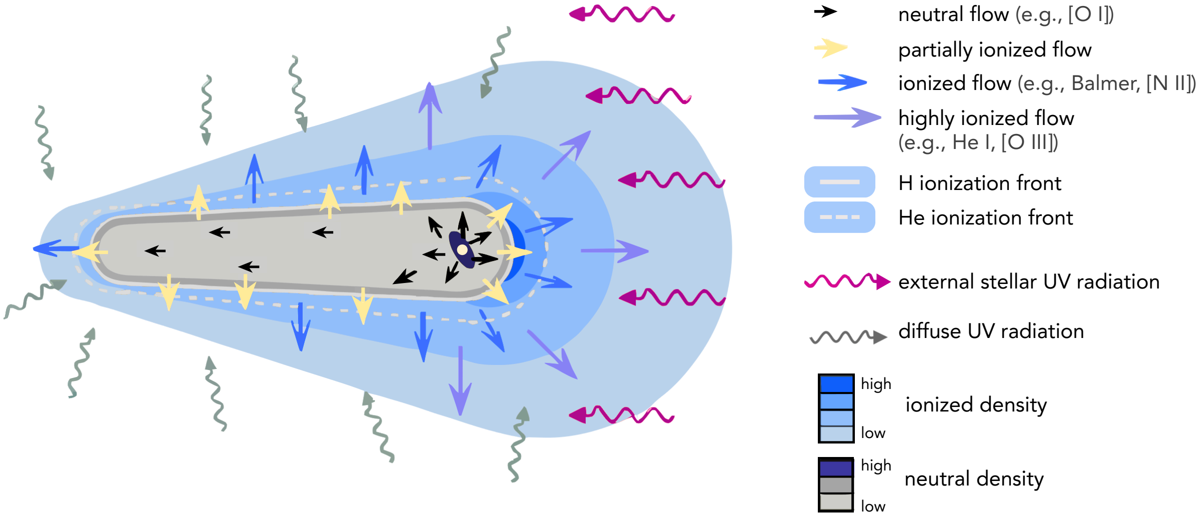

Figure 1.13: Components of the photoevaporating flow in a proplyd. Adapted from Henney & O'Dell (1999).

Figure 1.14: A collage of ONC proplyds acquired with Hubble's Advanced Camera for Surveys (ACS). Credit: NASA/ESA and L. Ricci (ESO)

which are discussed in detail in the following chapter of this thesis.

- **Radio free–free continuum**. Emitted from proplyd ionization fronts. Explored in the early studies, such as Churchwell et al. (1987) to more recently Boyden & Eisner (2020); Ballering et al. (2023). Radio emission studies are described further in Sect. 1.4.4.

- **[O I] 6300 Å.** This emission line traces both the warm neutral gas (~1000 K) inside the dense PDR at the disk surface (Champion et al. 2017), and the ionization front.
Ballabio et al. (2023) simulated theoretical line profiles of the OH dissociation-driven emission of [O I] 6300 Å to predict how the line strength scales with FUV irradiation. The work greatly expanded on the model presented by Störzer & Hollenbach (1998), including a wide range of UV field strengths, updated chemical reaction coefficients, and PDR microphysics. The authors found that the [O I] 6300 Å line luminosity increases dramatically above ~5000 G_0 *, and the line luminosity was compared to observations of ONC proplyds for consistency. Ballabio et al. also found that the ratio of the emission line to accretion luminosity undergoes an increase above around 10^4 G_0. indicating that these tracers are promising for external photoevaporation. However, in spatially unresolved observations, the tracer is not reliable if the [O I] emission is mainly contributed from the internal wind.

- **Far-infrared lines: C II 158 μm and [O I] 63 μm** These are dense PDR lines, which were observed in two proplyds in the ONC with the *Herschel* Space Observatory by Champion et al. (2017). They used a 1D model to determine the conditions in the PDR that is created at the disk surface, and they demonstrated an independent estimate of mass loss rate, consistent with prior values.

- **H41α**. Hydrogen radio recombination lines H41α were found to be spatially coinciding with the proplyd ionization fronts (Boyden et al. 2025). By deriving H41α line fluxes, they estimated electron temperatures and electron densities in the ionization fronts.

* It is typical to express the FUV field strength in terms of the Habing field G_0. $G_0 = 1$ corresponds to $1.6 \times 10^{-3}\,\mathrm{erg\,cm^{-2}\,s^{-1}}$ (Habing 1968).

1.4 Observational methods

A variety of techniques are used in observational astronomy, each with their advantages in tackling the study of star and planet formation. Two-dimensional images show the morphology and spatial distribution of extended objects. Traditional long-slit spectroscopy, on the other hand, provides high spectral resolution and higher-sensitivity observations for faint point sources. Detailed maps of an object require multiple slit positions, however, which makes this technique inefficient for extended sources. Integral field spectroscopy (IFS) combines the techniques above by simultaneously collecting spectral and spatial information in the form of 3D data cubes. IFS gives the means to efficiently acquire observations and analyze target(s) in detailed maps. Interferometric facilities complement these methods by achieving angular resolutions and sensitivities unattainable with single telescopes, particularly at millimeter wavelengths. Below, a brief overview of the methods is given, along with their applications in the exploration of proplyds.

1.4.1 Imaging

Imaging provides the most direct means of observation, recording light from targets on a detector to create two-dimensional intensity maps. Imaging typically uses charge-coupled devices (CCDs) or complementary metal–oxide–semiconductor (CMOS) detectors, which convert photons into electronic signals. The pixel size of the detector is a crucial part in the achievable image resolution, along with the telescope optics. Before the light reaches the detector, however, it is passed through filters that select specific wavelength ranges. Narrow-band filters isolate emission from specific atomic or molecular transitions (e.g., an Hα filter isolates light emitted by hydrogen gas). Broadband filters cover a range of wavelengths, providing for example, continuum SED of a disk. Multi-band imaging allows creating color-composite maps of a target. For instance, the Hubble WFPC2 camera (Wide Field and Planetary Camera 2), which was installed in 1993, involved a mix of 48 filters for purposes ranging from galactic observations to protoplanetary disks.

1.4.2 Slit spectroscopy

In slit spectroscopy, light from an object passes through an elongated, narrow slit a the entrance aperture of a spectrograph, blocking most of the field and allowing only a strip to pass through. Light entering the slit is then dispersed by a device such as a diffraction grating, and recorded with a detector. By isolating the light from a target, a high-resolution spectrum can be extracted. In the resulting data, one axis corresponds to the wavelength and the other represents a spatial position along the slit.

In the study of proplyds, early applications of slit spectroscopy include observations made with the Manchester Echelle Spectrometer on the 2.5 m Isaac Newton Telescope (a study of [O III] 5007 Å line profiles of five proplyds, Massey & Meaburn 1995; Henney et al. 1997), and the HIRES spectrograph installed on the Keck telescope (Henney & O'Dell 1999) (Figures 1.15, 1.16). Both works were acquired at a velocity resolution of 6 km s^{-1}. As explained by the authors, the main challenge in extracting the spectra lies in the accurate subtraction of the nebular background which varies significantly on scales of several arcseconds. By fitting models to the spectral line widths and HST emission-line imaging, they measured the proplyd sizes, ionized densities, and outflow velocity.

As an example of recent studies, Goicoechea et al. (2024) observed the irradiated disk d203-506 with the JWST Near Infrared Spectrograph (which has five fixed slits) at R$\approx$2700 resolution or ~0.1" (~40 au at the distance to Orion). They reported the first detection of the [C I] 609 μm emission line and derived the (total) gas-phase abundance of carbon.

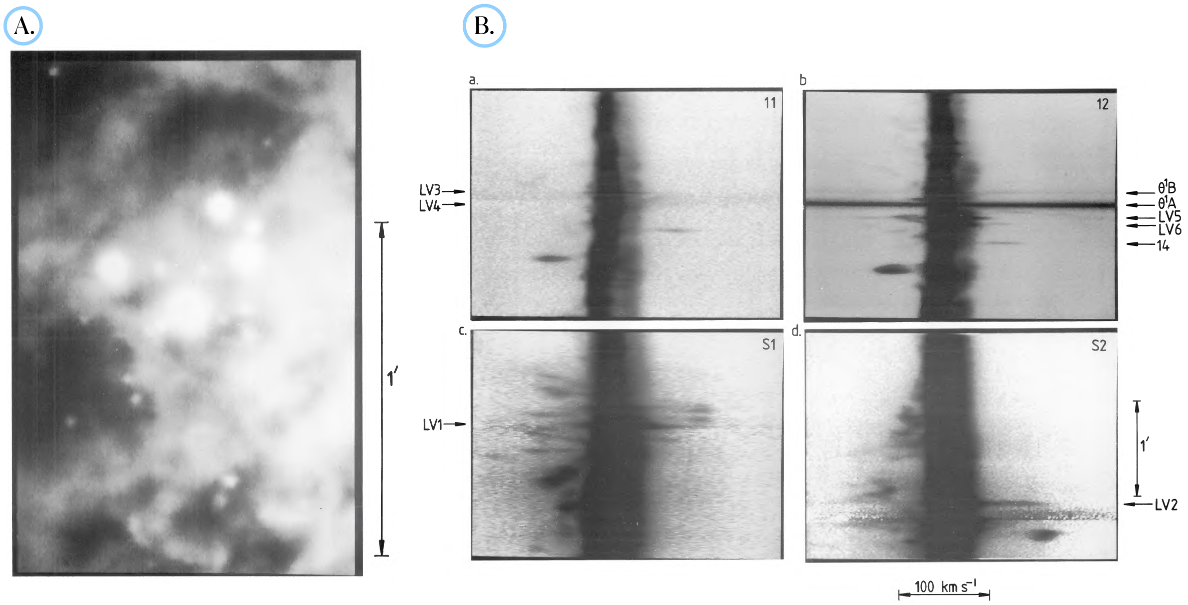

Figure 1.15: (A) An image of the Trapezium region in the [O iii] 5007 Å line, through a 70 Å bandwidth filter. (B) Grey-scale representations of position-velocity arrays obtained from four slit positions with the Manchester Echelle Spectrometer (Massey & Meaburn 1995). Copyright: Royal Astronomical Society

1.4.3 Integral Field Spectroscopy

In an integral field instrument, the integral field unit (IFU) divides the field of view of an acquired image into many segments, that is, an array of single slices. The signal from each slice is fed into a spectrograph, which splits the incoming light into a particular wavelength range, generating a spectrum. All the resulting spectra are arranged into a datacube, which contains the entire 2D field of view plus the third, spectral dimension. There are techniques to divide the field of view, depending on the type of IFU, with the main ones being as follows: a microlens array, a fibre bundle, a mirror array or image slicer, and their combinations.

The earliest integral field spectrograph saw its first light in 1987 following the idea proposed by Courtes 1982. It was installed on the 3.6-metre Canada-France-Hawaii Telescope on Mauna Kea, Hawaii. In 2004, the Gemini Multi-Object Spectrograph (GMOS) became operational at the 8-m Gemini South Observatory (Chile), and its science verification run included observations of the proplyd 167-317, designated earlier as LV 2 (Vasconcelos et al. 2005a). They detected multiple forbidden and permitted emission lines in the spectral range from 5500 to 7600 Å. Tsamis et al. (2011) and Tsamis & Walsh (2011) further examined the proplyd 167-317 or LV 2 and its redshifted jet with the Fibre Large Array Multi Element Spectrograph (FLAMES), at the VLT in the spectral range from 3000 to 7200 Å. More IFS works followed, including the analysis of proplyds 177-341, 170-337 and 170-334 by using the Potsdam Multi-Aperture Spectrophotometer (PMAS) (Mesa-Delgado et al. 2012).

This thesis focuses on the Multi Unit Spectroscopic Explorer MUSE at VLT, which saw first

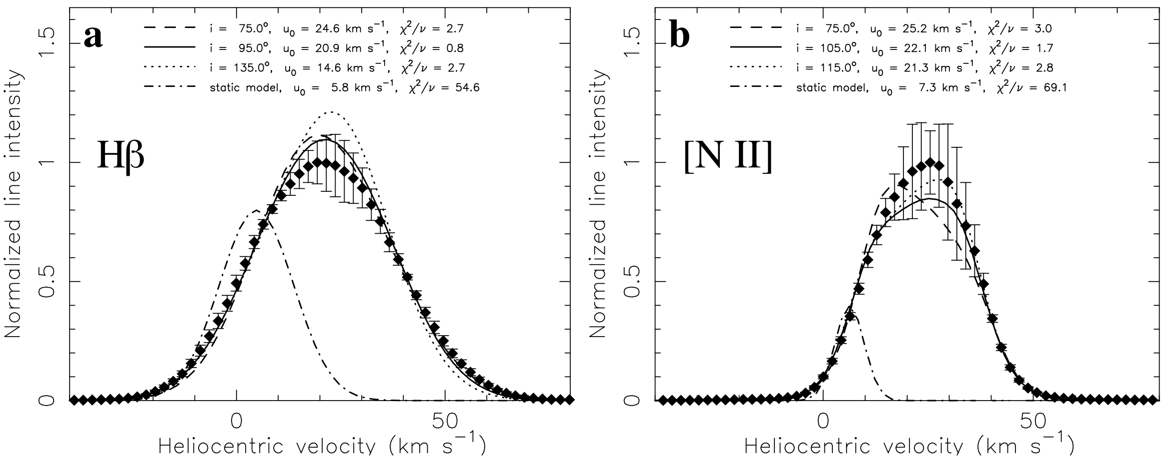

Figure 1.16: Examples of extracted line profiles (solid points) and model fits for the proplyd 177–341W, acquired with the HIRES spectrograph, Keck I telescope (Henney & O'Dell 1999).

Spectral range	0.465–0.93 μm
Resolving power	2000@0.46 μm 4000@0.93 μm
Narrow-Field Mode	
Field of view	7.5×7.5 arcsec^2
Spatial sampling	0.025×0.025 arcsec^2
Spatial resolution @0.75 μm (median seeing)	0.042 arcsec

Table 1.2: MUSE observational parameters

light in 2014. MUSE offers two modes—wide-field and narrow-field—combining high spatial resolution, medium resolving power, and a large simultaneous spectral range in the optical. It comprises 24 identical modules, equipped with an advanced slicer, a spectrograph, and a detector. The incoming field of view is derotated and divided into 24 sub-fields by a series of fore-optics, splitting, and relay optics. The high spatial resolution is achieved through the adaptive optics correction (AO), specifically in the Laser Tomography Adaptive Optics mode, performed by the VLT deformable secondary mirror. AO uses four sodium laser guide stars, and a natural star for tip/tilt correction.

In narrow-field mode, an additional optical system operates in the fore-optics, enabling 0.025" spatial sampling in the 7.5×7.5" field of view (observational parameters are listed in Table 1.2). The main additions lie in AO optimization and configuration: the laser guide stars are moved closer, and tip/tilt sensing is performed at IR wavelengths using either a natural guide star within the field or the target itself. The main steps involved in the production of data-cubes are shown in Fig. 1.17. The scheme is based on the wide-field mode, commonly used for galactic studies, but not discussed here.

The MUSE pipeline (Weilbacher et al. 2020) carries out the classical data reduction steps, in-

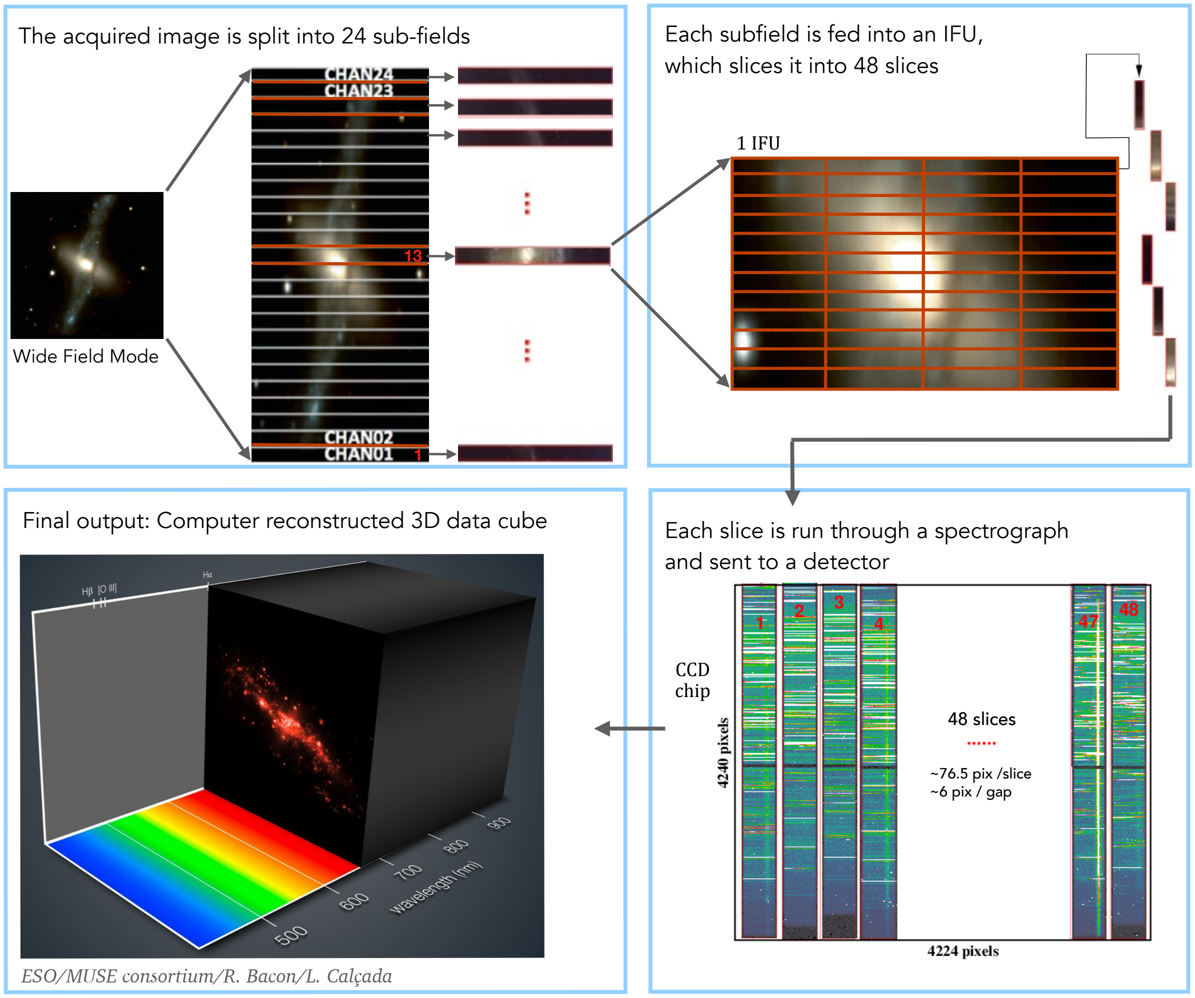

Figure 1.17: The key steps of a MUSE data cube. Adapted from P. Boehm, AIP, 2006, and Weilbacher et al. 2009.

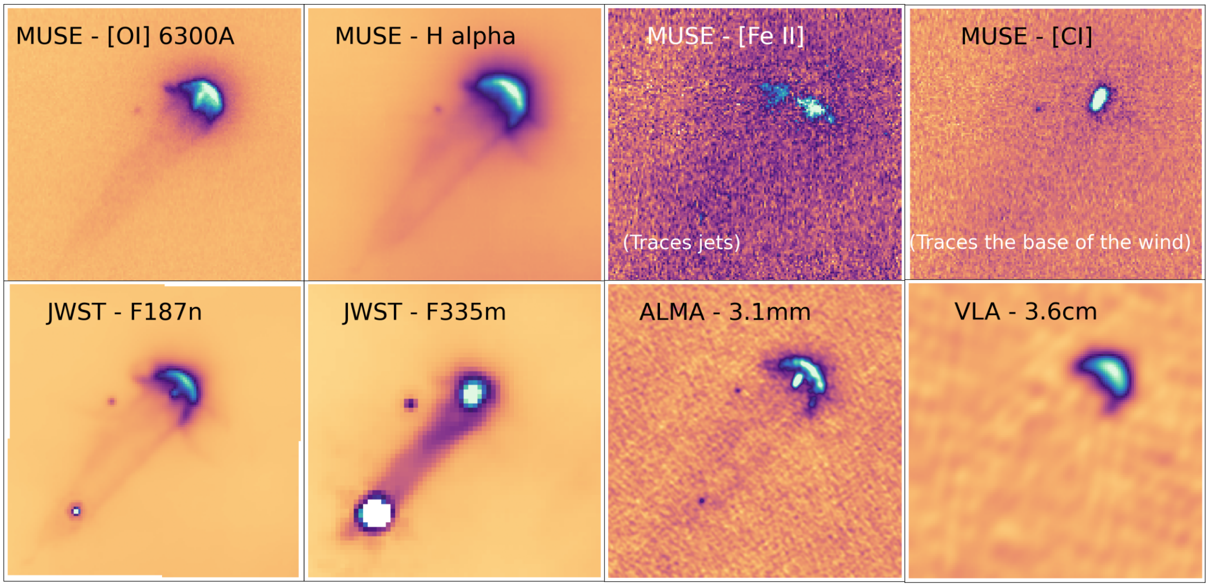

Figure 1.18: Multi-wavelength view of proplyd 177-341W in a 4×4" field of view (Planet formation environments collaboration et al. 2025). The gallery includes images acquired with MUSE (Aru et al. 2024b), JWST NIRCam (McCaughrean & Pearson 2023), ALMA (Ballering et al. 2023), and VLA (Sheehan et al. 2016).

cluding bias, dark, flat computation and correction, wavelength calibration, flux calibration, sky subtraction, and exposure alignment and combination.

1.4.4 Interferometry

In a protoplanetary disk, millimeter-sized dust grains are initially distributed throughout the disk. They experience oscillations around the disk midplane, as they are affected by gas drag and a downward force from the gravity of the star (e.g., Testi et al. 2014). Skipping the complex details of dust dynamics, the dust particles undergo vertical settling and eventually settle on the cold midplane; characterized by a temperature of approximately 20 K. The midplane is where most of the disk's mass is concentrated and where planets are expected to form (Birnstiel 2024, for a review). The traditional method of measuring disk mass has relied on the detection of this cold dust, and applying a gas-to-dust ratio of 1:100. This ratio assumes that the dust accounts for 1% of the total mass (Miotello et al. 2023). The little thermal emission of the dust in the midplane peaks in the wavelength range of 0.1–1 mm, hidden from the optical. Accordingly, instruments operating in the sub-millimeter and millimeter wavelength range have to be employed for observations (Williams & Cieza 2011, for a review on infrared and (sub-)millimeter observations).

In practice, detecting and characterizing the faint emission calls for higher sensitivity and angular resolution than feasible with single-dish telescopes, since the resolving power is limited by their physical dish size. A solution is to use interferometry, in which many smaller antennas are operated together to simulate a single gigantic telescope. In an interferometer, the angular resolution is determined by the maximum distance between antennas, that is, the baseline. The antennas are consequently spread over distances of up to tens of kilometers, and synchronized with exquisite precision.

The first measurements of proplyds at centimeter wavelengths were carried out with the Very Large Array (VLA; Churchwell et al. 1987), an array of 28 antennas in New Mexico. The authors detected the free-free emission from ionization fronts. The rest of the proplyd morphology became visible in more recent radio observations with the with the upgraded VLA (Forbrich et al. 2016; Sheehan et al. 2016). ALMA, the Atacama Large Millimeter/submillimeter Array transformed radio astronomy, introducing a significant improvement in both sensitivity and resolution, with its baselines up to 16 km. ALMA is a facility made up of 66 high-precision antennas located on the Chajnantor plateau, at an altitude of 5000 m in northern Chile. ALMA Band 7 (0.86 mm) observations of Mann et al. (2014) in combination with previous Submillimeter Array data revealed a lack of massive ($\gtrsim$3 M_{Jup}) disks within 0.03 pc of θ^1 Ori C, and the gas disks were found to be compact in comparison with those studied in environments with negligible UV radiation—implying that the UV environment diminishes the mass available for planet formation. These findings were corroborated further with ALMA (Eisner et al. 2016, 2018).

A view including both dust emission from the disk and free–free emission from the ionization front was presented in ALMA Band 3 (3.1 mm) for 12 proplyds by Ballering et al. (2023). Free-free emission occurs in the ionization front as it is occupied by free electrons, which become accelerated by the Coulomb force when passing by an ion.

The authors measured disk radii and spectral indices with a resolution of 0.057", corroborating small disk sizes and finding low spectral indices, which indicates optically thick dust emission. They also derived mass-loss rates in two separate ways. First, through the ionization front radii (based on the ionization equilibrium), and second using the brightness of the free-free emission, finding the range $\dot{M} = 0.6 - 18.4 \times 10^{-7} M_{\odot}\mathrm{yr}^{-1}$ in decent agreement with prior estimates.

A multi-wavelength view of the proplyd 177-341W is given in Fig. 1.18, which illustrates how different techniques are complementary.

1.5 The structure and role of this thesis

The main goal of this thesis is to provide diagnostics of external photoevaporation based on spatially and spectrally resolved observations of proplyds. These diagnostics are necessary for two main reasons: for interpreting the observations wherein the characteristic morphology of proplyds cannot be spatially resolved, i.e., in distant clusters, and for providing a point of reference for models.

Until recently, astronomers have relied on the same observational diagnostics for studying both internally and externally driven photoevaporative winds in protoplanetary disks, as available data from stellar clusters were sparse and limited in spatial and spectral resolution. This overlap made it difficult to assess the relative importance of each process in disk evolution and prevented external photoevaporation from being included in theoretical models.

1.5.1 State of the art and the problem

This section briefly summarizes the wave of observational discoveries and theoretical advancements from circa 2010s.

New proplyd discoveries beyond ONC Bally et al. (2012) discovered a proplyd around a B-type system 42 Ori in the NGC 1977, followed by the discovery of seven more in the same region by Kim et al. (2016). This demonstrated that external photoevaporation and the consequent proplyd morphology manifest also in a much weaker UV environment ($\sim 10^3 G_0$) compared to the ONC. Whereas NGC 1977 is 1–2 Myr old, a finding of a handful of proplyds with HST Haworth et al. (2021) was based in a young environment (~0.5–1 Myr) NGC 2024, the Flame Nebula. These discoveries demonstrate the prevalence of external photoevaporation in a range of the impinging UV field intensities and cluster ages.
The works above imaged the proplyd morphology, providing direct evidence of external photoevaporation. Rigliaco et al. (2009) carried out a spectroscopic study of the σ-Orionis cluster, and detected strong forbidden emission lines of ionized atoms, [S II] and [N II]. In this pioneering work, they argued that the line ratio indicates ongoing external photoevaporation.

Cluster-wide disk evolution under high UV Several studies presented observational evidence of the external photoevaporation effects on disk populations. Based on an ALMA survey in the ONC, Mann et al. (2014) reported a drop in the disk masses at a small projected separation from the central star UV source, within 0.03 pc of θ^1 Ori C(further supported by Eisner et al. 2016, 2018). The result complemented an earlier study of Adams et al. (2004), who explored larger separations, ~0.03–0.3 pc, and derived masses consistent with those found in low-UV SFRs.
The trend of lower disk masses at smaller separations from the UV source was also observed in σ Orionis, based on both an ALMA survey (Ansdell et al. 2017) and a spectroscopic survey with VLT/X-shooter (Maucó et al. 2023). The σ Orionis cluster, hosts an OB stellar association in which the most massive star is an O9 star. Both studies observed a drop of disk masses near the center of the cluster, but at a much larger projected separation than in the ONC—in the inner ~0.5 pc of the cluster. To explain this difference, Maucó et al. (2023) calculated the FUV field strength due to the central OB system, and estimated it to be lower than that of the ONC. At the 0.5 pc mark, the impinging FUV field is $\sim 10^4\,G_0$. Therefore, this region offers a complementary, lower range of UV field strengths to test the effect of external photoevaporation.

Theoretical developments In 2016, important theoretical developments were made in the study of external photoevaporation, prompting analyses in the subsequent years. Facchini et al. (2016) provided new mass-loss rate estimates of photoevaporative winds by expanding parameter space (exploring larger disk sizes and lower FUV fluxes) compared to earlier studies, and by accounting for the grain size distribution of dust. Based on semi-analytic calculations, they found that considering the dust grain growth has a larger impact on the mass-loss rate than previously thought, leading to higher mass loss. Another advancement was made by Haworth et al. (2016) with the development of radiation hydrodynamic simulations, followed by Haworth & Clarke

(2019) presenting the first 2D models of externally photoevaporating disks. These developments provided a more realistic comparisons with observations.
Importantly, based on the radiation hydrodynamic models, Haworth et al. (2018) made a grid of ~4000 calculations publicly accessible, with the grid spanning a range of disk sizes and masses, stellar masses, and FUV field strengths (FRIED, FUV Radiation Induced Evaporation of Discs). With the ready-to-use mass-loss rates, numerous studies drew on the FRIED grid (for a review, see Planet formation environments collaboration et al. 2025, Sect. 2.3.1).

The findings above help us move towards a comprehensive understanding of external photoevaporation in clusters of various ages and UV-field strengths in Orion. While the next crucial step is to expand the studies into more massive clusters, it remains challenging. For example, massive clusters in the constellation Carina, such as Trumpler 14 and Trumpler 16, are distant (> 2 kpc), which hinders the possibility to resolve ONC-like proplyds with current facilities. In addition, these regions exhibit strong, highly variable nebular emission (Itrich et al. 2024). Next-generation observatories, such as the ESO 39-m Extremely Large Telescope, are expected to overcome these limitations. In any case, reliable signatures of external photoevaporation are needed in order to confirm whether the effect is underway in spatially unresolved targets.

1.5.2 The role and structure of this thesis

This thesis aims to disentangle internal and external photoevaporation by identifying signatures unique to externally driven winds and therefore determine whether this process takes place. This aim can be achieved with the novel observations delivered by IFS. A further goal is to assess the use of optical IFU data for measuring the physical properties of external photoevaporation. These observations are promising for the robust characterization of external photoevaporation, which in turn provides constraints needed for refining models of disk dispersal. Establishing these diagnostics in Orion sets the foundation for future studies in more massive and distant clusters, where disk morphologies cannot be spatially resolved, and where external photoevaporation is expected to play a dominant role. This thesis includes the following chapters. **In Chapter 2,** I present the sample of proplyds, detailing their observations, the detected morphology, and the analysis of their ionization front radii. These radii are then used to derive the mass-loss rates of the targets, and their values are compared to those in the literature. The Chapter presents the wealth of emission lines in different degrees of ionization. The observed spatial distribution of ionization states of oxygen in proplyds is compared with a simple model.
Chapter 3 focuses on studying a forbidden line of neutral atomic carbon, [C I] 8727 Å and its potential to act as a tell-tale tracer to disentangle the externally and internally photoevaporative winds. While I use an analysis method described in Chapter 2, I also employ ALMA data for the spatial comparison between thermal dust emission from the disk, and the gas emission (MUSE). The Chapter highlights the potential of using the [C I] line as a proxy to trace external photoevaporation, and future studies to solidify the result.
In Chapter 4, I describe additional data analysis methods, including extinction correction and background subtraction. The latter is required for extracting the proplyd emission from the variable nebular emission. These steps allow better measurement and analysis of line ratios. As a result, the most robust combination of line ratios are identified for detecting external winds. I

also present possibilities for constraining the physical properties with MUSE based on line ratios. Finally, **Chapter 5** gives an outlook onto the work and concludes the thesis.

2

MUSE observations of proplyds in the Orion Nebula Cluster: I. Sample presentation and ionization front sizes

This chapter is published as Aru et al., 2024, A&A, 687, A93.

Full author list: **M. L. Aru**, K. Maucó, C. F. Manara, T. J. Haworth, S. Facchini, A. F. McLeod, A. Miotello, M. G. Petr-Gotzens, M. Robberto, G. P. Rosotti, S. Vicente, A. Winter and M. Ansdell.

Abstract

In the Orion Nebula Cluster (ONC), protoplanetary disks exhibit ionized gas clouds in the form of a striking teardrop shape as massive stars irradiate the disk material. We present the first spatially and spectrally resolved observations of 12 such objects, known as proplyds, using integral field spectroscopy observations performed with the Multi-Unit Spectroscopic Explorer (MUSE) instrument in Narrow Field Mode (NFM) on the Very Large Telescope (VLT). We present the morphology of the proplyds in seven emission lines and measure the radius of the ionization front (I-front) of the targets in four tracers, covering transitions of different ionization states for the same element. We also derive stellar masses for the targets.

The measurements follow a consistent trend of increasing I-front radius for a decreasing strength of the far-UV radiation as expected from photoevaporation models. By analyzing the ratios of the I-front radii as measured in the emission lines of Hα, [O I] 6300Å, [O II] 7330Å, and [O III] 5007Å, we observe the ionization stratification, that is, the most ionized part of the flow being the furthest from the disk (and closest to the UV source). The ratios of ionization front radii scale in the same way for all proplyds in our sample regardless of the incident radiation. We show that the stratification can help constrain the densities near the I-front by using a 1D photoionization model.

We derive the upper limits of photoevaporative mass-loss rates ($\dot{M}_{\rm loss}$) by assuming ionization equilibrium, and estimate values in the range 1.07–94.5 × 10^{-7} $M_\odot$ yr^{-1}, with $\dot{M}_{\rm loss}$ values decreasing towards lower impinging radiation. We do not find a correlation between the mass-loss rate and stellar mass. The highest mass-loss rate is for the giant proplyd 244-440. These values of $\dot{M}_{\mathrm{loss}}$, combined with recent estimates of the disk mass with ALMA, confirm previous estimates of the short lifetime of these proplyds.

This work demonstrates the potential of this MUSE dataset and offers a new set of observables to be used to test current and future models of external photoevaporation.

2.1 Introduction

Protoplanetary disks, composed of gas and dust, emerge as a consequence of the star formation process, and provide the birthplaces of planetary systems. The evolutionary pathways of protoplanetary disks and their ability to form planets are expected to differ depending on the surrounding environment, with disks undergoing rapid changes in the presence of massive stars (for a recent review see Parker 2020 and Reiter & Parker 2022). In massive clusters near OB-type stars, UV radiation can externally photoevaporate disks and severely diminish their size, mass, and survival timescale (e.g., Winter & Haworth 2022).

The effect of external photoevaporation can be studied in the act in the Orion Nebula Cluster (ONC), where the primary UV source is the O6V star θ^1 Ori C (O'Dell et al. 2017). These systems of ionized protoplanetary disks, known as "proplyds", were first imaged with the Hubble Space Telescope (HST), exhibiting ionization fronts, disk silhouettes, and comet-like tails pointing away from the UV source (O'Dell et al. 1993; O'Dell & Wen 1994; McCaughrean & O'Dell 1996; Ricci et al. 2008).

Proplyds are detected in strong Hα emission, which serves as a signature of ionized gas near the ionization front, where UV radiation effectively ionizes the wind from the disk. The Hα surface brightness was first employed by Laques & Vidal (1979) to estimate the electron density of the gas in proplyds, which at the time were proposed to be partially ionized globules. Subsequently, Henney et al. (1997) introduced the first theoretical models, which reproduced the emission line profiles. Expanding on the latter study, Henney & O'Dell (1999) compared the models with high-resolution spectroscopy measurements of four proplyds acquired with the HIRES spectrograph on the Keck Telescope, and analyzed the spatial profiles of Hα, Hβ, and forbidden lines, such as those of oxygen, sulfur, and nitrogen ions. Forbidden lines have been the key tool to probe the density, temperature, and ionization state of the gas in proplyds (Mesa-Delgado et al. 2012). Furthermore, forbidden lines of for instance, [Fe II] and [S II] have traced the supersonic jets and winds from proplyds (Bally & Reipurth 2001; Kirwan et al. 2023).

The characteristic cometary or teardrop shape of proplyds is created by the outflow of neutral gas from the disk as extreme- and far-UV energy photons heat the surface material and drive thermal winds. The neutral gas becomes photoionized as it expands and interacts with stellar UV radiation. The external photoevaporation of disk material leads to mass loss, estimated to be in the range from 10^{-8} to $10^{-6} M_\odot\,\mathrm{yr}^{-1}$ for proplyds within 0.3 pc of θ^1 Ori C, based on values inferred from observations (Henney & Arthur 1998; Henney & O'Dell 1999; Henney et al. 2002) and theory (Johnstone et al. 1998; Storzer & Hollenbach 1999; Richling & Yorke 2000). Recent ALMA Band 3 (3.1 mm) observations of a dozen proplyds in the ONC found values in the order of $10^{-7}\,\mathrm{M}_\odot\,\mathrm{yr}^{-1}$ (Ballering et al. 2023).

Submillimeter wavelength observations with ALMA confirm that the gas disks in the ONC are compact in comparison with the disks studied in environments where negligible UV radiation is present (Mann et al. 2014; Eisner et al. 2018; Boyden & Eisner 2020; van Terwisga & Hacar 2023; Ballering et al. 2023). Similarly, low disk dust masses are found in regions with weaker, but still relevant, UV radiation, such as the inner ~0.5 pc of the σ-Orionis cluster (Ansdell et al. 2017; Maucó et al. 2023). The extreme environment may dramatically alter the initial conditions

Table 2.1: Coordinates and projected separations of the detected proplyds.

Proplyd	RA hh:mm::ss.s	DEC dd:mm:ss.s	d(UV source) [pc]
154-346	05:35:15.44	−05:23:45.55	0.068
167-325	05:35:16.72	−05:23:25.5	0.009
168-326	05:35:16.85	−05:23:26.22	0.012
170-249	05:35:16.96	−05:22:48.51	0.068
170-334	05:35:16.96	−05:23:33.6	0.028
170-337	05:35:16.97	−05:23:37.15	0.031
171-340	05:35:17.06	−05:23:39.77	0.037
173-236	05:35:17.34	−05:22:35.81	0.095
174-414	05:35:17.40	−05:24:14.5	0.106
177-341W	05:35:17.66	−05:23:41.00	0.049
203-504	05:35:20.26	−05:25:04.05	0.077 (θ^2 Ori A)
244-440	05:35:24.38	−05:24:39.74	0.06 (θ^2 Ori A) 0.31 (θ^1 Ori C)

Notes: The information is from O'Dell & Wen (1994); Bally et al. (2000); Ricci et al. (2008); Mann et al. (2014). For the given projected separations d, the UV source is θ^1 Ori C with the exception of 203-504 (irradiated by θ^2 Ori A) and 244-440.

for emerging planets, as the total disk mass limits the mass available for planet formation.

The majority of the past studies of proplyds were carried out with HST imaging in a limited number of filters, and spectroscopic analysis is available for only a few proplyds (e.g., Henney & O'Dell 1999). The Multi-Unit Spectroscopic Explorer (MUSE) is an integral field unit (IFU) spectrograph on the ESO Very Large Telescope (VLT). Used in the narrow-field mode (NFM), MUSE allows for the first time to both spatially and spectrally resolve the structure of proplyds in the ONC, as demonstrated by Kirwan et al. (2023) and Haworth et al. (2023b). The IFU data provides spectroscopy covering a wealth of emission lines at each position in the proplyds, and sub-arcsec spatial resolution of the objects.

Here, we present the morphology of 12 objects in seven emission lines, including Hα, and forbidden oxygen, sulfur, and nitrogen lines. We measure the radius of the ionization front of proplyds, a key ingredient for estimating the mass-loss rate, in Hα and forbidden oxygen lines. Using the forbidden oxygen lines in addition to the traditional tracer Hα is important for gaining a more comprehensive understanding of the physical and chemical processes occurring in these systems. From the spectra, we also measure the stellar properties of the targets.

The paper is structured as follows. In Sect. 2.2, we describe the MUSE observations and data reduction. The sample with the morphology of individual proplyds is presented in Sect. 2.3, and the outline of the analysis steps is given in Sect. 4.2. We summarize the results in Sect. 4.3, and further discuss them in Sect. 3.3.

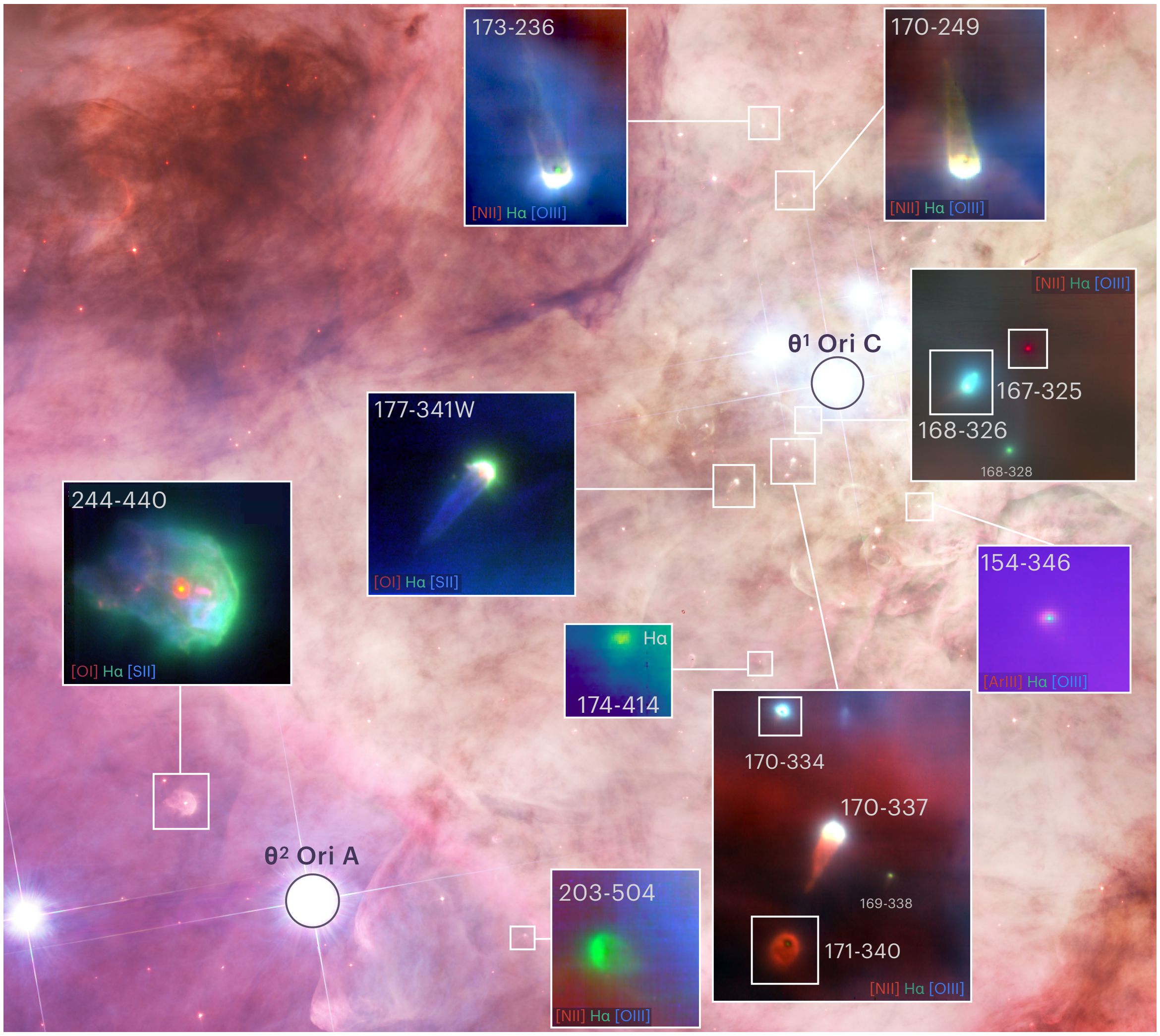

Figure 2.1: RGB images (insets) of continuum subtracted, single line integrated flux images of the sample acquired with MUSE. In each inset, a variety of emission lines are combined to highlight the morphology of the proplyd. The background image is a Hubble optical image of the Orion Nebula Cluster (Credit: NASA, ESA, M. Robberto (Space Telescope Science Institute/ESA) and the Hubble Space Telescope Orion Treasury Project Team).

2.2 Observations and data reduction

The targets in our sample were chosen to cover a large range of distances from θ^1 Ori C, covering different levels of the incident radiation field and thus ionization. Furthermore, the targets were selected to have an overlap with ALMA observations, providing disk mass and size (Mann et al. 2014, Eisner et al. 2018, Boyden & Eisner 2020).

Observations were carried out with the MUSE integral-field spectrograph (Bacon et al. 2010), which is mounted on the Unit Telescope 4 (UT4) at the VLT. MUSE was operated in the Narrow Field Mode (NFM), which covers 4750–9350 Å in a smaller field of view (FOV) of ~7.5" × 7.5". On this FOV, the AO-correction is enhanced by the Laser Tomography Adaptive Optics (LTAO) mode leading to near diffraction limited images with a sampling of 0.025" per spatial pixel. In all the observations, the Natural Guide Star (NGS) was chosen to be the target, and was thus on-axis.

The observations presented here were carried out in three different observing programs between October 2019 and November 2022, always in Service Mode. The observations for the proplyds 244-440 (see Kirwan et al. 2023), 168-328, and 177-341W were taken in October 2019 (program ID 104.C-0963(A), PI: C. F. Manara), and those for the rest of the sample in January and February 2021 (program ID 106.218X.001, PI: C. F. Manara). Finally, we also include here the data taken in November 2022 during the Director Discretionary Time program 110.259E.001 (PI T. J. Haworth) for the proplyd 203-504, which are presented in Haworth et al. (2023b). MUSE was operated under clear sky conditions, and the full AO system was employed, using the stars at the center of our targets as NGS to achieve the best possible correction. The log file, including the airmass-corrected seeing and turbulence parameters are listed in Table 2.4.

The observations were generally composed by three dithered exposures. In each observation, the telescope was offset by 0.2" and 0.1" in the second and third exposures, respectively, and turned by 90 degrees with respect to the previous exposure to achieve the best possible corrections for bad pixels and instrumental effects. The exposure time in each exposure is reported in Table 2.4.

Data reduction was carried out with the MUSE pipeline v2.8 (Weilbacher et al. 2020) run in the ESO Reflex (Freudling et al. 2013) environment. The pipeline carries out the classical data reduction steps, including bias, dark, flat computation and correction, wavelength calibration, flux calibration, sky subtraction, and exposure alignment and combination. The only steps that required non-standard settings were the alignment and combination of the cubes. Obtaining a satisfactory alignment was complicated due to only a small number of stars being present in the observed FOV. For that reason, some of the final cubes are obtained by combining a smaller set of dithering/rotation exposures (see Table 2.4). Having a few stars available in the FOV can also decrease the accuracy of the coordinates, and the coordinates of the central stars are retrieved relative to those catalogued following the process described in Sect. 2.4.1. The final, wavelength calibrated data-cubes are in barycentric velocities, and the wavelength scale is in air wavelengths. The spectral resolution is R≈2000–4000, corresponding to 170–90 km s^{-1} from blue to red. We measure the spatial resolution of the images in the range FWHM≈0.065–0.080" at ~6760 Å in our observations.

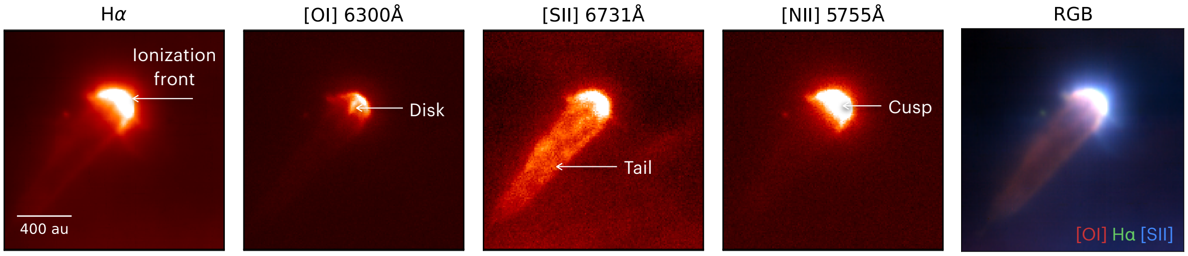

Figure 2.2: Continuum subtracted, single line integrated flux images of proplyd 177-341W. The panels show which parts of the system are visible in given emission lines.

Continuum subtraction was then performed on sub-cubes spanning ~100Å to only include the spectral emission regions of interest. Each sub-cube was continuum-subtracted by fitting a second-order polynomial to the spectrum at each spatial pixel (spaxel) in the sub-cube. This procedure was performed using the Python package MUSE Python Data Analysis Framework (`mpdaf`[1], Piqueras et al. 2017), in particular the function `spec.poly_spec`. After this step, the sub-cubes were divided into smaller slabs with individual lines only, again using `mpdaf`.

2.3 Morphology of observed proplyds

An overview of the ONC with the observed proplyds is presented in Fig. 2.1. The view includes RGB images of nine proplyds: 154-346, 167-325, 170-249, 170-337, 173-236, 174-414, 177-341W, 203-504, and 244-440. In addition, there are proplyds in the background of several images: 168-326, 170-334, and 171-340. The coordinates of the targets are given in Table 3.1. The lines associated with the RGB colors are chosen for each target to show the morphological characteristics described in this section.

A collage of each proplyd is shown in Fig. 2.13 and Fig. 2.14 in the following emission lines: Hα, [O I] 6300Å, [O II] 7330Å, [O III] 5007Å, [S II] 6731Å, [N II] 5755Å, and [N II] 6584Å. These lines are selected to show the various components of the systems, including the ionization front, the disk, the cusp, and the tail, as seen as an example based on proplyd 177-341W in Fig. 2.2. The detailed analysis of these and other emission lines is deferred to forthcoming papers, while here we focus only on the measurement of the ionization front size, well traced by the Hα and oxygen emission lines.

We first describe the morphology of the well-detected proplyds, targets for which the ionization front, the disk, and the tail can be distinguished. These targets appear with the classic teardrop shape and the elongated tail, covering ~1.2-4" in the FOV, except for 244-440 which spans over ~6.4". We then give an overview of the fainter objects, which cover <1" in the FOV, and the non-detections.

---

[1] https://github.com/musevlt/mpdaf

2.3.1 Well-detected proplyds

170-249

The proplyd 170-249 has an elongated tail in the north direction. This tail is visible in Hα, forbidden sulfur species, and [N II] 6584Å lines. The cusp and the ionization front are bright in most of the emission lines, while the disk is traced in the [O I] 6300Å and [S II] 6312Å lines.
In the FOV, the bright central region of a second object is visible in [O I] 6300Å and [N II] 5755Å lines to the southwest of 170-249 (not shown in the RGB image in Fig. 2.1); no tail is distinguished.

170-337

The proplyd 170-337 exhibits the elongated tail in the southeast direction, visible in [S II] 6731Å and [N II] 6584Å emission. The disk can be distinguished in Hα and [O I] 6300Å lines. The cusp and the ionization front are bright in most of the emission lines.
The FOV of 170-337 is rich with more targets:

- In the southeast direction of 170-337, a well-resolved proplyd, designated 171-340, is visible with a round, extended cloud of ionized gas surrounding the disk. The proplyd differs from other objects by bearing a dark core, which may be a disk seen in silhouette against the background nebular light. The structure resembles the case of proplyd HST-10, also designated as 182-413 (O'Dell et al. 1993).
  A long tail is not visible, but the proplyd is extended in the direction opposite the UV source. The proplyd is bright in [S II] 6731Å and [N II] 6584Å lines. The central region appears bright in [S II] 6731Å.

- In the upper part of the cube in the northeast from 170-337, the cusp of the proplyd 170-334 is bright in most emission lines. The classic tail shape is visible in Hα, and it is aligned with the one of 170-337.

- There is a very small proplyd, 169-338, visible to the west of 170-337. We do not include it in the analysis as it is unresolved.

Although 171-340 and 170-334 are smaller than the central target 170-337, it is possible to measure their ionization front radius.

173-236

The proplyd 173-236 exhibits an elongated tail in the northeast direction. The star-disk region is traced by [O I] 6300Å and [S II] 6731Å lines. With a small, bright central part visible in Hα. There is a bubble-like structure southeast from the center of the FOV, which is most prominent in [S II] 6731Å emission (not shown in Fig. 2.1).

177-341W

The RGB image of proplyd 177-341W, shows both a bright cusp and a highly elongated tail in the southeast direction, which is brightest in [S II] and [N II] emission lines. Each emission line traces the cusp with the ionization front. The disk can be distinguished in the [O I] 6300Å emission line, oriented perpendicular to the cusp, in a northwest to southeast direction.

244-440

Proplyd 224-440 is one of the largest in the ONC, spanning about 6.4" from the tip of the longest tail to the ionization front. The tail structure is more complex compared to the other proplyds, resembling a tooth-like shape with two to three tail components depending on the observed wavelength; a JWST/NIRCam view is shown by Habart et al. (2023).
The morphology is striking with different emission lines tracing a variety of the system's components: the cusp and the tail being visible in different ionization states of forbidden oxygen, sulfur, and nitrogen; the disk is bright in [O I] 6300Å. The jet is visible in the MUSE data in the [O I] 6300Å and various [Fe II] lines (Kirwan et al. 2023).

203-504

The proplyd 203-504 is coincident with the Orion Bar, which lies approximately 112" to the southeast of the Trapezium. The teardrop shape is less elongated and more oval compared to the targets close to θ^1 Ori C, and the morphology is bright in Hα and [N II] 5755Å. The cusp is brightest in Hα, [N II] 5755Å, while the disk region is traced in the forbidden oxygen lines. Haworth et al. (2023b) discusses the target in depth. This is the only proplyd in our sample which is directly irradiated only by θ^2 Ori A.

2.3.2 Faint proplyds

154-346

The star-disk region of proplyd 154-346 is visibly bright in each emission listed above, except for [O III] 5007Å and [N II] 5755Å. The proplyd is very small and the classic drop-like shape can be distinguished faintly.

167-325 and its FOV

The proplyd 167-325 is closest to θ^1 Ori C (0.009 pc) in our field. Only the star-disk region of the system is visible, traced in [N II] 6584Å line and faintly in forbidden sulfur species. In the same FOV, there are three objects:

- Two proplyds appear very close to each other in the southeast direction of the central target; the classic shape of the foreground proplyd (168-326) is visible while only a part of the background proplyd can be distinguished. The tail of 168-326 is visible in [NIII] 6584Å

Table 2.2: Measured values for the observed proplyds

Proplyd	R_{IF} Hα ["]	R_{IF}[O I] ["]	R_{IF} [O II] ["]	R_{IF} [O III] ["]	$\dot{M}_{\rm loss}$ Hα $M_\odot\,yr^{-1}$	$M_{\rm disk}$ $[M_{\rm Jup}]$
154-346	0.10*	0.11*	0.10*	...	1.3×10^{-7}	...
167-325	0.10*	0.10*	...	...	8.57×10^{-7}	...
168-326	0.10 ± 0.01	0.10 ± 0.01	0.10 ± 0.01	0.12 ± 0.01	6.43×10^{-7}	5.0 ± 3.0
170-249	0.23 ± 0.02	0.17 ± 0.02	0.21 ± 0.02	0.29 ± 0.03	4.6×10^{-7}	27 ± 0.4
170-334	0.12*	0.09*	0.07*	0.10*	3.9×10^{-7}	...
170-337	0.17 ± 0.02	0.12 ± 0.01	0.14 ± 0.01	0.17 ± 0.02	5.5×10^{-7}	7.13 ± 1.08
171-340	0.19 ± 0.02	0.16 ± 0.02	0.18 ± 0.02	0.18 ± 0.02	5.46×10^{-7}	15.83 ± 0.42
173-236	0.23 ± 0.02	0.20 ± 0.02	0.23 ± 0.02	0.24 ± 0.02	2.85×10^{-7}	45 ± 1.0
174-414	0.13*	0.10*	0.15*	...	1.07×10^{-7}	...
177-341W	0.2 ± 0.02	0.18 ± 0.02	0.21 ± 0.02	0.26 ± 0.03	5.11×10^{-7}	7.48 ± 0.45
203-504	0.21 ± 0.02	0.18 ± 0.02	0.23 ± 0.05	...	2.5×10^{-7}	...
244-440	2.0 ± 0.1	1.95 ± 0.0975	1.97 ± 0.098	2.18 ± 0.22	9.45×10^{-6}	

Notes: * Uncertain value, considered as lower limit. The values of disk dust masses have been estimated by Mann et al. (2014) and Eisner et al. (2018), except for 170-249 and 173-236 (Ballering et al. 2023) (T=20 K).

line. The star-disk region is traced by Hα, [O II] 7320Å , [O III] 5007Å , and [S II] 9068Å lines.

- There is another proplyd in the south of 167-325 and 168-326. It is much smaller, and its ionization front size is not measured.

174-414

The proplyd 174-414 appears at the very edge of the cube which was planned to be an observation of HST-10. The teardrop shape is visible faintly in Hα and [N II] 6584Å. The central part is bright in [O I] 6300Å, [O II] 7320Å and forbidden nitrogen and sulfur lines.

2.3.3 Non-detections

The proplyds 142-301, 167-231, and HST-10 were targeted on our MUSE programs, but not detected.
In the case of proplyd 159-350, the pointing was not accurate and the observation of this proplyd was not acquired; instead, the pointing was centered at the nearby proplyd 154-346.

2.4 Analysis

2.4.1 Measurement of the ionization front radius

Our goal is to study the radius of the ionization front (I-front) as a function of the incident radiation field. Here, we focus on measuring the I-front radius for four lines: Hα, [O I] 6300Å , [O II] 7330Å , and [O III] 5007Å. The Hα line allows us to detect the region where ionized gas transitions to neutral gas; this has been used as the tracer of the ionization front in past studies (e.g., Henney & Arthur 1998; Henney & O'Dell 1999). The forbidden oxygen lines allow us to additionally trace the ionization structure for different ionization states.

We located the I-front at the bright cusp on the side closer to the UV source. The main UV influx comes from θ^1 Ori C for all proplyds except 203-504 and 244-440, which appear to be primarily irradiated by θ^2 Ori A (O'Dell et al. 2017; Haworth et al. 2023b).

As the coordinates of the stars in the MUSE cubes might not directly correspond to those cataloged because of poor astrometric calibrations of our dataset (described in Sect. 2.2), we determined the coordinates of the central stars in the MUSE data directly. We created a sub-cube with continuum emission only, that is, a region free of lines, at 6740-6780Å. We located the peak of the continuum emission by using the `mpdaf` function `peak` in the region of the star. The coordinates of the peak were used as the location of the star for the following steps and the following measurements were always carried out using relative distances (Fig. 2.3).

We then retrieved a radial cut of the proplyd intensity profile in each of the investigated lines by tracing a 6" line centered at the coordinates of the central star. We set the position angle of the radial cut in the direction between the central star and the peak of the emission in the ionization front, which in turn is in the direction of the ionizing star in all cases, with the exception of 244-440 and 203-504. For 203-504, the angle between the proplyd and θ^2 Ori A was calculated based on their catalogued coordinates. The intensity profile along the line was extracted by using cubic interpolation with the `scipy` function `map_coordinates`. The location of the I-front was determined relative to the line's center, the ~0" mark on the x-axis of the intensity profile. For the majority of the sample, an intensity peak corresponding to the I-front, a bright region in the direction of the UV source, lies at a small offset from the center. This offset is the radius of the I-front.

The I-front radius value measured from the intensity profile overlaps roughly with the brightest area visible on the image of each proplyd; the scale parameters of the image can slightly change the boundary of the brightest area. An example of the measurement method is shown in Fig. 2.3.

We estimated the uncertainty by repeating the measurement for two more position angles (±15°), and calculating the percentage change between the values of I-front radii. The typical uncertainty in the cases of good detection is 10% (see Table 2.2).

Proplyds 154-346, 167-325, 170-334, and 174-414 make up a much smaller part in the FOV compared to the well-detected targets. In those cases, no distinct peak is visible in the intensity profile and we estimated the I-front's position based on locating the outer part of the bright center of the target. This is the lower limit of the I-front.

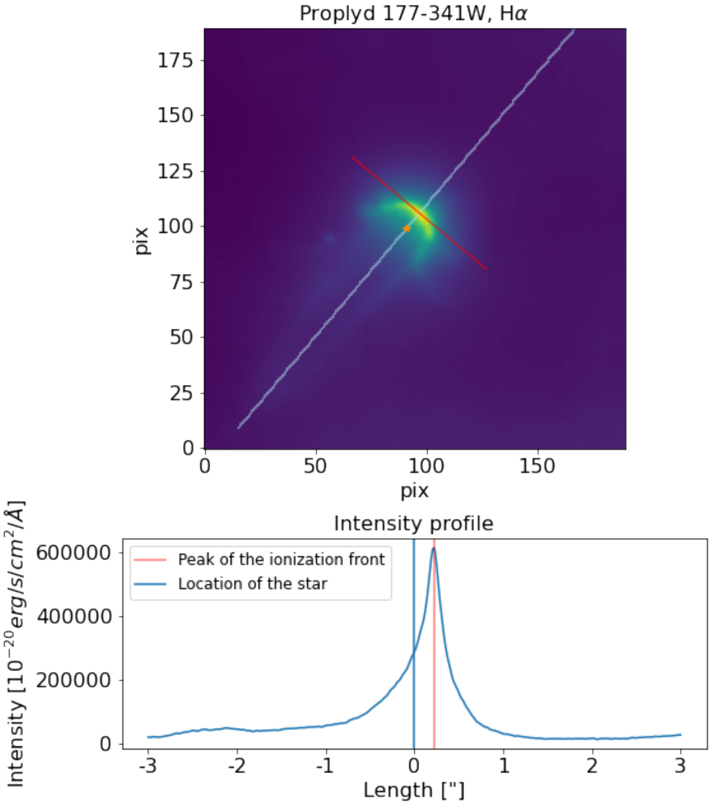

Figure 2.3: Method for measuring the ionization front radius of a proplyd. Top panel: the intensity cut is taken along the diagonal line. The red line marks our identification of the ionization front. Bottom panel: intensity cut along the diagonal line marked in the top panel.

The identification of the I-front was straightforward for the Hα lines of each well-detected proplyd. The I-front was fainter and less clear to distinguish the oxygen lines of several proplyds. There were two intensity peaks for the oxygen lines compared to the single peak in Hα intensity profiles: the higher peak coincided with the star's location, and the smaller peak coincided with the I-front. The principle of the measurement remained the same. The measured I-front radii in the various lines are reported in Table 2.2.

2.4.2 Stellar parameters

The MUSE data allow us to determine the stellar parameters of the central objects for the observed proplyds. We extracted the spectra of the stars using a circular aperture of 0.05"–0.075" depending on the target and an annulus of 0.075"–0.175" to estimate the sky emission. The spectra for 167-325 and for 168-326 could not be extracted as the S/N ratio of the continuum is too low.

The spectra were then compared with the set of pre-main-sequence empirical templates from Manara et al. (2013, 2017a), and Claes et al. (in prep.) to determine the spectral type (SpT)

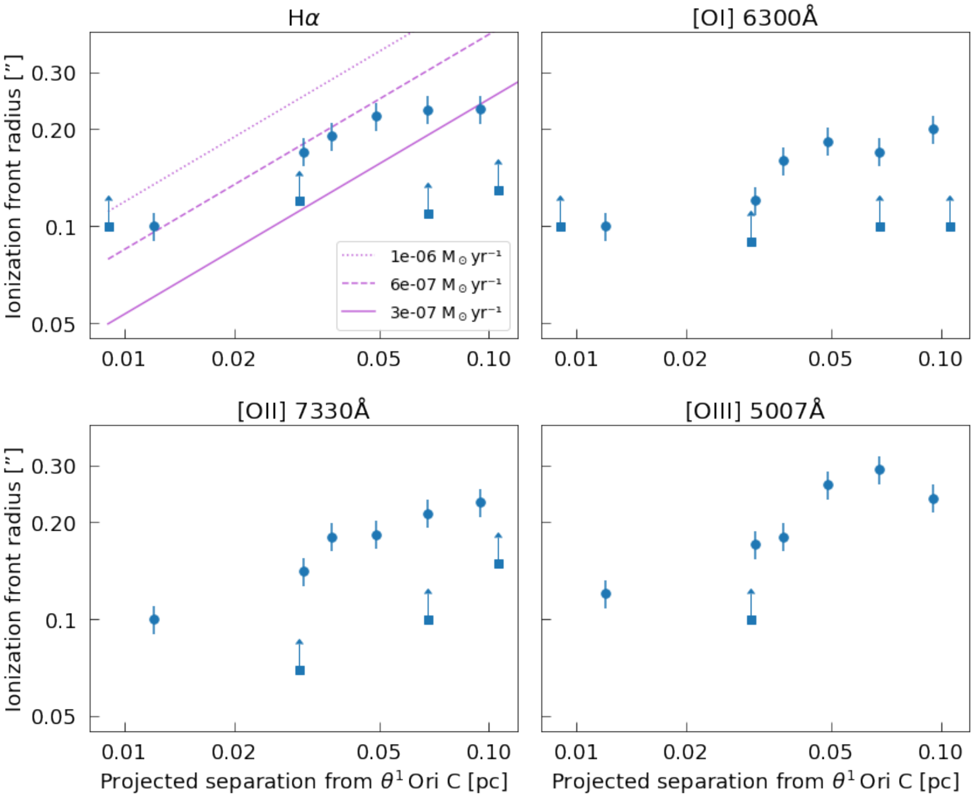

Figure 2.4: Ionization front radius versus the projected separation from θ^1Ori C. Squares mark proplyds for which the I-front measurement has a higher uncertainty. The radii of the ionization fronts increase with larger projected distances from the UV source. Due to noisy subcubes, measurements were not taken for proplyd 167-325 (closest to the UV source) in the bottom panels. For the same reason, the panel of [O III]5007Å excludes the radii of several targets.

and extinction (A_V). The latter was determined assuming the reddening law by Cardelli et al. (1989) and a value R_V=3.1. Typical uncertainties on these derived parameters are of 1-2 subclasses for the SpT and of 0.5 mag on A_V, but they depend on the quality of the spectrum in the redder part (λ >750 nm) which is sometimes suboptimal for several reasons, including strong emission lines and telluric absorption. The SpT was converted into effective temperatures ($T_{\rm eff}$) using the relation by Herczeg & Hillenbrand (2014). From the $J-$band magnitude (Robberto et al. 2010), we then estimated the stellar luminosity ($L_\star$) using the bolometric correction by Herczeg & Hillenbrand (2014), to finally derive a stellar mass ($M_\star$) using the evolutionary tracks by Siess et al. (2000). The latter was used because most of the targets appear to be located on the Hertzsprung-Russel Diagram above the 1 Myr isochrone, not covered by other tracks, as expected due to their young age.

The derived parameters are reported in Table 2.3, and the best fits are shown in Fig. 2.16. We compare the derived values with Fang et al. (2021), but only a sub-sample of our targets are covered by that study, and they show a good agreement within one subclass with our estimates.

Table 2.3: Stellar parameters derived for the sampled proplyds

Proplyd	SpT	A_V [mag]	$T_{\rm eff}$ [K]	$\log(L_\star)$ [$L_\odot$]	$M_\star$ [$M_\odot$]
154-346	M0	4.5	3900	0.46	0.60
167-325	...	...	...	...	...
168-326	...	...	...	...	...
170-249	M4.5	3.5	3085	-0.48	0.20
170-334	K5.5	3.0	4162	1.05	1.02
170-337	K6	3.5	4115	0.39	0.79
171-340	M1	3.0	3720	0.22	0.47
173-236	K5.5	5.0	4160	0.96	0.99
174-414	M5	6.0	2980	-0.34	0.18
177-341W	K5.5	4.3	4160	-0.30	0.91
203-504	K5.5	3.0	4160	-0.74	0.72
244-440	M0	3.0	3900	0.42	0.59

2.5 Results

2.5.1 Ionization front radius

The ionization front radius of proplyds enables us to infer the mass-loss rate of proplyds, which is a critical factor in the evolution of protoplanetary disks. The radii of targets irradiated by θ^1 Ori C are shown as a function of the projected distance from the massive star in Fig. 2.4. We note that given the distance to the ONC and the generally high optical extinctions towards the region, the *Gaia* parallaxes for our targets are not always available, or they are too uncertain to provide reliable individual distances to the targets. For this reason, we assume a common distance of 400 pc for the targets in our sample, and only consider projected separations from the ionizing stars in our analysis. In the panel of Hα emission, we compare the measurements with predicted values for a set of mass-loss rates, as described in Sect. 2.5.3.

Figure 2.4 shows that the I-front radius is generally larger at lower ionization rates, that is, at larger projected distance, in all tracers discussed here. The proplyds with more uncertain measurements do not however typically follow the trend. The proplyds with more uncertain measurements are small and faint compared to the rest of the sample, and the I-front measurement could not be carried out with the same approach.

To explore the significance of the relation between I-front radii (R_{IF}) and projected distance (d_p), we carried out two analyses similarly to McLeod et al. (2021). Firstly, we tested the null-hypothesis that there is no relation between the parameters. We used a bootstrap sampling method with 10^4 iterations, where we randomized the x-axis values and computed the Spearman correlation coefficient (r_s). By calculating the σ distribution of the data, we can exclude the null-hypothesis with a larger than 2σ confidence in all cases ($p<0.05$). Secondly, we assessed the

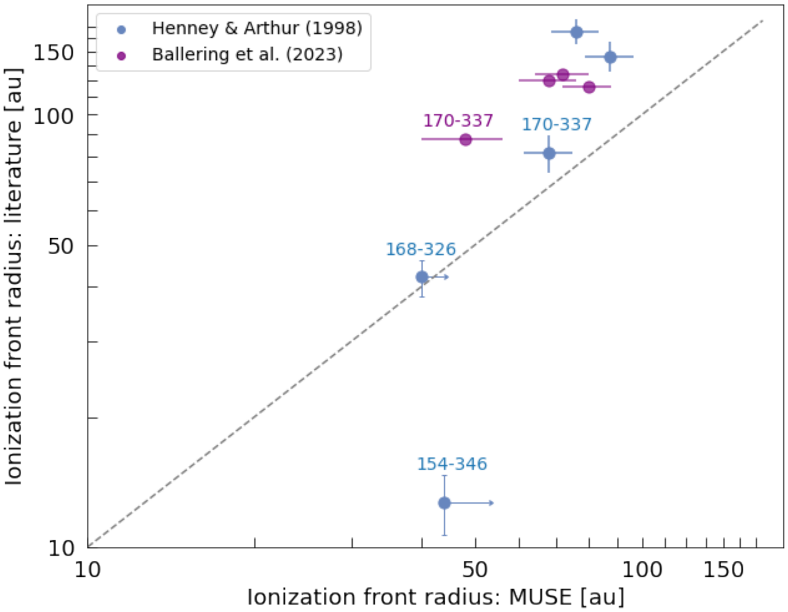

Figure 2.5: Ionization front sizes from literature (Henney & Arthur 1998; Ballering et al. 2023) versus as measured with MUSE IFU data. We note that the measurement methods differ slightly from each other.

uncertainty of the correlation coefficient by bootstrapping with 10^4 iterations while varying the y-axis values within their respective uncertainties. We adopted a truncated Gaussian distribution to model the uncertainty for the lower limits values in the R_{IF} measurements. In those cases, the bootstrapping was selected within this truncated Gaussian distribution with a standard deviation of 20% of the lower limit value. Both of these tests were then compared with the actual coefficient r_s. We also report the p-value of the null hypothesis randomizing the x-axis values. The p-value was calculated as the number of correlation coefficients larger (for positive correlation) than 1σ of bootstrapped observations, and divided by the number of iterations. We excluded proplyd 244-440 from the given test and those which follow.

We found p-value $\simeq 0.02$ and $r_s \simeq 0.62$, indicating a positive relation (Fig. 2.15a).

The sub-cube was too noisy for the measurement of R_{IF} in the case of 167-325 at [O II] 7330Å and [O III] 5007Å, and for proplyds 174-414 and 203-504 at [O III] 5007Å; they are not included in Fig. 2.4.

In Fig. 2.5, we show the comparison between our measurements of R_{IF} and those from the literature. The I-front radii of proplyds 154-346, 168-326, 170-337, 170-334, and 177-341W were derived by Henney & Arthur (1998), who fit models to observed Hα intensity profiles. Proplyd 168-326 is within the uncertainties of the literature values; proplyd 154-346 is a factor ~3.5 lower in the literature, and the rest are higher. The differences in the measured values could be explained by the measurement approaches.

Vicente & Alves (2005) measured the "chord diameters" of a sample of proplyds, in which 244-440 is common with our sample. The chord diameter is defined as the diameter of a circle

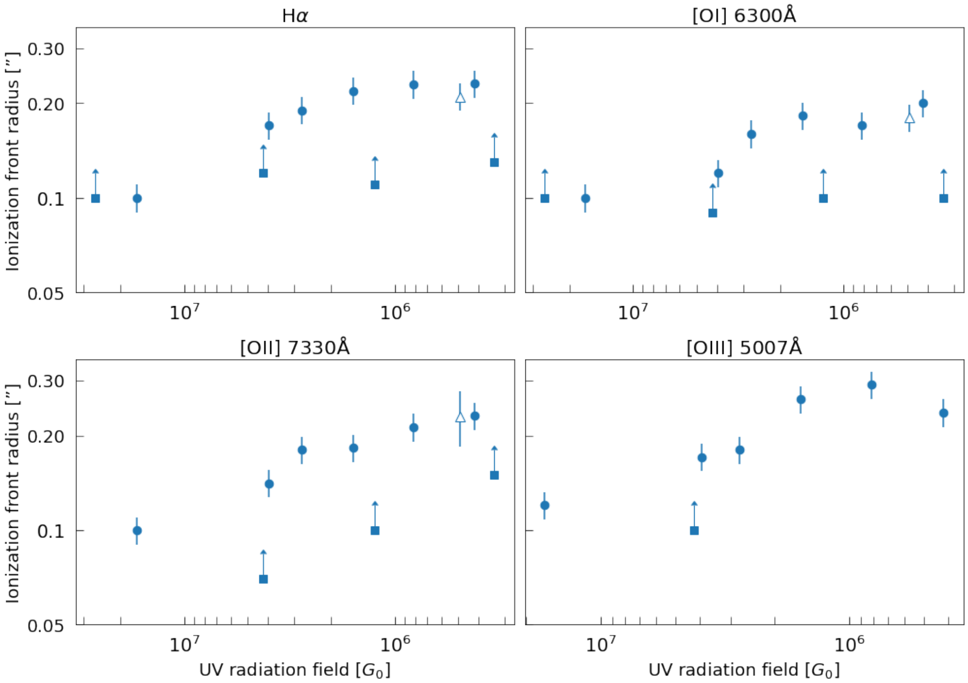

Figure 2.6: Ionizing radiation strength as a function of the ionization front radius. The diamond marks proplyd 203-504, irradiated mainly by θ^2 Ori A. For the rest of the targets (dots and squares), the UV source is θ^1 Ori C. Squares mark proplyds for which the I-front measurement has a higher uncertainty. 244-440 is not included in this figure due to the stark difference in size compared to the rest of the sample.

fitted to the contour of the proplyd cusp boundary, plus ∼30% the average background intensity. This approach places the I-front radius higher than our value, roughly at 2.8" or 1120 au; the measurement is not shown in Fig. 2.5 due to the great difference in size compared to the rest of the targets.

Recently, Ballering et al. (2023) estimated the I-front radii of proplyds 170-249, 170-337, 173-236, and 177-341W marking the disk center and the outer edge of the ionization front on surface brightness cuts of ALMA Band 3 images. Our values are systematically lower compared to the ALMA study, because the I-front marker was positioned past the peak's inflection point, not on the peak.

2.5.2 Ionization front radius and incident radiation field strength

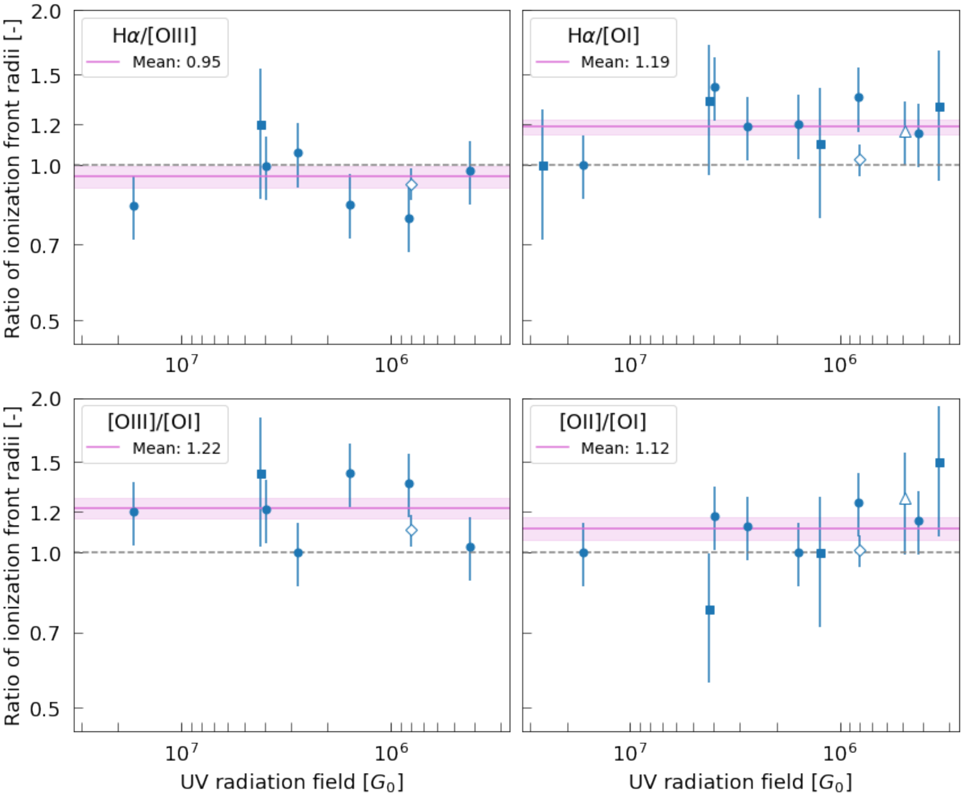

Figure 2.7: Ratios of ionization front sizes of Hα, [O III], [O II], and [O I] as a function of the incident UV field. The empty diamond marks 244-440, and the empty triangle marks 203-504. The mean and SEM are marked in violet.

The strength of the FUV environment is described in the units of the Habing radiation field; 1 $G_0 = 1.6 \times 10^{-3}$ erg cm^{-2} s^{-1} (Habing 1968). We calculate the strength of the incident radiation field using the following adimensional parameter:

$$F_{FUV} = \frac{1}{G_0}\frac{L_{\rm FUV}}{4\pi r^2}, \tag{2.1}$$

where the far-UV (FUV) luminosity $L_{\rm FUV}$ is derived from the values of FUV radiation reported as a function of stellar mass by Winter & Haworth (2022). The stellar mass was considered to be 45 $M_\odot$ for θ^1 Ori C and 39 $M_\odot$ for θ^2 Ori A (Simón-Díaz et al. 2006). The ionizing radiation strength for our sample spans from 10^5–10^7 G_0 over projected distances of 0.009–0.31 pc. These values are consistent with the literature: the FUV field incident upon most of the proplyds in the vicinity of θ^1 Ori C is estimated to be $F_{FUV} \geq 10^6$. For 244-440, the value is estimated to be on the order of $10^5 G_0$ assuming irradiation by θ^2 Ori A, which agrees with the value found by Vicente (2009). However, O'Dell et al. (2017) note that the proplyd may be ionized by both θ^1 Ori C and θ^2 Ori A, which would increase the radiation strength.

In Fig. 2.6, the I-front radii of the proplyds irradiated by θ^1 Ori C, as well as proplyd 203-504 irradiated by θ^2 Ori A, are plotted as a function of the incident UV radiation field. The I-front radii are larger at lower incident fields. We repeat the statistical test described above, and find $r_s \simeq$ -0.65, indicating a negative relation (Fig. 2.15b), and p-value $\simeq$ 0.02.
The proplyd 203-504, irradiated by θ^2 Ori A, follows very well the trend of the proplyds irradiated by θ^1 Ori C. The proplyd 244-440 appears to be much larger than any other proplyd, and it is not included in the figure.

To compare the different levels of ionization, we show the ratios of R_{IF} for the Hα line and for different forbidden oxygen lines as a function of the UV field in Fig. 2.7. We calculate the mean and its standard deviation for the following ratios. The ionization front radius increases for tracers that are more ionized: R_{IF}[O III]/ R_{IF}[O I] $\simeq 1.22 \pm 0.06 >$ R_{IF}[O II]/ R_{IF}[O I] $\simeq 1.12 \pm 0.06$. We see an increasing trend as expected, but the statistical significance is limited by the small sample size. More data would be needed for a firm confirmation. The same applies to the following case: $\mathrm{R}_{IF}\mathrm{H}\alpha/\mathrm{R}_{IF}$[O III] $\simeq 0.95 \pm 0.05$.

2.5.3 Mass-loss rate

In Fig. 2.4 (panel of Hα), the measured values of I-front radii are compared with predicted ionization front radii based on a set of mass-loss rates described by the following equation from Winter & Haworth (2022):

$$r_{\rm IF} \approx 1200 \left(\frac{\dot{M}_{\rm loss}}{10^{-8}\, M_\odot\,{\rm yr}^{-1}}\right)^{2/3} \left(\frac{\dot{N}_{\rm Ly}}{10^{45}\,{\rm s}^{-1}}\right)^{-1/3} \left(\frac{d}{1\,{\rm pc}}\right)^{2/3} \,{\rm au}, \tag{2.2}$$

where $\dot{M}_{\rm loss}$ is the mass-loss rate of the proplyd, d the projected separation from an irradiation source emitting $\dot{N}_{\rm Ly}$ ionizing photons per second. For θ^1 Ori C, we use $\dot{N}_{\rm Ly} = 1.60 \times 10^{49}$ photons s^{-1}, and $\dot{N}_{\rm Ly} = 1.08 \times 10^{49}$ photons s^{-1} for θ^2 Ori A, based on the values of stellar EUV luminosity as a function of stellar mass from Winter & Haworth (2022).

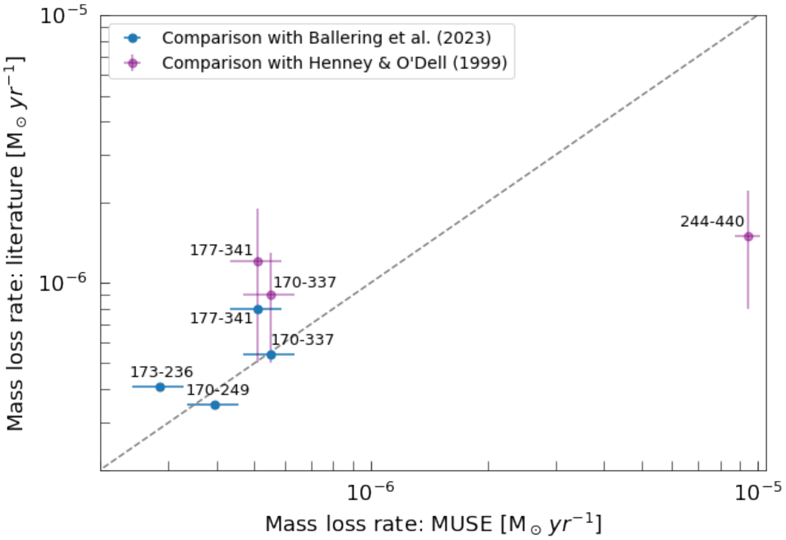

Figure 2.8: Mass-loss rates of MUSE compared with the values reported by Henney & O'Dell (1999); Ballering et al. (2023).

In the panel of Hα, of Fig. 2.4, curves for three different mass-loss rate values are partly overlapping with the data points, with $\dot{M}_{\rm loss}$ decreasing over larger projected distances, as expected from theoretical models of disk photoevaporation (e.g., Johnstone et al. 1998; Storzer & Hollenbach 1999). Four of the proplyds are at the curve marking 6×10^{-7} M$_\odot$ yr^{-1}, while the rest of the proplyds vary slightly more, falling between 1×10^{-6} and 3×10^{-7} M$_\odot$ yr^{-1}. The inferred $\dot{M}_{\rm loss}$ values are reported in Table 2.2.

The comparison of our estimates of $\dot{M}_{\rm loss}$ with values reported in the literature is shown in Fig. 2.8. The values are very consistent, except for 244-440 which has the highest $\dot{M}_{\rm loss}$ value in our sample, $\sim 8.06 \times 10^{-6}$ M$_\odot$ yr^{-1}. We discuss the values of $\dot{M}_{\rm loss}$ and the comparison with literature further in Sect. 2.6.3, and the case of 244-440 in Sect. 2.6.3.

To analyze how the estimated $\dot{M}_{\rm loss}$ of proplyds depends on the strength of the ionizing field, we plot the $\dot{M}_{\rm loss}$ values as a function of the incident UV radiation field in Fig. 2.9. This shows an increasing trend for $\dot{M}_{\rm loss}$ for the proplyds irradiated by θ^1 Ori C, moving from 10^6 to 10^7 G_0. Proplyd 203-504 also follows the trend relatively well. The proplyds with uncertain measurements of the I-front radii have a systematically lower value of $\dot{M}_{\rm loss}$, but the uncertainty in the measurement does not allow further considerations. We assessed the trend between $\dot{M}_{\rm loss}$ and G_0 with the statistical analysis described in the previous section. The Spearman correlation coefficient $r_s \simeq 0.84$, indicating a strong positive relation (Fig. 2.15c), and p-value $\simeq 0.001$, which indicates a very significant correlation.

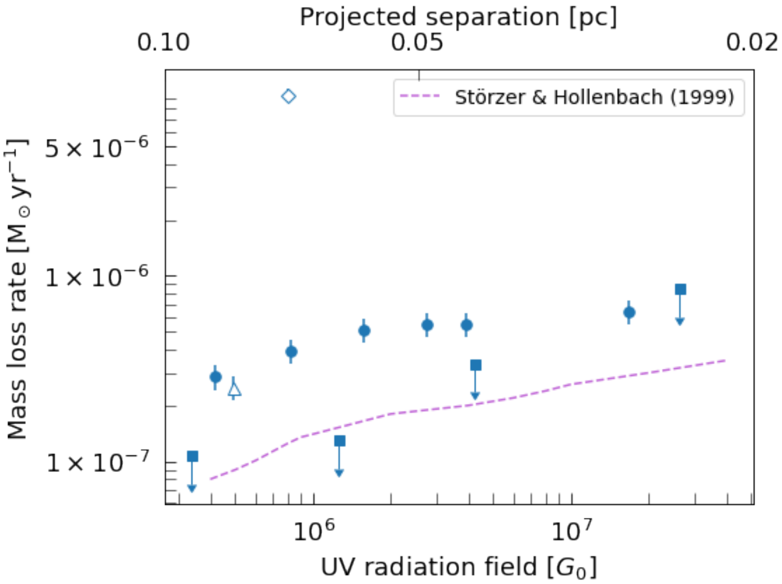

Figure 2.9: Mass-loss rate vs incident radiation field. The dots represent well-detected proplyds, and the squares denote the proplyds with higher uncertainty. The diamond (244-440) and the triangle (203-504) mark proplyds irradiated by θ^2 Ori A. The dashed purple line represents a model prediction for disks with a radius of 40 au (Storzer & Hollenbach 1999).

2.6 Discussion

2.6.1 Ratios of ionization front sizes

We have analyzed the MUSE IFU data of 12 proplyds to measure the I-front radii in four emission lines. The I-front radii as measured in different tracers reflect the ionization stratification in photoevaporating flow models (Henney & Arthur 1998), with the highest ionized flow spanning the furthest from the disk and closest to the UV source. Figure 2.7 underlines this ionization structure as R$_{IF}$[O III] > R$_{IF}$[O I], and R$_{IF}$[O III]/R$_{IF}$[O I] > R$_{IF}$[O II]/ R$_{IF}$[O I]. However, the statistical significance is limited by the small sample size.

We observe no dependency of the ratios on the impinging radiation, which indicates that the distribution of ionization front sizes of proplyds in the sample is self-similar: they have the same relative sizes at all levels of ionization, independently of the incident radiation. We provide a simple explanation of why this is expected, as follows.

Assuming equilibrium between ionizing flux from a massive star at distance d and gas recombinations, another way to express R$_{IF}$, following the analytic treatment of flows by Johnstone et al. (1998), is:

$$r_{IF} = \left[\frac{\alpha r_0^4 n_0^2}{3} \frac{4\pi d^2}{\dot{N}_i} \right]^{1/3} \tag{2.3}$$

where α is the recombination coefficient for the given ionized species, r_0 is the disk outer radius,

n_0 is the density of neutral material at the disk surface, and $\dot{N}_i$ the ionizing photon count. When considering the ratio between I-front radii of two emission lines, the influence of distance becomes negligible, and the ratio depends on α, and $\dot{N}_i$. Considering the same UV source, the ratio for [O I] and [O II], for example, would simplify as

$$\frac{r_{\rm IF,OII}}{r_{\rm IF,OI}} = \frac{(\alpha_{\rm OII}\dot{N}_{\rm OI})^{1/3}}{(\alpha_{\rm OI}\dot{N}_{\rm OII})^{1/3}} \tag{2.4}$$

In the case of a θ^1 Ori C like object, with $\dot{N}_{\rm OII} \sim 10^{47}$, $\dot{N}_{\rm OI} \sim 10^{49}$, $\alpha_{\rm OI} = 3.25 \times 10^{-13}$, $\alpha_{\rm OII} = 1.99 \times 10^{-12}$ (recombination coefficients from Draine (2011)) the ratio is ~9, so while it is expected to be insensitive to the distance of the proplyd from the UV source, the predicted magnitude of the ratio is too high from this simple analysis. The reason for this is that the above argument assumes a spherically diverging (R^{-2}) scaling of the density at all distances from the disk. In reality, at the hydrogen ionization front (which coincides closely with the singly ionized oxygen front) there is a sharp jump in temperature from tens/hundreds of Kelvin to $\sim 10^4$ K. That temperature jump is associated with a sharp increase in the flow velocity and a sharp decrease in the gas density (easily an order of magnitude). Furthermore, if material is being accumulated in a shell within the proplyd cusp then the density contrast between the proplyd and surrounding H II region can be even higher, which we explore below with a basic numerical photoionization calculation.

2.6.2 Photoionization models of the ionization front structure

The structure of the H II region around a θ^1 Ori C type star is well understood to have an inner zone of more highly ionized species such as O III and He II surrounded by a zone where hydrogen is still ionized but, for example there is neutral helium and only singly ionized oxygen (e.g. O'Dell 2001; O'Dell et al. 2017). In the case of the proplyds, the transition from [O III], to [O II] to [O I] is very sharp, as shown in Sect. 2.6.1, suggesting that the density is substantially higher than the ambient H II region.

Here we build a simple set of models to estimate the required density near the I-front in the proplyds. The purpose of these models is purely to determine the density of gas required to make the separation between the different oxygen emission features as small as observed. We are not aiming at producing a detailed model of the structure of the proplyds.

We ran 1D spherical photoionization equilibrium calculations with the TORUS Monte Carlo Radiative Transfer code (Haworth & Harries 2012; Harries et al. 2019). This included polychromatic radiation, the diffuse field. The species included are hydrogen, helium, oxygen, carbon, nitrogen, neon and sulfur. We set the dust abundance to a negligible value in these calculations.

Our model consists of a star with $T_{\rm eff}$ =39,000 K and radius $R_* = 10.6\,R_\odot$. The inner portion of the 1D spherical grid was then modeled to be representative of the "normal" H II region, in which the gas density is $100\,{\rm m_H\,cm^{-3}}$. If the medium were all at that density, the H II region would extend to around 3.3 pc. We then imposed a density enhancement at 0.1 pc from the UV source that is supposed to represent the denser medium associated with the proplyd cometary cusp. The increased density is then a free parameter of the models and we study the location of the oxygen ionization fronts. We note that it is not an issue if the separation between ionization fronts is not significantly smaller than the radius of curvature of the object in the 1D spherical model, since the required thickness for that to be the case would be inconsistent with the observed thickness for the real proplyds.

Figure 2.10 shows the oxygen ionization fractions as a function of distance from the density enhancement (i.e., the distance outside of the normal H II region and into the "proplyd") for different densities. At low densities the spacing between the different oxygen emitting zones is far larger than the extent of proplyds. At higher densities, at around a few $\times 10^5$ cm^{-3}, the model results in a spatial distribution of ionization states of oxygen consistent with what is typical for the observed proplyds.

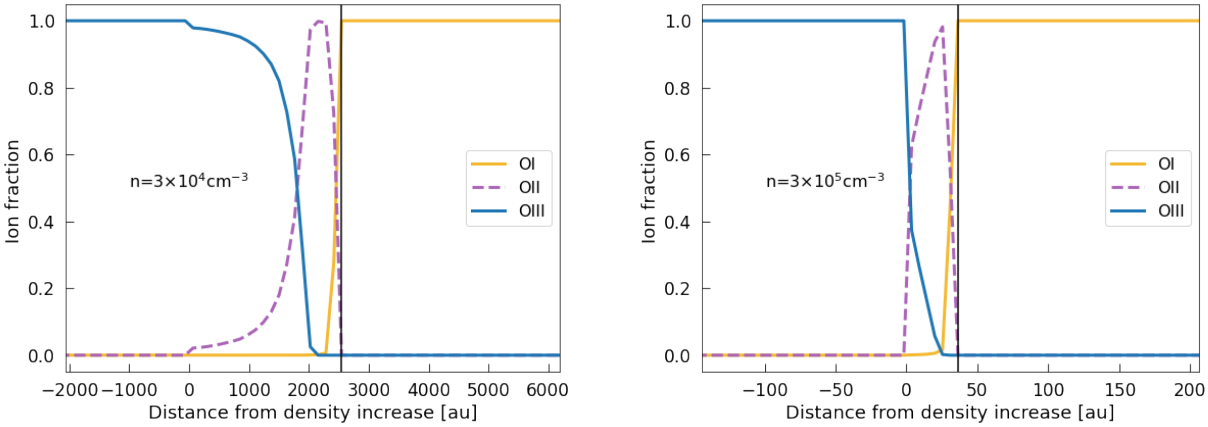

$n = 3 \times 10^4$ cm^{-3}

$n = 3 \times 10^5$ cm^{-3}

Figure 2.10: Example profiles of the oxygen ionization state as a function of distance from the density enhancement in the H II region (distance from the star of the proplyd cusp).

It is possible to broadly encapsulate the behavior here with the width of the O II zone. Figure 2.11 shows the scaling of that width as a function of the density enhancement beyond 0.1 pc. The scaling is approximately linear in log space, of the form

$$\log_{10}\left(\frac{\Delta(\mathrm{O\,II})}{\mathrm{au}}\right) = 8.18 - 1.21\log_{10}\left(\frac{n}{\mathrm{cm}^{-3}}\right) \tag{2.5}$$

Although this was derived for a proplyd at 0.1 pc from θ^1 Ori C, this distance is quite representative for our sample, as the projected separation are lower limits of the real distances. Furthermore, if the proplyd is closer, the proplyd would have to be even denser than predicted by Eq. 2.5 to achieve the same O II width. The same would be the case if the H II region density were lower. Overall these combine to make Eq. 2.5 a lower limit, in such a way that the empirical scaling of Equation 2.5 could be applied to give rough representative values of the density of cometary cusps across the ONC, which results in the typical values being $\sim 2 - 3 \times 10^5$ cm^{-3}. More detailed modeling is needed to precisely determine densities in proplyds using this approach, and we defer this analysis to future work. The densities predicted close to the I-front in our model

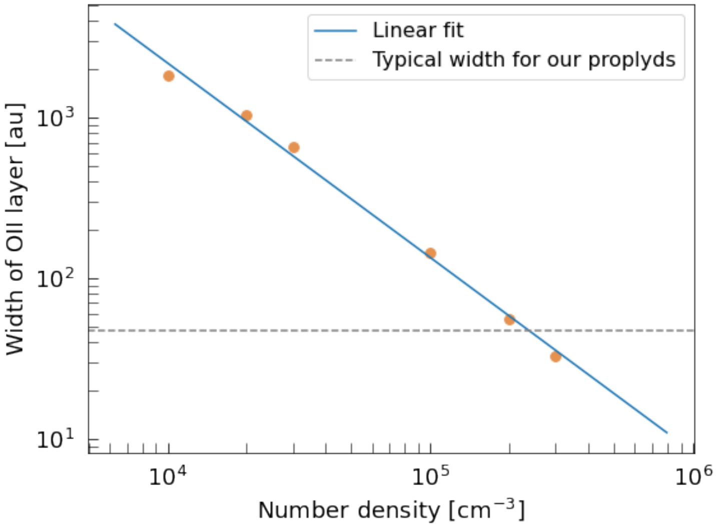

Figure 2.11: Distance between the O III-O II transition and the O II-O I transition for a proplyd at a distance of 0.1 pc from a θ^1 Ori C like star, as a function of the density in the cometary cusp of the proplyd. For densities $\sim 2-3\times10^5\ \mathrm{cm^{-3}}$ the thickness of the O II layer is consistent with our observations of ONC proplyds.

are consistent with the electron density estimates inferred from radio continuum observations of ONC proplyds by Ballering et al. (2023).

2.6.3 Mass-loss rate

Our estimates of the mass-loss rate employ the I-front radius, measured from the Hα line emission, following Eq. 2.2. The latter provides an upper limit on the mass-loss rate, since it neglects any possible extinction between the irradiating star and the proplyd. Indeed, clumps of dust between the ionizing source and the young stars can cause a total shielding of the ambient radiation field, as in the case of object 204-506, which does not show a cocoon of ionized material unlike the nearby 203-504 proplyd (Haworth et al. 2023b).

Figure 2.9 shows a decrease in the mass-loss rate with a smaller incident UV radiation field. This is in agreement with photodissociation models (Storzer & Hollenbach 1999), which consider that $\dot{M}_{\rm loss}$ is a slowly decreasing function of the UV field strength. The theoretical expectation is marked with the dashed line in Fig. 2.9. This prediction reproduces the increase of $\dot{M}_{\rm loss}$ with incident radiation observed in our measurements, but at lower $\dot{M}_{\rm loss}$ values. The offset is likely due to several assumptions, such as dust extinction, the outflow velocity, and the disk radius. The latter has a value of 6×10^{14} cm (40 au) in the plotted curve.

Proplyd 244-440 stands out as an outlier in Fig. 2.9 with $\dot{M}_{\rm loss}$ nearly an order and a half of magnitude larger than for the nearby proplyd 203-504. We discuss the properties of this object in the next subsection.

The curious case of 244-440

Proplyd 244-440 exhibits the widest cusp observed in the Trapezium. Past studies note that the giant proplyd is possibly irradiated by both θ^2 Ori A and θ^1 Ori C (O'Dell et al. 2017), evident from its multiple tails, although five times further from the latter (see Fig. 2.1). The complex environment might play a role in the unusual shape of 244-440; Haworth et al. (2023b) showed that the ONC is an environment where two YSOs can appear extremely different from each other regardless of their proximity.

The disk diameter of 244-440 has been estimated to be 387 au from HST-WFPC2 images (Vicente & Alves 2005). Using the higher spatial resolution observation of MUSE, the disk is roughly 300 au in diameter in the [O I]λ6300Å line. This is a particularly large size for disks in the ONC, smaller than the giant disk 114-426 (e.g., Miotello et al. 2012) but much larger than any other disk in this region, typically smaller than ~60 au in radius (Eisner et al. 2018). For a disk size of that order, exposed to a high UV radiation field ($> 10^5 G_0$), the models predict mass-loss rate $> 10^{-6}\,\mathrm{M_\odot\,yr^{-1}}$ (Haworth et al. 2023a), consistent with our estimation.

Despite standing out from the sample with its large I-front radius and high mass loss rate, 244-440 follows the same behavior as the rest of the objects in Fig. 2.7, with the ratios of its I-front radius being similar to the rest of the sample. This confirms a similar effect of the irradiation from the massive star(s) on the relative sizes of the I-fronts, as expected by the fact that they depend mainly on physical constants and, to a lesser extent, on the densities in the systems (see Sect. 2.6.1-2.6.2).

Given the rapid mass-loss rate, 244-440 is a unique object to be observed before its dispersal. Future observations with ALMA would clarify the disk properties and give insight into the evolution of the proplyd.

Dependence of mass loss rate on stellar mass

We have determined the stellar parameters for 10 targets in our sample. One half of the sample is classified as M spectral type (M0 and M5), and the other half is classified as mid-late K spectral type. The stellar masses range from 0.2 to $\sim$1 $\mathrm{M_\odot}$.

It is known that, in such a stellar mass range, several disk, accretion, and wind properties have a steep scaling with stellar mass (e.g., Manara et al. 2023). Although this sample is small, a correlation between $\dot{M}_{\rm loss}$ and stellar mass would be expected if the mass loss rate was driven by other processes than the irradiation from the ionizing stars, or if the stellar mass was a significant factor in setting the strength of the photoevaporating wind.

We explore the relation between $\dot{M}_{\rm loss}$ and stellar mass and find no correlation or dependence between the two parameters, which implies that mass loss is driven by the external UV source and depends on other properties, such as disk radii, but not (significantly) on the stellar mass. On the other hand, it is known that, in low-mass star-forming regions, the disk radii typically scale with stellar mass (e.g., Hendler et al. 2020). This is not the case in the ONC. Indeed, Vicente & Alves (2005) presented the disk diameter as a function of the SpT in a sample of 52 sources, and found no obvious correlation between the two.

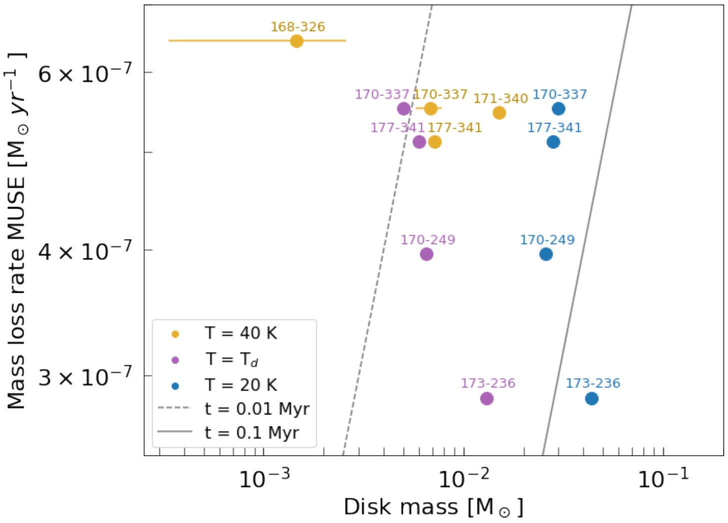

Figure 2.12: Mass-loss rates measured from the ionization front radius as a function of disk mass. The disk masses found by Mann et al. (2014) partly overlap with those reported by Ballering et al. (2023). Each colour represents a different assumed dust temperature: T=20 K, T=40 K, and T$_d$=62–108 K, and diagonal lines mark lifetimes.

Recently, Maucó et al. (2023) observed that the depletion of disk masses in the vicinity of the massive star σ-Ori is more pronounced for disks around stars with stellar masses higher than $\sim 0.4\,M_\odot$. Our sample is too small to firmly confirm or dispute this finding, but we do not find any significant difference in the measured $\dot{M}_{\rm loss}$ for the disks around stars more massive than 0.4 $M_\odot$. The reason could be a combination of the location and impinging radiation onto the disks, or the lack of a dependence on stellar mass. Future studies measuring both $\dot{M}_{\rm loss}$ and stellar masses should further explore this possibility.

2.6.4 Proplyd lifetime

The external photoevaporation process erodes material from the outer part of protoplanetary disks at a rate calculated here for our sample as $\dot{M}_{\rm loss}$. Here we investigate how long the disks we have observed can appear to survive under the effect of this process. In Fig. 2.12, we show $\dot{M}_{\rm loss}$ as a function of the disk masses measured with ALMA from continuum emission for seven proplyds from Mann et al. (2014) (reported as 100 × dust mass) and Ballering et al. (2023). The disk masses in the literature have been estimated by using different dust temperatures: Mann et al. (2014) assumed 40 K, while Ballering et al. (2023) computed the disk masses at both 20 K, and at temperatures that take external heating (Haworth 2021) by θ^1 Ori C into account for each proplyd in their sample. The values of disk masses for our targets are lower than typical disk populations in nearby low-mass star-forming regions. Indeed, the relation between disk masses and the projected separation from θ^1 Ori C have been studied by for example, Mann & Williams (2010), who found that the disks located within 0.3 pc from the massive star have lower masses. The low disk masses close to the UV source is also consistent with studies in different regions with lower but not negligible UV field, such as σ Orionis (Ansdell et al. 2017; Maucó et al. 2023) and NGC 2024 (Mann et al. 2015; van Terwisga et al. 2020). Interestingly, also in the latter region proplyds were observed with HST (Robberto et al. 2024). The $\dot{M}_{\rm loss}$ values are within the same order of 10^{-7} $M_\odot$ yr^{-1} for the available disk masses ($10^{-4} M_\odot$ – $10^{-1} M_\odot$).

The ratio between the disk mass and $\dot{M}_{\rm loss}$ gives an estimate of the expected lifetime of these systems, assuming that a constant $\dot{M}_{\rm loss}$ will affect them during their lifetime. Since other processes, such as accretion onto the star or internal winds, are predicted to remove mass from the disk at a rate that is orders of magnitudes lower (e.g., Alcalá et al. 2017; Manara et al. 2017b; Nisini et al. 2018), this ratio is the most constraining for the disk lifetime. Observational studies report mass loss (10^{-7}–10^{-6} $M_\odot$ yr^{-1}) similar to our estimates, and lifetimes < 1 Myr (e.g., Storzer & Hollenbach 1999; Henney et al. 2002; Ballering et al. 2023) for the proplyds. Here we have a larger sample of proplyds with both measured $\dot{M}_{\rm loss}$ and disk mass, and we derive photoevaporative timescale $t = M_{\rm disk}/\dot{M}_{\rm loss}$ in the range from 2.4 to 130 kyr (Fig. 2.12). These values are very short compared to the age of the region, making it peculiar that these objects are observed just before their final dispersal. Given these derived values, our results are in agreement with the literature values, conforming to this "proplyd lifetime problem".

Multiple works have explored solutions to the lifetime problem. Storzer & Hollenbach (1999) suggested that disks can survive much longer if they have radial orbits, and experience the highest mass-loss rate when they are closer to the ionizing stars, when they fly by in their vicinity. However, the dynamical models of the ONC were not found to be consistent with the suggestion (Scally & Clarke 2001).

The theoretical study by Winter et al. (2019) explored the survival of disks in the ONC by implementing a one-dimensional viscous evolution model, and highlighted that the mass loss rates inferred from observations of proplyds in the ONC are preferentially high, representing the most extreme values. Their model predicts $\dot{M}_{\rm loss}$ to be a factor of 2–3 lower for the majority of proplyds in their sample. The study also shows that part of the solution involves accounting for the age spread present in the stellar population of the ONC (e.g., Hillenbrand 1997; Palla & Stahler 1999; Da Rio et al. 2010; Jeffries et al. 2011; Beccari et al. 2017). In this scenario, the strongly irradiated stars are also the youngest and therefore have the greatest mass reservoir remaining. This represents a natural mechanism by which disks in the ONC can survive until the present day. Wilhelm et al. (2023) focused on modeling the radiation shielding by gas in massive star-forming regions, and showed that the disk lifetime could be extended by an order of magnitude by such shielding, making the lifetime problem milder. In the context of recent observational analysis, Ballering et al. (2023) suggested that disk masses are underestimated as a result of the ALMA emission being optically thick, which could play a role in solving the proplyd lifetime problem. Therefore, there are multiple factors to take into account when estimating the lifetimes of proplyds.

2.7 Conclusions

We have presented the first spatially and spectrally resolved observations of 12 proplyds in the Orion Nebula Cluster using MUSE NFM. We have characterized their morphology in different emission lines commonly associated with ionized gas, measured the size of the ionization front in different ionization tracers, and measured their stellar properties. This has allowed us to estimate physical parameters and draw comparisons with photoevaporation models. Our main conclusions are as follows:

- The ionization front radius traced by different emission lines (Hα, [O I], [O II], and [O III]) increases with decreasing strength of the FUV radiation field, as expected by photoevaporation models.
- The ratios of the ionization front radii for the emission lines of Hα, [O I] 6300Å, [O II] 7330Å, and [O III] 5007Å, shows the expected ionization stratification: the most ionized part of the flow is located closest to the UV source.
- The ratios of ionization fronts at the different ionization states explored in this work scale in the same way for all proplyds in our sample regardless of the incident radiation. This indicates that the ratio of ionization front sizes at different ionization states of proplyds is self-similar.
- Mass-loss rates, estimated based on the Hα emission, are of the order of 1.07–94.5 × 10^{-7} $M_\odot$ yr^{-1}. Higher $\dot{M}_{\rm loss}$ is observed at higher FUV field strengths, in line with general expectations from models. No dependence is observed with the stellar mass.
- The density of cometary cusps across the ONC should have typical values $\sim$ 2–3×10^5 cm^{-3} to explain the observed spatial distribution of ionization states of oxygen in proplyds.
- Observationally, the proplyd lifetime problem still holds even after new measurements of disk masses and mass loss rates have been performed.

This work sets the stage for identifying firm signatures associated with external photoevaporation, which would open the possibility of confirming whether disks located in more massive and distant star-forming regions undergo the effect. Moreover, the characterization of external photoevaporation is fundamental to constraining planet formation models.

Future work will involve analyzing line ratios as the tracers of electron density and temperature. Determining the physical properties of the proplyds will allow for a more precise measurement of the mass-loss rate. Additionally, the identification of new emission lines will be explored.

Acknowledgements

We thank the anonymous referee for the insightful review that improved our study. MLA, KM, and CFM acknowledge funding from the European Union (ERC, WANDA, 101039452). SF is funded by the European Union (ERC, UNVEIL, 101076613) and by the grant PRIN-MUR 2022YP5ACE. GPR is funded by the Fondazione Cariplo, grant no. 2022-1217, and the European Union (ERC, DiscEvol, 101039651). TJH acknowledges funding from a Royal Society

Dorothy Hodgkin Fellowship and UKRI guaranteed funding for a Horizon Europe ERC consolidator grant (EP/Y024710/1). Views and opinions expressed are however those of the author(s) only and do not necessarily reflect those of the European Union or the European Research Council. Neither the European Union nor the granting authority can be held responsible for them.

2.8 Appendix

2.8.1 MUSE NFM images of ONC proplyds

Figures 2.13 and 2.14 show each proplyd in a collage of the following emission lines: Hα, [O I] 6300Å, [O II] 7330Å, [O III] 5007Å, [S II] 6731Å, [N II] 5755Å, and [N II] 6584Å. These lines are selected to show the various components of the systems.

2.8.2 Statistical test

To asses the statistical significance of the relations in our small sample, we carry out two analyses for the following: ionization front radius (R_{IF}) and projected separation (d); R$_{IF}$ with UV radiation (G_0); and mass-loss rate ($\dot{M}_{\rm loss}$) with G_0.

Firstly, we test the null-hypothesis that there is no relation between the independent variable on the x-axis and the dependent variable on the y-axis. We use a bootstrap sampling method with 10^4 iterations, where we randomize the x values and compute the Spearman correlation coefficient. Secondly, we assess the uncertainty of the correlation coefficient by bootstrapping with 10^4 iterations while varying the y-axis values within their respective uncertainties taken as the standard deviation of a Gaussian distribution of random points. We adopt a truncated Gaussian distribution to model the uncertainty for the lower limits values in the R_{IF}, and thus also $\dot{M}_{\rm loss}$, measurements. In those cases, the bootstrapping is selected within this truncated Gaussian distribution with a standard deviation of 20% of the lower limit value. Both of these tests are then compared with the actual Spearman correlation coefficient r_s. The results are presented in Fig. 2.15.

2.8.3 Best fit of the stellar spectra

As described in Sect. 2.4.2, the extracted stellar spectra for the proplyds are compared with templates of young stellar objects to determine their spectral type and extinction. The best fit of the spectra are presented in Fig. 2.16.

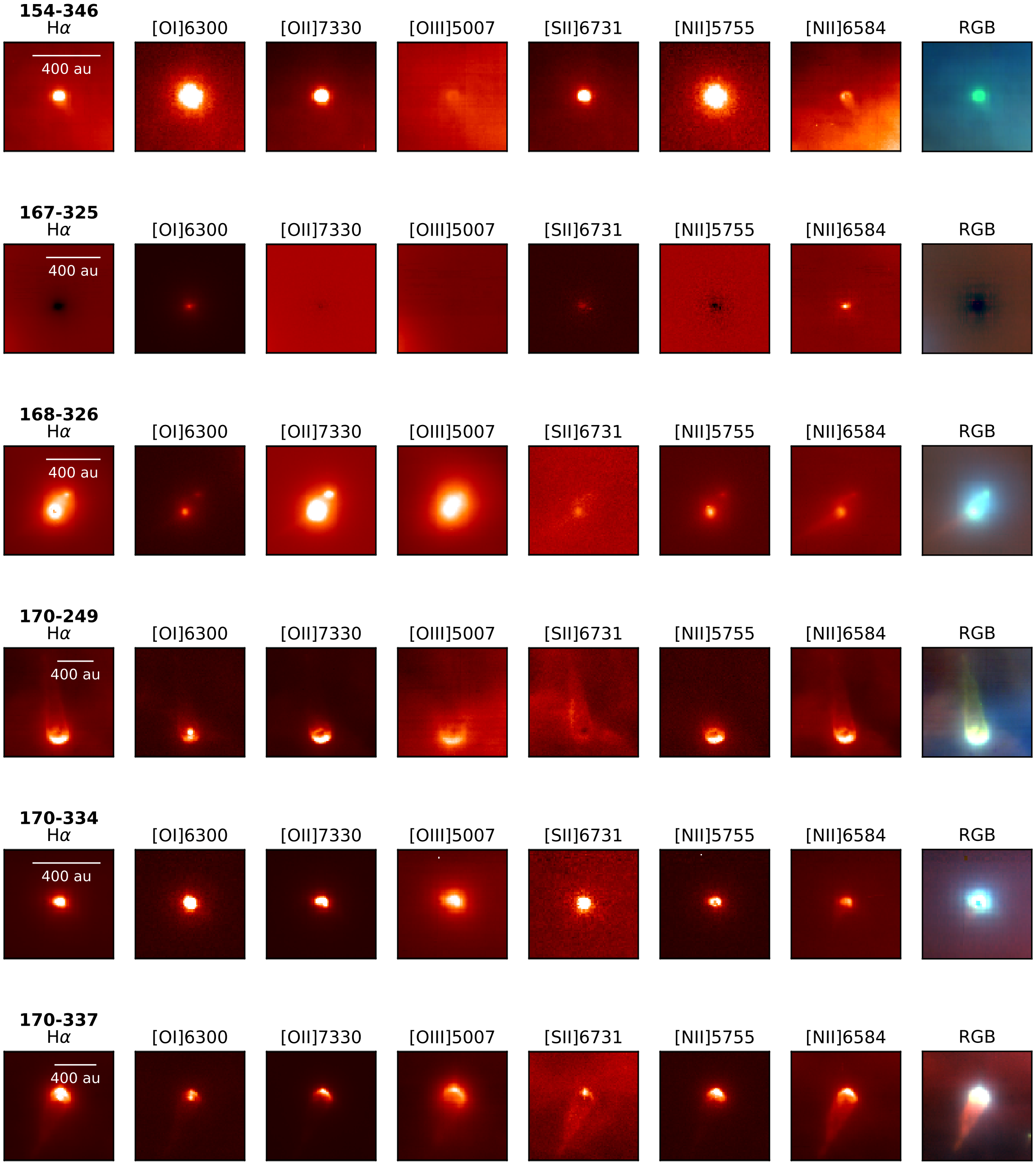

Figure 2.13: MUSE NFM observations of proplyds in seven emission lines. The last column is an RGB image combining [N II] 6548Å, Hα, and [O III] 5007Å emission lines.

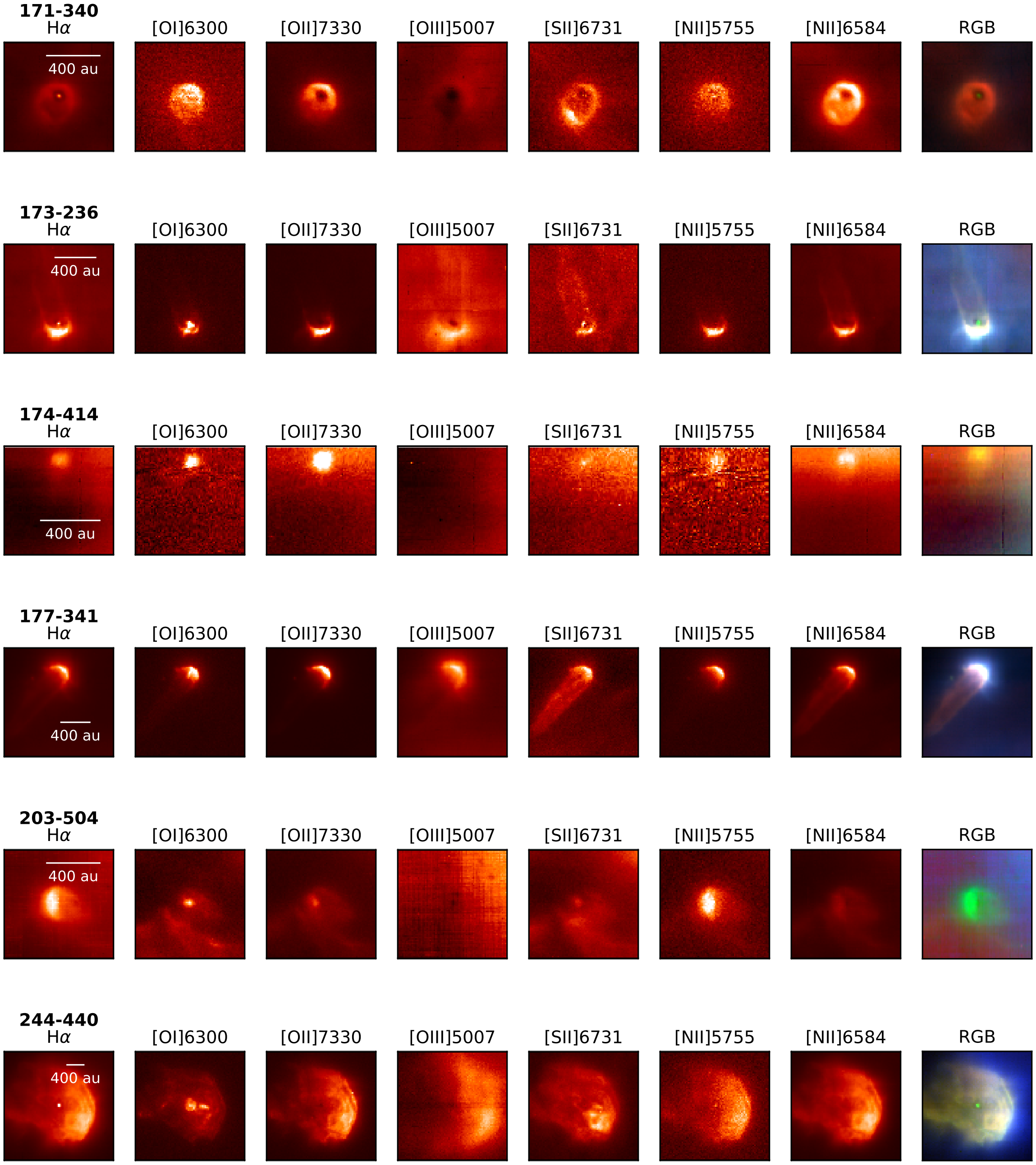

Figure 2.14: MUSE NFM observations of proplyds in seven emission lines. The last column is an RGB image combining [N II] 6548Å, Hα, and [O III] 5007Å emission lines.

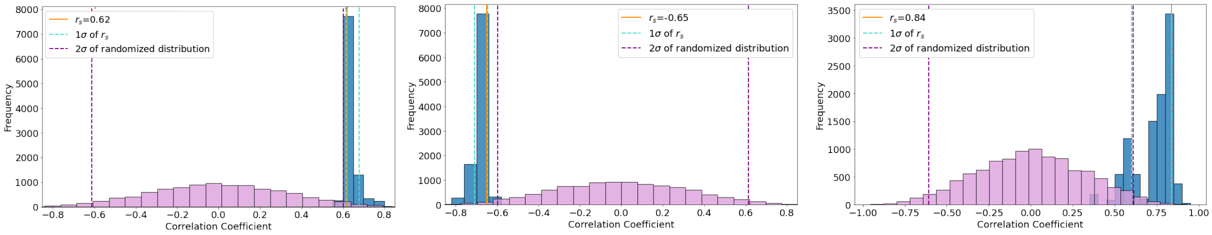

(a) (b) (c)

Figure 2.15: Correlation coefficient analysis for: (a) the ionization front radii and projected separation relation; (b) the ionization front radii and UV radiation relation; (c) mass-loss rate and UV radiation relation. The violet histogram corresponds to the bootstrapped randomized x-axis values; the dashed purple lines mark the 2σ ranges of the realizations. The blue histogram results from bootstrapping the y-axis values within the respective error bars, and the 1σ ranges of the bootstrap are shown with cyan line. We show that Spearman correlation coefficient for the measured data (orange line), which is outside 2σ of the randomized distribution.

2.8.4 Observations

The details concerning the MUSE NFM observations are given in Table 2.4.

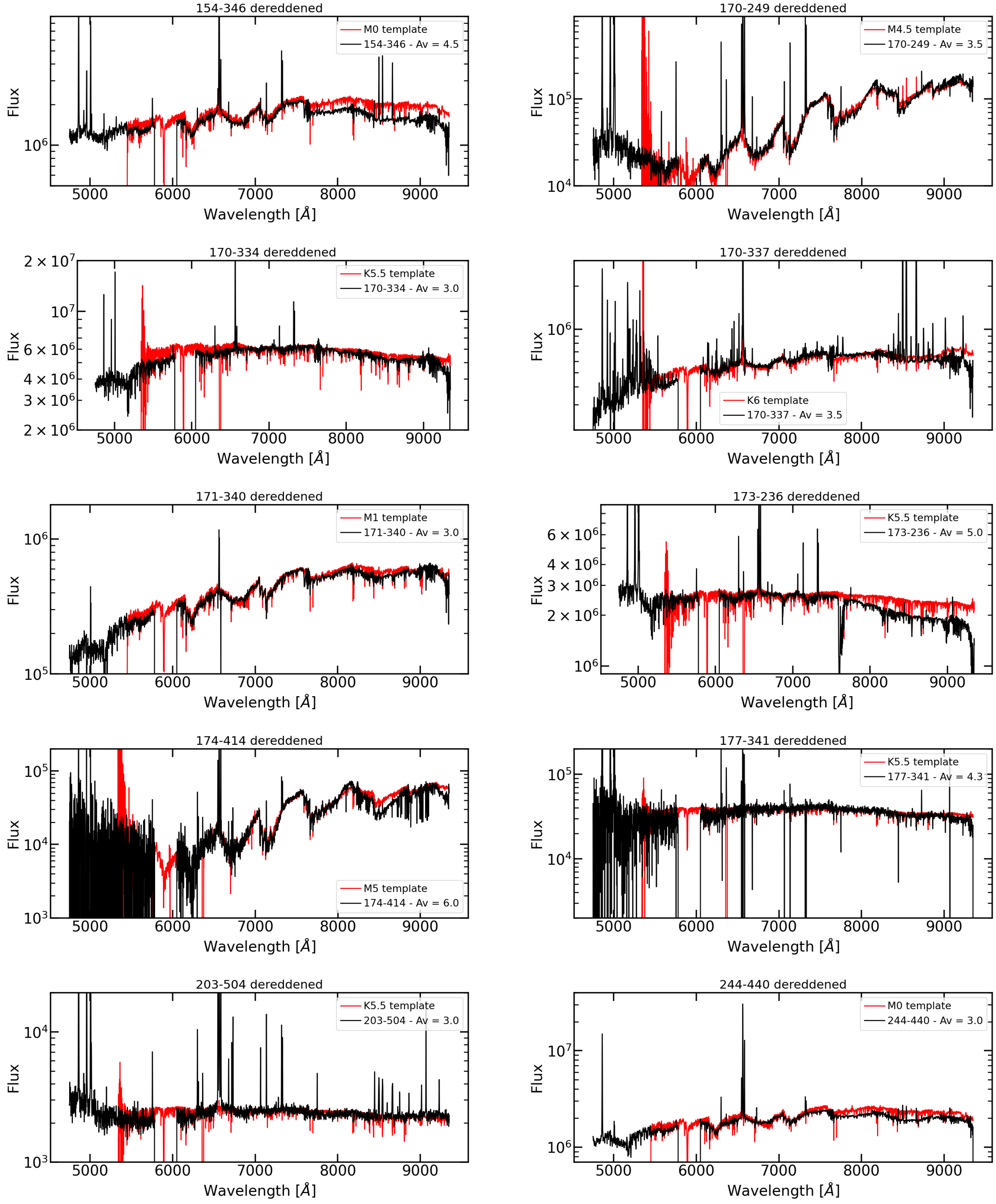

Figure 2.16: Best fit of the stellar spectra of the proplyds studied in this work.

Table 2.4: Information about the observations taken with MUSE NFM

Proplyd Name (1)	Observation date (2)	Exp. Time (3)	Seeing (4)	NEXP (5)	Airmass Start (6)	Airmass End (7)	Seeing Start (8)	Seeing End (9)	Tau0 (10)	Pr. Id (11)
142-301	2021-01-19 T04:37:43.619	360	0.84	3	1.262	1.288	0.89	0.8	0.005	A
159-350	2021-01-21 T01:40:53.355	729	0.81	3	1.071	1.067	0.5	0.52	0.007	A
167-231	2021-01-22 T02:17:52.677	340	0.62	3	1.06	1.061	0.64	1.08	0.005	A
168-326	2019-10-12 T07:53:02.561	400	1.25	3	1.098	1.089	1.13	0.74	0.0027	B
170-249	2021-02-20 T02:00:13.622	360	0.71	3	1.17	1.188	0.52	0.54	0.007	A
170-337	2021-01-21 T02:01:15.202	300	0.74	3	1.061	1.06	0.41	0.79	0.0065	A
173-236	2021-01-25 T03:54:24.967	300	0.84	2	1.201	1.218	0.6	0.6	0.0055	A
177-341W	2019-10-23 T07:23:13.289	380	0.82	3	1.083	1.076	0.9	1.01	0.0076	B
180-331	2021-02-06 T02:44:54.948	360	0.87	3	1.147	1.163	0.67	0.86	0.0084	A
203-504	2022-11-20 T04:45:50.432	660	0.91	4	1.154	1.131	0.55	0.57	0.0065	C
244-440	2019-10-23 T08:14:06.908	360	0.99	3	1.059	1.06	1.2	0.96	0.0063	B
HST-10	2021-03-25 T01:03:00.499	360	0.78	1	1.446	1.483	0.65	0.59	0.0043	A

Notes: Columns: (1) object, (2) date of observations, (3) exposure time per exposure, (4) airmass corrected seeing, (5) number of exposure, (6) airmass at start, (7) airmass at end of obs, (8) seeing at start, (9) seeing at end of obs, (10) coherence time, (11) Proposal ID. A: 106.218X.001. B: 104.C-0963(A). C: 110.259E.001.

3

A tell-tale tracer for externally irradiated protoplanetary disks: [C I] 8727 Å

This chapter is published as "A tell-tale tracer for externally irradiated protoplanetary disks: Comparing the [C I] 8727 Å line and ALMA observations in proplyds", Aru et al., 2024, A&A, 692, A137.

Full author list: **M. L. Aru**, K. Maucó, C. F. Manara, T. J. Haworth, N. Ballering, R. Boyden, J. Campbell-White, S. Facchini, G. P. Rosotti, A. Winter.

Abstract

The evolution of protoplanetary disks in regions with massive OB stars is influenced by externally driven winds that deplete the outer parts of these disks. The winds have previously been studied via forbidden oxygen emission lines, which also arise in isolated disks in low-mass star-forming regions (SFRs) with weak external UV fields in photoevaporative or magnetic (internal) disk winds. It is crucial to determine how to disentangle external winds from internal ones. Here, we report a proxy for unambiguously identifying externally driven winds with a forbidden line of neutral atomic carbon, [C I] 8727 Å.

We compare for the first time the spatial location of the emission in the [O I] 5577 Å, [O I] 6300 Å, and [C I] 8727Å lines traced by VLT/MUSE-NFM with the ALMA Band 7 continuum disk emission in a sample of 12 proplyds in the Orion Nebula Cluster (ONC). We confirm that the [O I] 5577 Å emission is co-spatial with the disk emission, whereas that of [O I] 6300 Å is emitted both on the disk surface and on the ionization front of the proplyds. We show for the first time that the [C I] 8727 Å line is also co-spatial with the disk surface in proplyds, as seen in the MUSE and ALMA data comparison. The peak emission is compatible with the stellar location in all cases, apart from one target with high relative inclination with respect to the ionizing radiation, where the peak emission is located at the disk edge in the direction of the ionizing radiation.

To verify whether the [C I] 8727 Å line is detected in regions where external photoevaporation is not expected, we examined VLT/X-Shooter spectra for young stars in low-mass SFRs. Although the [O I] 5577 Å and 6300 Å lines are well detected in all these targets, the total detection rate is $\ll 10\%$ in the case of the [C I] 8727 Å line.

This number increases substantially to a $\sim 40\%$ detection rate in σ-Orionis, a region with higher UV radiation than in low-mass SFRs, but lower than in the ONC.

The spatial location of the [C I] 8727 Å line emission and the lack of its detection in isolated disks in low-mass SFRs strongly suggest that this line is a tell-tale tracer of externally driven photoevaporative winds, which agrees with recent excitation models.

3.1 Introduction

The evolution of protoplanetary disks is affected by their surrounding environment. In massive clusters, the UV radiation from OB stars heats the gas in nearby protoplanetary disks, and gives rise to externally driven photoevaporative wind. This wind depletes the disk outside-in, causing rapid mass loss and a shorter disk lifetime (see Winter & Haworth 2022 for a review).

Irradiated disks, typically called proplyds, have been studied best in the Orion Nebula Cluster (ONC), where they exhibit a teardrop shape with an ionization front as imaged with the *Hubble* Space Telescope (HST; e.g., O'Dell et al. 1993; Bally et al. 1998; Ricci et al. 2008), and more recently studied with the Multi-Unit Spectroscopic Explorer (MUSE) instrument in narrow-field mode (NFM) at the ESO Very Large Telescope (VLT, Kirwan et al. 2023; Haworth et al. 2023b; Aru et al. 2024b) and with JWST (Berné et al. 2023, 2024; Habart et al. 2024) .

While external photoevaporation of disks is unique to clusters with massive stars, such as the ONC, internal photoevaporative winds due to the high-energy radiation from the central star (e.g., Ercolano & Pascucci 2017) may be present in high-UV environments and in low-mass star-forming regions (SFRs) with weak external UV fields. Internal disk winds may also be magnetohydrodynamically driven (see Pascucci et al. 2023 for a review). The forbidden emission lines, such as [O I] 5577 Å and [O I] 6300 Å, are commonly observed in conjunction with both internally driven winds (e.g., Natta et al. 2014; Simon et al. 2016; Fang et al. 2018; Nisini et al. 2018; Banzatti et al. 2019; Gangi et al. 2023) and externally driven winds (e.g., Bally et al. 1998; Tsamis et al. 2013). In distant clusters, the proplyd morphology cannot be spatially resolved. Furthermore, there may be no ionization fronts in regions where the extreme-ultraviolet (EUV) field is attenuated or negligible (e.g., Haworth et al. 2023b). These facts raise the question of how to identify external winds and how to disentangle them from internal ones. Ballabio et al. (2023) explore the line luminosity of [O I] 6300 Å as a diagnostic for external photoevaporation and predict it to undergo a dramatic increase above ~5000 G_0. However, it remains challenging to spectrally differentiate between internal and external winds without spatially resolving the system.

Here, we explore a proxy of externally driven winds, the near-IR forbidden line of neutral atomic carbon at 8727 Å covered by the MUSE-NFM data. Atomic carbon is predicted to be present in the upper layers of protoplanetary disks, where CO is dissociated by UV photons (e.g., Bruderer et al. 2012). Recently, [C I] 609 μm was detected in the isolated disk IM Lup with the Atacama Large Millimeter/submillimeter Array (ALMA) Band 8 observations, where it traces the disk atmosphere (Law et al. 2023), and in the irradiated disk d203-506 in the ONC, where it traces a photoevaporative wind (Goicoechea et al. 2024). Forbidden carbon lines at 8727 Å and 9850 Å were observed in emission in the ONC before the discovery of proplyds (Hippelein & Muench 1978 detected the two lines; Cosmovici et al. 1981 observed 8727 Å). Goicoechea et al. (2024) also report detecting the [C I] 9850 Å line in d203-506. Other carbon emission lines around ~ 1 μm were observed in the Orion Bar by Walmsley et al. (2000) and Peeters et al. (2024). Various permitted carbon emission lines in the same wavelength range were reported to be emitted in the inner regions of isolated disks by McClure (2019) and McClure et al. (2020), who did not detect near-IR carbon forbidden lines in these objects. More recently, [C I] 8727 Å

Table 3.1: Coordinates and projected separations of the sample of proplyds.

Proplyd	RA hh:mm::ss.s	DEC dd:mm:ss.s	d(UV source) [pc]
154-346	05:35:15.44	−05:23:45.55	0.068
167-325	05:35:16.72	−05:23:25.5	0.009
168-326	05:35:16.85	−05:23:26.22	0.012
170-249	05:35:16.96	−05:22:48.51	0.068
170-334	05:35:16.96	−05:23:33.6	0.028
170-337	05:35:16.97	−05:23:37.15	0.031
171-340	05:35:17.06	−05:23:39.77	0.037
173-236	05:35:17.34	−05:22:35.81	0.095
174-414	05:35:17.40	−05:24:14.5	0.106
177-341W	05:35:17.66	−05:23:41.00	0.049
203-504	05:35:20.26	−05:25:04.05	0.077 (θ^2 Ori A)
244-440	05:35:24.38	−05:24:39.74	0.06 (θ^2 Ori A) 0.31 (θ^1 Ori C)

Notes: The information is from O'Dell & Wen (1994); Bally et al. (2000); Ricci et al. (2008); Mann et al. (2014). For the given projected separations, d, the UV source is θ^1 Ori C with the exception of 203-504 (irradiated by θ^2 Ori A) and 244-440.

was detected in two irradiated disks in the ONC (Haworth et al. 2023b). This line, emitted at the 2.7 eV level in the transition $2p^2\ ^1D_2$, was theoretically studied by Escalante et al. (1991), as were two related forbidden lines at 9850 Å and 9823 Å. Escalante et al. (1991) reported that these lines originated from a combination of C^+ ions produced by photoionization in regions with a density greater than 10^5 cm^{-3} and radiation fields $\sim 10^3 - 10^6 G_0$, where G_0 is the interstellar field intensity. More recent models predict that the line is instead excited via far-ultraviolet (FUV) pumping and its intensity scales with G_0 (Goicoechea et al. 2024).

In this study, we build on these previous works to present strong evidence that the [C I] 8727 Å line can be used as a near-IR tracer for identifying externally photoevaporated disks by combining the information on the location of the emission in this line with that from the disk from 12 proplyds in the ONC observed with MUSE and with ALMA.

3.2 Data and analysis

3.2.1 Observational data

We use data from the 12 proplyds showing prominent ionization fronts firstly presented by Aru et al. (2024b). These objects were observed with the VLT/MUSE integral field spectrograph (Bacon et al. 2010). The coordinates of the targets are given in Table 3.1. MUSE was operated in NFM, which covers the wavelength range ~4750–9350 Å with a field of view of ~7.5" × 7.5". The observations were taken in three programs (Pr. ID 104.C-0963(A) and 106.218X.001, PI: C. F. Manara; Pr. ID 110.259E.001, PI: T. J. Haworth). We measured the angular resolution of the images in the full width at half maximum (FWHM) range ≈0.06-0.08" at ~8760 Å in our observations. Details regarding the observation and the data reduction process are described in Haworth et al. (2023b) for proplyd 203-504 and in Aru et al. (2024b) for the rest of the sample.

In addition, we use the ALMA observations of six targets (168-326, 170-249, 170-337, 171-340, 173-236, and 177-341W) performed in Band 7 (0.86 mm) with an angular resolution of 0.09". The ALMA Band 7 data trace thermal dust emission from the disk and are described in Eisner et al. (2018). Ballering et al. (2023) show that the Band 7 data do not trace the ionization front, which is instead traced by the Band 3 data as presented in their work. Lastly, we use the publicly available spectra taken with VLT/X-Shooter for the PENELLOPE Large Program (Manara et al. 2021) and those published by Maucó et al. (2023).

3.2.2 Data analysis

In the following analysis, we consider the [O I] lines at 5577 Å and 6300 Å and [C I] 8727 Å, observed with MUSE-NFM, and compare the location of the continuum-subtracted emission (see Aru et al. 2024b for details) with the locations of the ALMA disk continuum emission and the stellar continuum emission.

Alignment and spatial comparison

As MUSE-NFM is known to have an uncertain astrometric accuracy, it is necessary to align the MUSE cubes with the ALMA data before analyzing how the MUSE detections of [C I] 8727 Å, as well as [O I] 5577 Å and 6300 Å, emissions compare to the disk's dust observations of ALMA. The alignment was done by measuring relevant reference points in the MUSE and ALMA continuum images and shifting the coordinates of the ALMA image to align with MUSE.

In the case of 177-341W, we carried out the matching by using two background sources present in both the ALMA and the MUSE data. We refer readers to Appendix 3.5.1 for a more detailed discussion on this target and its alignment. For the remaining proplyds, we used a subcube of the MUSE observations nearly free of emission lines, showing the star continuum, at $\lambda \sim 674 - 678$ nm. We then aligned the location of the star, measured on the MUSE image, with the center of the disk in the ALMA continuum image. We considered the uncertainty on this alignment to be half the spatial size of the MUSE spaxels (0.0125") for all proplyds except 168-326, 174-414, and 203-504, for which the spaxel size 0.025" was used because the emission around the central star is more extended and therefore the location more uncertain.

In Fig. 3.1, the images of the ALMA Band 7 data are shown together with the line emission from MUSE, which is shown with contours representing 50%, 70%, and 90% of the peak intensity of the line emission. The proplyds are ordered starting from the smallest projected separation to θ^1 Ori C to the largest. The direction of the UV source is shown with an arrow. We report the inclinations of the disks, calculated from their deconvolved FWHM major and minor axes listed by Ballering et al. (2023) using the CASA task imfit on the ALMA data for proplyds 168-326 and 171-340.

We made a spatial comparison between the stellar emission location and the [O I] 5577 Å, 6300 Å, and [C I] 8727 Å line emission location to determine any spatial displacement. Figure 3.2 shows the MUSE stellar continuum emission and the contours of the emission lines in a similar way as Fig. 3.1. In Fig. 3.2 all 12 of the proplyds are shown, including those not observed with ALMA.

Radial cuts

In order to confirm that the line emission is spatially resolved and to analyze the shift of the emission lines in relation to the central star, we retrieved a radial cut for each proplyd in the MUSE emission line images. This was performed by calculating the emission along a 6"-long line centered at the coordinates of the central star and oriented toward the ionizing source θ^1 Ori C. The procedure is described in more detail in Aru et al. (2024b). In the case of 177-341W, we instead centered the radial cut line at coordinates corresponding to the center of the disk as seen in the ALMA image. This is because the disk is highly inclined and the coordinates of the central star cannot be determined in the same way as for other proplyds. This target is discussed in more detail in Appendix 3.5.1. Figures of radial cuts are described in Appendix 3.5.2 (available on Zenodo).

3.3 Results and discussion

Here, we describe the observed spatial location of the [O I] 5577 Å, 6300 Å, and [C I] 8727 Å lines observed with MUSE and how these compare with the disk emission traced by ALMA. Combining this information with an analysis of high-resolution spectra of young stars in low-mass SFRs, we show the potential of the [C I] line for tracing externally photoevaporated winds.

3.3.1 [OI] 5577 Å, 6300 Å lines in proplyds

The [O I] 6300 Å line was detected in some of the proplyds in the ONC with HST (e.g., Bally et al. 1998), while [O I] 5577 Å was detected in proplyd 182-413 (also known as HST-10) with VLT/FLAMES (Tsamis et al. 2013). We detect both lines in all 12 proplyds of the sample. Here, we introduce a comparison between these oxygen emission lines and the ALMA disk continuum emission.

The location of the [O I] 5577 Å, 6300 Å emission lines is typically well aligned with the disk's dust emission from ALMA, as shown in Fig. 3.1. The emission of [O I] 5577 Å coincides with the disk, which is seen the most clearly, due to the lowest noise, in proplyds 170-249 and 173-236. We note that these are the two disks with the largest projected separation from the ionizing source in the combined MUSE-ALMA sample shown here. In the MUSE-MUSE comparison of Fig. 3.2, proplyds 170-334, 154-346, 203-504, and 244-440 also show the coincidence of the [O I] 5577 Å emission with the disk, under the assumption that the star is centered

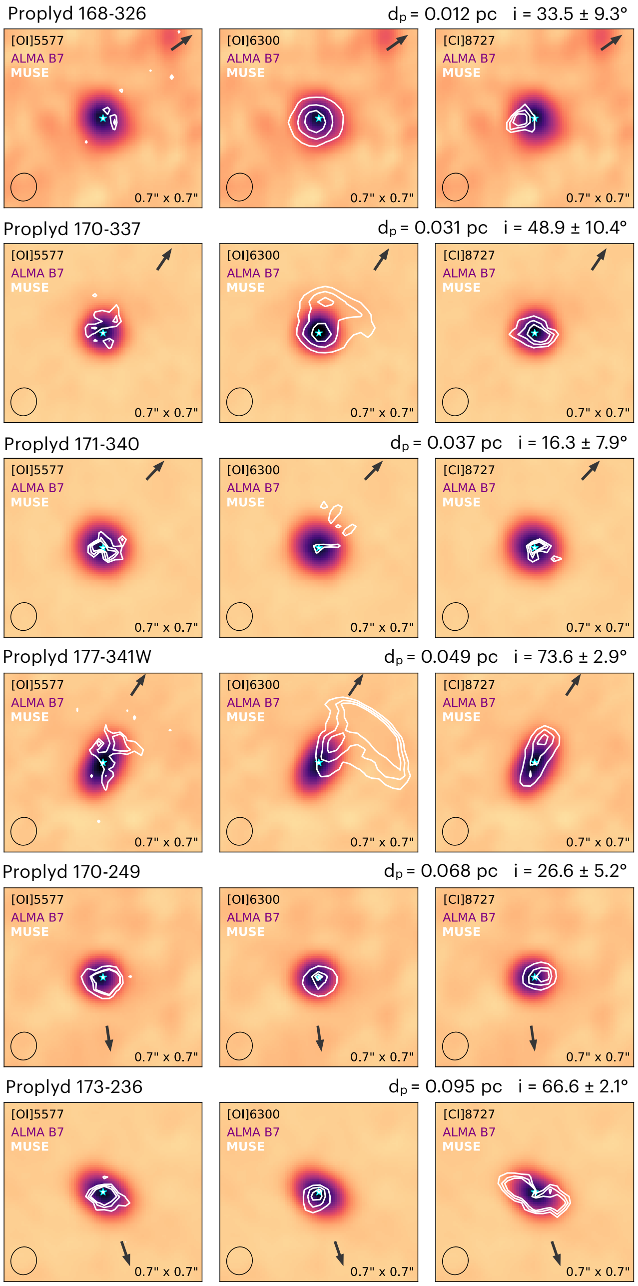

Figure 3.1: ALMA Band 7 images of proplyds 168-326, 170-337, 171-340, 177-341W, 170-249, and 173-236 compared with the MUSE emission lines (contours) at 50%, 70%, and 90% of the peak intensity; the rows are ordered in increasing projected distance from θ^1 Ori C. The ALMA Band 7 data were originally published by Eisner et al. (2018); the values for inclination marked above the figures are from Ballering et al. (2023), except for 168-326 and 171-340 (Ballering et al., in prep.). The MUSE emission lines are shown in the top left corner, the beam size is indicated in the bottom left corner, and the size of each image in the bottom right corner. The direction of the UV source is shown with an arrow. The cyan star marks the star's estimated location.

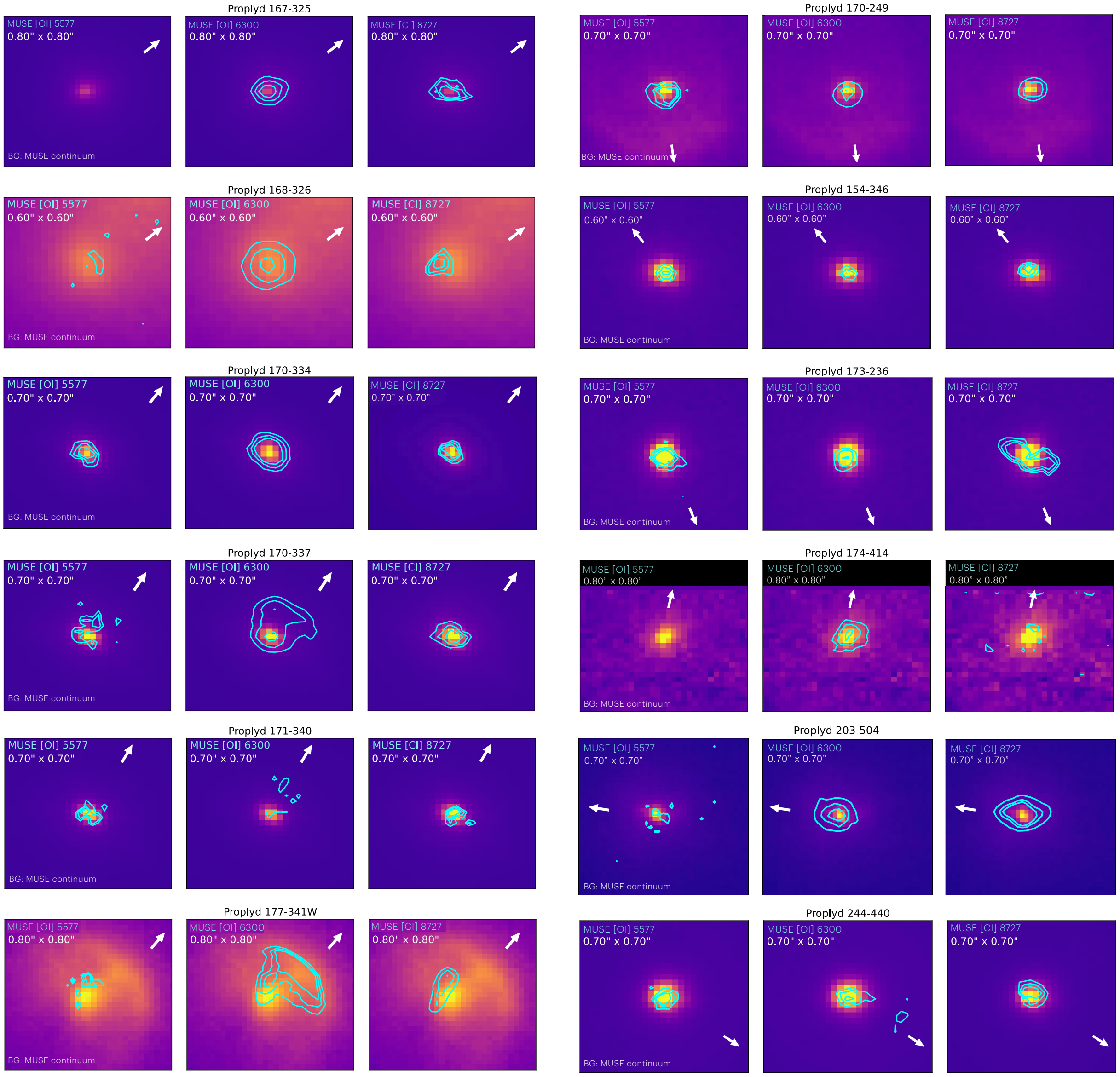

Figure 3.2: Spatial comparison between MUSE stellar continuum (colormap) and MUSE emission lines (contours) for proplyds 154-346, 167-325, 168-326, 170-249, 170-334, 170-337, 171-340, 173-236, 174-414, 177-341W, 203-504, and 244-440. The emission line and the size of each image are shown in the top left corner. The contours represent 50%, 70%, and 90% of the peak intensity of the MUSE emission lines, except for the [C I] line of 174-414 for which only 90% is shown. The direction of the UV source is shown with an arrow.

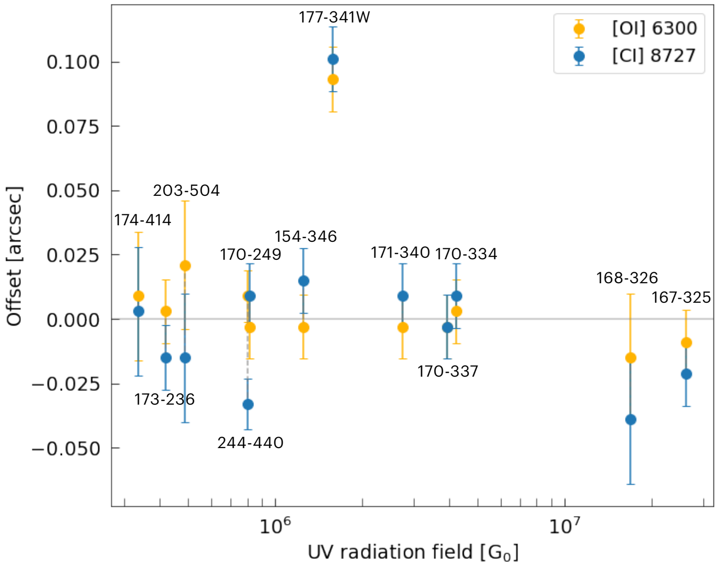

Figure 3.3: Offsets between the intensity peaks of forbidden line emission and the location of the star versus the UV radiation field. The peak in the radial cut of [O I] 6300 Å is marked in orange, and blue points mark [C I] 8727 Å.

at the center of the disk. For 167-32 and 174-414, the MUSE moment 0 map is too noisy for [O I] 5577 Å contours to be shown.

In a study of proplyd 182-413 (Tsamis et al. 2013), the line [O I] 5577 Å was found to peak at spaxels that coincide with the position of the disk and, therefore, align with our observations. We thus confirm that the [O I] 5577 Å emission originates on the disk surface.

The [O I] 5577 Å emission is not co-spatial with [O I] 6300 Å. The major difference between the two oxygen emission lines is that [O I] 5577 Å is only bound to the disk region and not emitted in the ionization front. The [O I] 6300 Å emission from the disk and the ionization front is connected in the contours for proplyds 170-337 and 177-341W; these locations match with the early observations described by Bally et al. (1998). Theoretical works have also predicted [O I] 6300 Å to trace multiple regions: the area near the disk surface, the photodissociation region, and the ionization front where oxygen is excited thermally due to collisions with H, H_2, and electrons (e.g., Störzer & Hollenbach 1998).

In Fig. 3.3 we show the displacement of the [O I] 6300 Å peak emission from the location of the star as a function of the UV radiation field. Values in the positive range of the y-axis mark a peak located in the direction of the UV source, and those in the negative range the opposite. These values are derived from the radial cuts (figures available on Zenodo), and given in Table 3.2. The values are compatible with no displacement within their uncertainties except for 177-341W, which has an inclined disk of i=73.6 ± 2.9 deg (Ballering et al. 2023).

To further investigate whether the offset of the emission peak is an effect related to the inclination of the disk relative to the UV source, we calculated the relative inclination of the disks using the spherical law of cosines: $\cos(\Delta i) = \cos(i_1)\cos(i_2) + \sin(i_1)\sin(i_2)\cos(\Omega_1 - \Omega_2)$, where

Table 3.2: Coordinates and projected separations of the detected proplyds.

Proplyd (1)	Offset, [O I] (") (2)	Offset, [C I] (") (3)	i (deg) (4)	PA$_d$ (deg) (5)	PA$_{d,\star}$ (deg) (6)
154-346	-0.003 ± 0.0125	0.015 ± 0.0125	...	...	38
167-325	-0.009 ± 0.0125	-0.021 ± 0.0125	...	...	126
168-326	-0.0150 ± 0.0250	-0.039 ± 0.0250	33.5 ± 9.3	31 ± 3	125
170-249	-0.0030 ± 0.0125	0.009 ± 0.0125	26.6 ± 5.2	68 ± 16	10
170-334	0.003 ± 0.0125	0.009 ± 0.0125	...	...	136
171-340	-0.0030 ± 0.0125	0.009 ± 0.0125	16.3 ± 7.9	41 ± 9	148
170-337	-0.0030 ± 0.0125	-0.003 ± 0.0125	48.9 ±10.4	85 ± 17	147
173-236	0.0030 ± 0.0125	-0.015 ± 0.0125	66.6 ± 2.1	60 ± 2	18
174-414	0.009 ± 0.0250	0.003 ± 0.0250	...	...	164
177-341W	0.0931 ± 0.0125	0.101 ± 0.0125	73.6 ± 2.9	152 ± 2	136
203-504	0.021 ± 0.0250	-0.015 ± 0.0250	...	...	75
244-440	0.009 ± 0.01	-0.033 ± 0.01	...	...	52

Notes: Column (1): Name of the proplyd. Column (2): Peak of [O I] 6300 Å emission measured from the location of the star in a radial cut; the sign indicates whether the peak is toward or in the opposite side from the UV source. Column (3): Similar to column (2) but for [C I] 8727 Å. Column (4): Inclination of the disk, calculated from the deconvolved FWHM major and minor axes of disks listed by Ballering et al. (2023) and Ballering et al., in prep., for proplyds 168-326 and 171-340. Column (5): Position angle of the deconvolved disk from ALMA data similarly to column (4). Column (6): Position angle between the disk and the UV source. As the inclination and PA$_d$ are measured from ALMA data; the values are not available for the whole sample.

Ω_1 is the position angle of the disk from ALMA, Ω_2 the position angle between the central star and the UV source, i_1 the disk inclination, and $i_2 = 90$ deg is the inclination we assume for the emission coming from the UV source in the plane of the sky. In Fig. 3.4, the displacements are shown as a function of the relative inclination. Proplyd 177-341W has the highest relative inclination, which could well explain the fact that the displacement arises from the disk's inclination relative to θ^1 Ori C. If the [O I] emission does mainly come from a wind on the surface of the disk, we would expect that this mainly arises from the edge of the disk on the side pointing toward the UV source θ^1 Ori C. In cases of low relative inclination, this effect is more difficult to see as the whole disk surface is irradiated, resulting in a more homogeneous emission. On the other hand, when the relative inclination is higher, then one side of the disk is more illuminated and the emission is stronger. This hypothesis needs confirmation on a larger sample of targets.

3.3.2 [CI] 8727 Å line in proplyds

The MUSE data provide the first detection of the [C I] 8727 Å emission line in proplyds (Haworth et al. 2023b). Here, we present for the first time a comparison between the [C I] 8727 Å emission and the ALMA dust emission, and the detection of this line in all 12 proplyds in our sample.

Firstly, the [C I] 8727 Å emission appears co-spatial with the ALMA disk emission. No contribution from the ionization front is present, and the line is emitted only from the disk surface and/or base of the externally photoevaporating wind. Compared to the contours of the [O I] λ5577, λ6300 lines, [C I] 8727 Å traces the disk shape more closely in the case of inclined disks 173-236 and 177-341W, as seen in Fig. 3.1. In the case of 173-236, the contours of [C I] 8727 Å follow an elliptical shape that coincides with the ALMA continuum image, rather than the circular contours of the [O I] 6300 Å emission line. The shape of the [C I] 8727 Å contours is also elliptical for 177-341W, whereas [O I] 5577 Å is not clear and the contours of [O I] 6300 Å are merged with the emission from the ionization front. For 170-337, [C I] 8727 Å also enables the disk to be located without noise or emission from the ionization front. Therefore, [C I] 8727 Å is a more accurate tracer of the disk surface and/or the base of the externally photoevaporating wind than the [O I] lines. Furthermore, the similarity between the gas radius and the dust continuum radius could potentially allow the [C I] 8727 Å emission line to be used for estimating the gas disk radius.

The [C I] 8727 Å emission is co-spatial with the MUSE stellar continuum emission for the rest of the proplyds in the sample (170-334, 174-414, 167-325, 154-346, 203-504, and 244-440). The stellar continuum, taken in an emission-line-free region of the MUSE cube between 8756–8764 Å, is shown in Fig. 3.2, together with the contours showing the location of the emission lines. When comparing the peak emission offset with the irradiation from the ionizing source on the targets (Fig. 3.3), including for the [C I] 8727 Å line, the biggest displacement is seen in 177-341W. For 177-341W, the [C I] 8727 Å emission peaks on the side of the disk facing toward the direction of the UV source. The offset between the center of the disk in the ALMA image and the peak of [C I] 8727 Å emission (MUSE) is shown as an outlier in Fig. 3.4, as the location of the star was assumed to be in the center of the disk. This peak implies that [C I] 8727 Å traces the surface of the disk and/or the base of the photoevaporative wind. Similarly to the discussion on

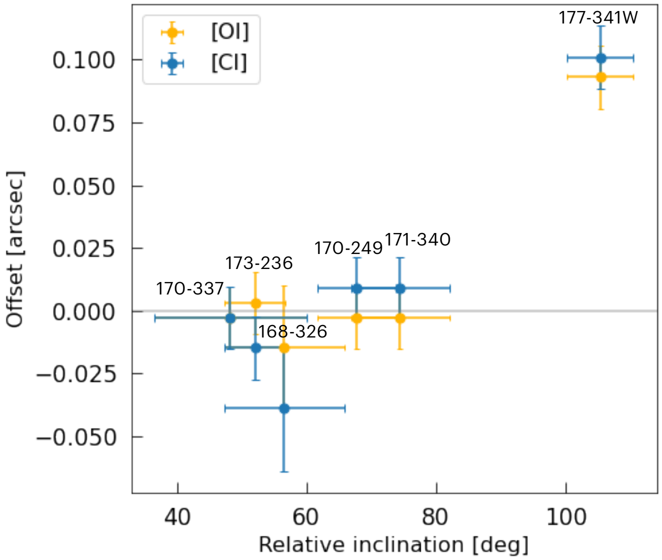

Figure 3.4: Offsets between the intensity peaks of forbidden line emission and the location of the star, versus relative inclination. A relative inclination of 0 deg would correspond to a disk being irradiated face-on, and of about 90 deg to an edge-on configuration. The peak in the radial cut of [O I] 6300 Å is marked in yellow, and blue points mark the offset of [C I] 8727 Å.

the [O I] line offset, the largest offset in this case may be due to the high relative inclination of this disk with respect to θ^1 Ori C. The targets with lower relative inclinations show a more uniform emission on the disk surface. The lack of measurements for disk inclination and position angle for half of our sample hinders the possibility of further confirming that this is due to the relative inclination of the disks and the external UV radiation. An example of the proplyd morphology based on 177-341W as observed with MUSE is shown in Fig. 3.5.

Proplyd 168-326 is another outlier in Figs. 3.3 and 3.4, with the peak of [C I] 8727 Å facing away from θ^1 Ori C. This proplyd has the second smallest projected separation (d_p=0.012 pc) from the UV source among the 12 targets. However, the contours of nearby proplyd 167-325 (d_p=0.009 pc) coincide with the location of the central star, as seen in Fig. 3.2. Therefore, it

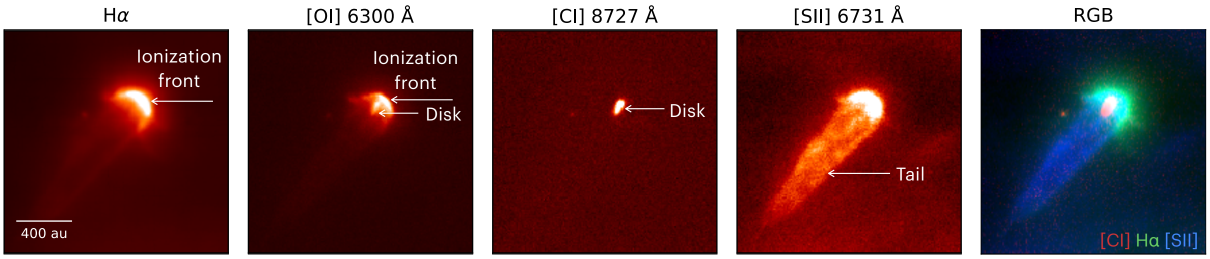

Figure 3.5: Continuum-subtracted, single-line integrated flux images and an RGB image of proplyd 177-341W. The panels show which parts of the system are visible in given emission lines.

is unclear whether the displacement of [C I] 8727 Å could be explained by the small projected separation. We also note that, for this target, the offset is still compatible with zero, and therefore it is harder to conclude any statistically sound difference.

Finally, we note that 244-440 also has a peak offset of the [C I] 8727 Å line slightly larger than zero and in the opposite direction of the ionizing radiation (Fig. 3.3). We note, however, that this is a peculiar target, possibly irradiated by two UV sources (O'Dell et al. 2017). The properties of this proplyd are discussed in more detail in Aru et al. (2024b) and it will be the subject of future studies.

3.3.3 The [CI] 8727 Å line as a tracer of externally photoevaporated disks

The spatial location of the [C I] 8727 Å emission strongly suggests that this line originates on the disk surface and/or the base of the externally photoevaporating wind. It is interesting to verify whether this line also traces disk winds in low-ionization environments, where external photoevaporation is not at play. This is the case for the [O I] lines, routinely detected in isolated disks in low-mass SFRs and interpreted in those environments as tracers of internal - photoevaporative or magnetohydrodynamic (MHD) - winds (Pascucci et al. 2023, for a review).

To verify whether the [C I] 8727 Å line is also typical in disks in low-mass SFRs, where external photoevaporation is not expected, we examined 74 VLT/X-Shooter spectra from the PENELLOPE Large Program (Manara et al. 2021, regions such as ϵ Cha, Lupus, and Taurus) and 45 VLT/X-Shooter spectra from the study of σ-Orionis by Maucó et al. (2023). The [O I] 5577 Å line is detected in 68% of the targets, and the [O I] 6300 Å line in 88% of the targets in the PENELLOPE sample (Campbell-White, in prep.). In contrast, only one target shows a clear detection of the [C I] 8727 Å line in the PENELLOPE sample, with seven additional tentative detections, for a total of a $\ll 10\%$ detection rate. This number increases substantially to a $\sim 40\%$ detection rate in σ-Orionis, a region with higher UV radiation than low-mass SFRs, but lower than the ONC. It is to be expected that a good fraction of the targets in this region are indeed experiencing external photoevaporation winds. Lastly, we detect this line in all 12 proplyds in the ONC observed with MUSE/NFM. The lack of detections in isolated disks is consistent with McClure (2019) and McClure et al. (2020), who did not detect IR carbon forbidden lines in the innermost regions of isolated disks, where instead they detected several permitted carbon lines. In the same disks, previous works had detected forbidden lines of [O I] in the vast majority of the targets (Natta et al. 2014; Nisini et al. 2018).

This notable difference in detection rates between the [O I] optical lines and the [C I] 8727 Å lines in disks in low-mass SFRs strongly points to the fact that this line is emitted in highly externally irradiated environments. This is in agreement with the results found by Escalante et al. (1991), who pointed to high external UV flux in cluster environments, such as the one experienced by proplyds, for this line to be emitted. We note that they considered the 10^3–10^6 G_0 FUV field range, and that the FUV field of our targets expands this range into lower values, with 10^2 G_0 in σ-Orionis and a higher range for the proplyds closest to θ^1 Ori C in the ONC (167-325 and 168-326; 10^7 G_0). Our results are in even greater agreement with the FUV-pumping excitation models of Goicoechea et al. (2024). Their models also predict that the intensity of the IR carbon lines scales with G_0. This dependence should be explored in future works. As expected from these models, the emission of [C I] 8727 Å is confined to the disk and/or base of the externally photoevaporating wind, and does not appear on the ionization front, in agreement with the fact that these are not recombination lines. The detection rate, together with the coincidence of the emission with the disk surface, strongly suggest that the [C I] 8727 Å line is emitted in an externally photoevaporated wind and does not suffer from confusion with line emission due to internal processes, such as in the cases of the [O I] lines, known tracers of internal processes (e.g., Ercolano & Pascucci 2017), and external winds (e.g, Ballabio et al. 2023).

3.4 Conclusions

In this work, we compared the spatial location traced by VLT/MUSE-NFM of the emission in the [O I] 6300 Å and [O I] 5577 Å lines, as well as in the [C I] 8727 Å line, with the ALMA Band 7 continuum disk emission in a sample of 12 proplyds in the ONC. We confirm that the [O I] emission is co-spatial with the disk emission for the [O I] 5577 Å line, whereas that of [O I] 6300 Å is emitted both on the disk surface and on the ionization front of the proplyds. At the same time, we show for the first time that [C I] 8727 Å is also co-spatial with the disk surface in a proplyd, as seen in the MUSE and ALMA data comparison. The peak emission is compatible with the stellar location in all cases, apart from one target with high relative inclination with respect to the UV radiation, where the peak emission is located at the disk edge in the direction of the UV radiation.

We have presented the [C I] 8727 Å emission line in the 12 proplyds that were observed with MUSE in NFM, with a detection rate of 100%. In contrast, this line has a much lower detection rate in other SFRs, and this rate decreases to become compatible with zero detections in the nearby low-mass SFRs. This result strongly supports the recent excitation models of neutral carbon in externally irradiated disks proposed by Goicoechea et al. (2024). On the other hand, [O I] lines at 5577 Å and 6300 Å are common in low-mass SFRs, as they are also related to internal disk winds, and this contamination makes them a less direct tracer of externally driven winds.

Our results strongly suggest that:

- The [C I] 8727 Å line traces the base of the externally photoevaporated wind, can act as a key tracer of the wind, and is ideal for distinguishing winds in disks that are not externally photoevaporated, such as in low-mass SFRs.

- This emission can be particularly valuable for identifying external irradiation when there is no ionization front or proplyd morphology visible (as in the case of d203-506; Haworth et al. 2023b).

- As the dust continuum radius is very similar to the gas radius, the [C I] line could be a potential tracer of the gas disk radius (and by extension, the gas-disk size distribution) in irradiated environments, which is set to be explored in future works.

Our work highlights the strength of using the [C I] 8727 Å line as a proxy for tracing external photoevaporation. With VLT/MUSE, it may be systematically easier to detect large samples of externally photoevaporated gas disks in massive clusters, and to study the global spatial extents of the dust versus gas at large samples in combination with ALMA.

Future studies should aim to study the kinematics of this line by using spectral resolutions inaccessible with MUSE-NFM, to confirm that this line is tracing a slow wind, as expected from externally photoevaporated winds (Ballabio et al. 2023). Additional surveys with ALMA should be carried out to measure the disk inclination and position angles, as well as the disk sizes, in a larger number of proplyds, which are to then be combined with the MUSE data to further decipher their physical conditions.

Data availability

Additional data for this article are available at `https://zenodo.org/doi/10.5281/zenodo.14002504`.

Acknowledgements

We thank the anonymous referee for detailed comments and useful suggestions, which improved our work. MLA, KM, CFM, and JCW are funded by the European Union (ERC, WANDA, 101039452). GPR is funded by the European Union (ERC, DiscEvol, 101039651) and by the Fondazione Cariplo, grant no. 2022-1217. SF is funded by the European Union (ERC, UNVEIL, 101076613), and acknowledges financial contribution from PRIN-MUR 2022YP5ACE. TJH acknowledges funding from a Royal Society Dorothy Hodgkin Fellowship and UKRI guaranteed funding for a Horizon Europe ERC consolidator grant (EP/Y024710/1). GB is supported by the European Research Council (ERC) under the European Union's Horizon 2020 research and innovation programme (Grant agreement No. 853022, PEVAP). Views and opinions expressed are however those of the author(s) only and do not necessarily reflect those of the European Union or the European Research Council Executive Agency. Neither the European Union nor the granting authority can be held responsible for them.

This paper makes use of the following ALMA data: ADS/JAO.ALMA #2015.1.00534.S. ALMA is a partnership of ESO (representing its member states), NSF (USA) and NINS (Japan), together with NRC (Canada), NSTC and ASIAA (Taiwan), and KASI (Republic of Korea), in cooperation with the Republic of Chile. The Joint ALMA Observatory is operated by ESO, AUI/NRAO and NAOJ.

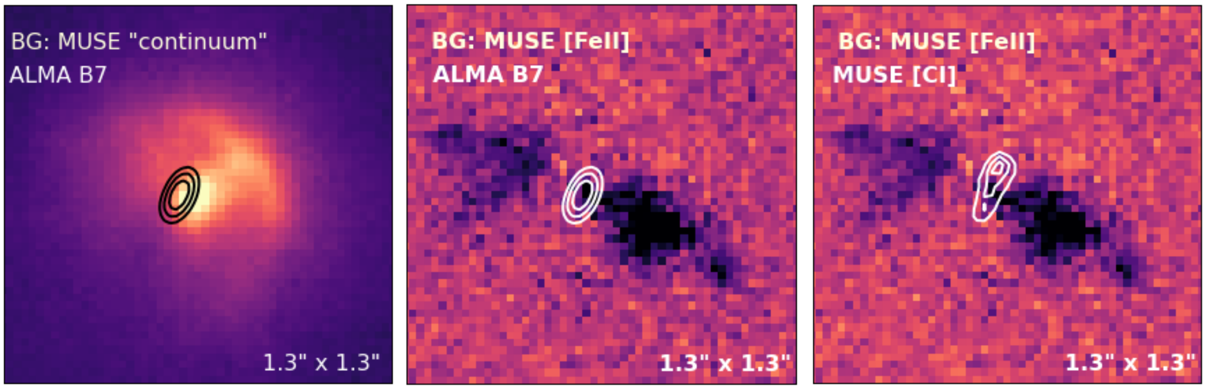

Figure 3.6: Proplyd 177-341W shown for three cases: 1) the stellar continuum emission in the background, overlaid with the contours of ALMA Band 7 data; 2) [Fe II] 8892 Å (MUSE) in the background, overlaid with the contours of ALMA Band 7 data; 3) [Fe II] 8892 Å (MUSE) in the background, overlaid with the contours of [C I] 8727 (MUSE).

3.5 Appendix

3.5.1 The case of proplyd 177-341W

With Fig. 3.6, we investigate the location of the disk (observed in ALMA band 7) with respect to the subcube nearly free of emission lines (left-most panel) and the jet as seen in the emission line [Fe II] 8892 Å observed with MUSE (middle panel). We also show the [C I] emission observed with MUSE as overlaid on the moment 0 map showing the jet (right-most panel).

The jet pinpoints to the center of the disk and therefore the location of the star, further indicating that the peak of the emission in the left-most panel is misaligned from the true location of the star. The case of 177-341W is similar to the scattered light images of highly inclined disks studied by Villenave et al. (2020).

3.5.2 Additional figures

The figures available on Zenodo show: (1) the [C I] line at 8727 Å in the 12 proplyds is shown. The spectra were extracted from continuum subtracted cubes of wavelength range 8660–8760 Å on the emission, by using a circular aperture of 0.1"; (2) the radial cuts of 12 proplyds for the MUSE stellar continuum, and the moment 0 maps of [O I] 5577 Å and [C I] 8727 Å emission. These radial profiles were taken in the direction of the UV source, and allowed us to measure the peak of the emission lines with respect to the location of the star; (3) the spectra of eight tentative detections of the [C I] 8727 line, out of 74 targets observed with VLT/X-Shooter. The clearest detection is seen in the case of AA Tau.

4

MUSE observations of proplyds in the Orion Nebula Cluster. II. Line ratios and physical properties of proplyds

This chapter is to be submitted to A&A, authored by **Aru, M. L.**, K. Maucó, C. F. Manara, T. J. Haworth, et al.

Abstract

Winds of different origin play a key role in dispersing protoplanetary disks and shaping their evolution into planetary systems. Most stars form in massive clusters with high UV fields, where OB stars irradiate disks and drive externally photoevaporative winds. These winds can be traced by optical forbidden emission lines, although similar lines also arise in isolated disks due to internal photoevaporative or magnetically driven winds.

We investigate commonly observed forbidden-line ratios in the Orion Nebula Cluster (ONC) proplyds, and compare them with other star-forming regions to distinguish internal and external winds. We present ratio maps and analyze their spatial variation. The aim of this part of the study is to inform future observations in spatially unresolved regions. We further link the observed ratios to the physical properties of proplyds.

Our analysis is based on spatially resolved observations of irradiated disks in the ONC, focusing on the [O I] λ6300, [N II] λ6583, and [S II] $\lambda\lambda$6731, 6716 lines. We also explore ratios that can serve as temperature and density diagnostics.

We confirm that [N II]/[S II] is a more reliable tracer of external winds than [O I]/[N II]. Additionally, the [N II]/[S II] ratio is in agreement with theoretical predictions. The line ratios vary significantly within proplyds, depending on whether the emission arises in the cusp or the tail, and they are consistent with electron densities reported in the literature. The available optical ratios for diagnostics remain limited, but future BlueMUSE observations would provide access to a wider set of lines.

4.1 Introduction

Protoplanetary disks of gas and dust are the formation sites of planets. Several processes contribute to the dispersal of the disk material, including accretion onto the central star (e.g., Hartmann et al. 2016; Manara et al. 2023, for reviews) and winds of different origin. The interplay of these processes sets the properties of disks at the time of planet formation, but many of their aspects are the subject of ongoing study.

Photoevaporative and magnetohydrodynamic winds can be driven by the central star, that is, internally to the system (e.g., Ercolano & Pascucci 2017; Lesur 2021, for reviews). In the nascent environment of stellar clusters, photoevaporative winds acting on the disk can also be launched by stars external to the system. The OB-type stars heat the outer layers of the disk and lead to the loss of material via external photoevaporation (Winter & Haworth 2022).

This process is observed in proplyds—objects which exhibit a cloud of ionized gas surrounding the disk. Proplyds have been extensively studied in the Orion Nebula Cluster (ONC), the nearest massive star-forming region at ~400 pc from the Sun (Menten et al. 2007a; Kounkel et al. 2017) with an estimated age of 1–3 Myr (e.g., Reggiani et al. 2011). The landmark observations of proplyds in the ONC were carried out with the *Hubble* Space Telescope (HST; e.g., O'Dell et al. 1993; Bally et al. 1998; Ricci et al. 2008). Recently, proplyds have been extensively studied at sub-mm and radio wavelengths using ALMA and VLA (Ballering et al. 2023; Boyden et al. 2025), in the optical with the ESO Very Large Telescope (VLT) Multi-Unit Spectroscopic Explorer (MUSE) instrument in narrow-field mode (NFM) (Kirwan et al. 2023; Haworth et al. 2023b; Aru et al. 2024b), and at mid-infrared wavelengths with JWST (Berné et al. 2023, 2024; Habart et al. 2024). In the ONC, proplyds can be spatially and spectrally resolved. The ability to resolve the proplyds allows us to determine the physical quantities, such as the mass-loss rate, needed to constrain models of external photoevaporation.

Higher mass stellar clusters such as NGC 6357, and Tr 14 in the Carina Nebula lie at larger distances of 1.69 kpc and 2.3 kpc respectively. Studying the proplyds of those regions as clearly as in the ONC requires higher spatial resolution and sensitivity. While JWST has made such distant irradiated disks accessible for detailed spectroscopic studies in mid-infrared (Ramírez-Tannus et al. 2023, 2025; Frediani et al. 2025), they remain spatially unresolvable with existing facilities. Therefore, identifying and interpreting external photoevaporation in higher-mass but further away clusters calls for ways which do not rely on resolving the proplyd morphology.

The different types of disk winds can be traced and studied by optical forbidden lines. For disks in low-mass star-forming regions (SFRs), lines such as [O I] 5577 Å and [O I] 6300 Å, [N II] 6548 Å and [N II] 6583 Å, and [S II] 4068 Å are widely used to characterize internal winds and their spectral components (e.g., Hartigan et al. 1995; Rigliaco et al. 2009; Natta et al. 2014; Banzatti et al. 2019; Whelan et al. 2021). These emission lines also trace external winds. The MUSE observations spatially distinguish where the emission lines are emitted: for example, the [O I] 6300 Å line is emitted just above the disk surface, and also at the ionization fronts of proplyds (e.g., Ballabio et al. 2023; Aru et al. 2024a). This raises the question of how to distinguish the processes that contribute to this emission. The emission line [C I] 8727 Å has recently been proposed as a compelling tracer of externally driven winds, as it is known to be

FUV-pumped and only observed in highly irradiated environments (Goicoechea et al. 2024; Aru et al. 2024a). While the [C I] line is a powerful tracer, it is detected only in the reddest part of the spectra, which warrants further study of more commonly observed forbidden lines.

Rigliaco et al. (2009) identified an externally photoevaporated disk in the σ-Orionis cluster, strong in [S II] and [N II] emission. In addition to analyzing their line profiles, they measured the ratio of these forbidden optical lines and found them to differ from the targets in low-mass SFRs and the ONC. Maucó et al. (2025) provided a new look at the spectral line characteristics in σ-Orionis and measured ratios for 15–30 targets. They observed that the [O I] λ6300/[S II] ($\lambda\lambda$6716, 6731)[1] ratio is similar to the targets in Taurus. In contrast, the ratio including [N II] is higher for σ-Orionis targets — a signature pointing to external photoevaporation. Line ratios are promising in telling the internal and external photoevaporative winds apart, and therefore identifying whether a disk is irradiated. Peake et al. (2025) developed an approximate model of the emission lines, determining which line ratios are most sensitive to the distance from an OB star to identify externally photoevaporation in distant regions.

Line ratios are known to be sensitive to the physical properties of the emitting gas, and can therefore be used as independent tracers of density and temperature in proplyds (following e.g., Vasconcelos et al. 2005b). With the density known, the mass loss rate can be inferred independently from other estimates, such as photoevaporative flow models (e.g., Storzer & Hollenbach 1999; Henney & O'Dell 1999), and radio free–free emission (Ballering et al. 2023).

Here, we explore various emission line ratios based on the VLT/MUSE NFM observations of proplyds in the ONC presented by Aru et al. (2024b). We also present line ratio maps for the aforementioned ratios, as well as maps for additional ratios of various species: such maps provide a way to interpret the observed ratios and predict which parts of the proplyds emit strongest in different chemical species. For this reason, these maps are made available to the community [2]. In Sect. 4.2, we describe the extinction correction, continuum subtraction, and background subtraction of our data. In Sect. 4.3, we report the observed line ratios and compare them with literature estimates, and link the ratios to the physical properties of proplyds. We discuss the implications of these results and conclude in Sect. 4.4.

4.2 Analysis

4.2.1 Observations

We use data of 12 proplyds, which were observed with the VLT/MUSE integral-field spectrograph (Bacon et al. 2010), and presented in Aru et al. (2024b). MUSE was operated in NFM, which covers the wavelength range ~4750–9350 Å with a field of view (FOV) of ~7.5" × 7.5". The observations were taken in three ESO programs (Pr. ID 104.C-0963(A) and 106.218X.001, PI: C. F. Manara; Pr. ID 110.259E.001, PI: T. J. Haworth). Details regarding the observations are described in Haworth et al. (2023b) for proplyd 203-504, and in Aru et al. (2024b) for the

---

[1] [O I] 6300 Å/([S II] 6716 Å+[S II] 6731 Å)

[2] The maps will be made available with the publication of the work.

remainder of the sample. The angular resolution of the images in our observations is in the range FWHM≈0.06-0.08".

4.2.2 Extinction correction

The Orion Nebula is expected to have relatively low foreground extinction, as it lies nearly 20° below the Galactic plane at a distance relatively close to us. Extinction maps show that the extinction varies within the nebula itself, with regions of the Dark Bay and the southwest cloud showing the strongest extinction (O'Dell et al. 2008; Weilbacher et al. 2015). In order to estimate the extinction towards our targets, we must thus estimate this value locally around the proplyd. In the following, we use a procedure similar to McLeod et al. (2016) to derive the reddening along the line of sight.

We created pixel-by-pixel maps of extinction values for each of the ~7.5" × 7.5" observed fields of view by using the Python package `PyNeb` (Luridiana et al. 2015). For each pixel (i, j), we: (1) used sub-cubes of the wavelength range 4852–4870 and 6555–6570 Å with Hα and Hβ emission lines, respectively, to compute their ratio; (2) derived the coefficient c(Hβ), comparing the observed ratio to the theoretical value 2.86; (3) derived visual extinction A$_V$ using the formula of Robberto et al. (1993):

$$A_V^{(i,j)} = 2.5 \cdot c(H\beta)^{(i,j)} \cdot f(5460) \tag{4.1}$$

The extinction curve of Cardelli et al. (1989) was used, adapted by O'Donnell (1994); Blagrave et al. (2007) in the optical ("CCM89 oD94" in `PyNeb.RedCorr`), with R$_V$ = 5.5; this is in line with e.g., Weilbacher et al. (2015).

We then created a map of A_V values in each FOV; we defined a mask for each target to exclude the emission from the proplyd, and interpolated the values for the masked region. We assumed that the proplyd lies on the same line of sight as the nebula, setting A_V for each proplyd based on the values around it. These maps were created with the `Background2D` class from the Photutils Python library, which interpolates the values for the masked region. We describe the method further in the next section. The A_V values are in the range of 0.73–1.43, except for the proplyd 168-326 with $A_V \approx 3.75$ mag. These values are within the typical A_V range of 0–2 mag estimated in the ONC (Da Rio et al. 2010; Manara et al. 2012).

By using the map, we applied the correction factor $10^{0.4A_\lambda}$ to the intensities of each pixel in all cubes. We then continue to the next steps with these extinction-corrected cubes. The maps are shown in Figures 4.11 and 4.12.

4.2.3 Continuum and background subtraction

For the stellar emission, continuum subtraction was performed in the spectral direction on sub-cubes spanning ~100 Å. We masked out the emission lines in these sub-cubes, and the estimation of the continuum was performed by doing a linear fit to the unmasked regions in the spectrum at each spatial pixel (spaxel). From these continuum-subtracted sub-cubes we then created moment0 maps of the emission lines of interest.

Proplyd	d_p (pc)	A_V
154-346	0.068	0.73
167-325	0.009	0.24 (revise this)
168-326	0.012	3.75
170-249	0.068	1.42
170-334	0.028	1.02
170-337	0.031	1.14
171-340	0.037	1.48
173-236	0.095	1.36
174-414	0.106	0.79
177-341W	0.049	1.43
203-504	0.077 (θ^2 Ori A)	1.18
244-440	0.06 (θ^2 Ori A) 0.31 (θ^1 Ori C)	1.01

Table 4.1: Projected separations and mean A_V values, taken inside the defined mask for each proplyd.

In order to remove the nebular emission without affecting the target itself, we created 2D background maps excluding the target which we then used for subtraction. We used the `Background2D` class, which includes the following parameters: `box_size`, `filter_size`, `fill_value`, `sigma_clip`, `mask`.

A `SigmaClip` object is created with `sigma=3.0` to iteratively remove pixels that deviate more than 3σ from the local mean, helping to exclude outliers. The background is estimated locally by dividing the image into a grid of small boxes; the box size is typically `(8,8)` pixels. We typically set the filter size low, ranging from `(1,1)` to `(5,5)`, indicating minimal smoothing using a median filter. Any invalid regions are filled with zero (`fill_value`=0). We defined masks for each proplyd: a rectangular region containing the proplyd is excluded from the background estimation. For some of the targets, the masks are rotated. Having defined the parameters, the `Background2D` object stores the estimated background in `bkg.background`. Finally, the background is subtracted from the original image. An example for the 2D background map and the resulting subtracted map is shown in Fig. 4.1. The rightmost figure in Fig. 4.1 shows a histogram of the intensity values in the background (excluding the target) before and after subtraction, with the noise becoming centered around zero. Figures 4.14 and 4.15 show the maps for the full sample.

4.2.4 Measurement of line ratios

In the literature, the measurements of line ratios are based on spatially unresolved observations of slit spectroscopy. To reproduce similar measurements for comparison, we integrated the emission from the moment0 map over the mask, which comprises a given proplyd. For a comparison with the values measured in σ-Orionis and in low-UV SFRs such as Taurus, the

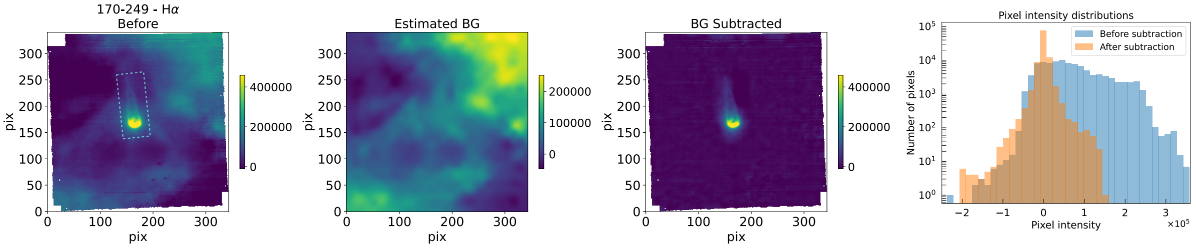

Figure 4.1: Example of background subtraction based on proplyd 170-249. From left to right: Hα moment0 map before background subtraction with the mask's coordinates overlaid, estimated 2D background, background-subtracted moment0 map, pixel intensity distributions before and after the subtraction.

emission lines [O I] λ6300, [N II] λ6583, and [S II] λ6731, and λ6716 were considered. Furthermore, MUSE allows us to measure spatially resolved line ratios to determine how the ratios vary in different parts of the proplyds. In addition to the aforementioned lines, we measured [N II] ($\lambda\lambda$6548,6583)/[N II] λ5754, [S II] λ6312/[S III] λ9068, and [O I] λ5577/[O I] λ6300. We produce additional ratio maps, potentially of interest for model comparisons: [O I] λ6300/[N II] λ6584, [O I] λ6300/Hα, [S II] λ6731/[O III]λ4959, [S II] λ6717/[S II] λ6731, [S II] λ(6717,6731)+[S III] λ9068/Hβ.

4.3 Results and discussion

4.3.1 ONC ratios: comparison with other environments and maps

Empirically estimating the line ratios provides a way to understand the origin of forbidden emission lines and help us disentangle the inner winds from the external ones. Such an approach was taken by Rigliaco et al. (2009), who measured the line ratios of SO587, a photoevaporating disk in σ-Orionis, and compared them to those in Orion proplyds and disks in low-mass SFRs. Maucó et al. (2025) analyzed high-resolution MIKE spectra for 27 classical T Tauri stars and complementary intermediate-resolution X-shooter data in σ-Orionis. They measured the [O I] 6300/([S II] 6716+[S II] 6731) ratio for over 30 targets, and the [N II] 6583/([S II] 6716+[S II] 6731) ratio for about 15 sources. Similarly to the earlier study, Maucó et al. (2025) observed that the [N II] 6583/([S II] 6716+[S II] 6731) ratio is higher for σ-Orionis targets than for stars in Taurus, while the [O I] 6300/([S II] 6716+[S II] 6731) ratio is similar to those in Taurus. Here, we compare the ratios measured from the MUSE observations (intensities integrated over the whole proplyd) with those presented in Maucó et al. (2025).

Figure 4.2 shows the ratios for aforementioned emission lines as a function of the UV field strength; for the latter, projected separations from the UV sources are used. According to Anania et al. (2025), 2D approximation can provide a reasonable estimate, although it could lead to an overestimation of the UV strength because it neglects the true, possibly larger, separation between stars and the dust extinction in the cluster. In the figure, we also include the trend of [N II]/[S II] vs FUV field predicted by an approximate model (Peake et al. 2025). The model

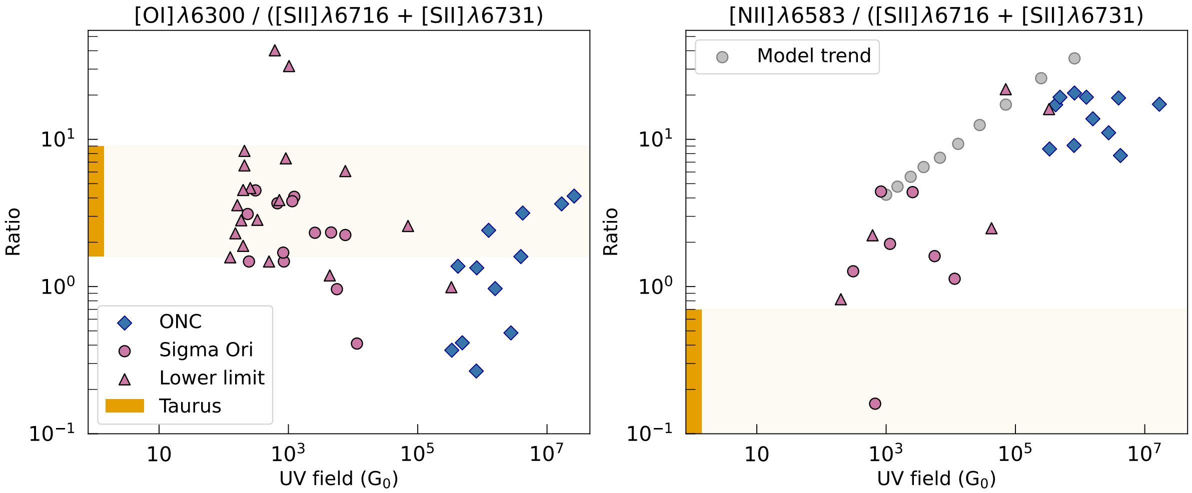

Figure 4.2: Emission line ratios for 12 ONC proplyds, and σ-Orionis sources as a function of the UV field they experience. Diamonds represent integrated intensity values for ONC proplyds; the UV sources are θ^1 Ori C, and θ^2 Ori A for proplyds 203-504 and 244-440. Dots mark σ-Orionis sources with the UV source being the σ-Orionis massive system. (Maucó et al. 2025). The colored area marks the typical range of ratio values for Taurus. Grey points on the right panel mark the trend predicted by an approximate model; note that the model considers emission from the cusp of the proplyd outwards (Peake et al. 2025).

considers emission from the cusp of the proplyd outwards, while the observational values of ONC include the whole proplyd. Even so, the observations and the model points are in general agreement with the ratio decreasing with decreasing FUV radiation.
The values reported for σ-Orionis, and the typical range of ratio values for Taurus (reported in Rigliaco et al. 2009) are also included. For the ONC proplyds, the [O I]/[S II] ratios are spread between 0–10, with five of these values overlapping with both those of σ-Orionis and Taurus. Therefore, internal photoevaporative winds can lead to similar [O I] λ6300 line fluxes as the external winds. On the other hand, the ratios are high (~8–22) for the ionized species [N II]/[S II], and the values clearly stand out in comparison to those of σ-Orionis (most of the values <5) and the range for Taurus targets (<1). Figure 4.2 therefore shows the impact of the UV field on these line ratios, targets of each region covering a distinct range of [N II]/[S II] ratio values and further demonstrating the advantage of this ratio as a tracer for external photoevaporation.

The ratios in the works of Rigliaco et al. (2009) and Maucó et al. (2025) rely on spatially unresolved measurements, encompassing values from over the entire emitting region. With the observations of MUSE, however, we can pinpoint the origin of the emission components, investigate how the ratios vary across the source, and therefore directly examine the regions where different physical processes dominate. In Figures 4.3 and 4.4, we show the maps of the same ratios. The [N II]/[S II] ratio is highest (~20–30) near the ionization front. This is expected as the [N II] emission arises mostly from the bright cusp, that is the highly ionized head of the proplyds in the direction of the UV source (individual images shown in Aru et al. 2024b). The values at the ionization front can be even higher, for example ∼40 for 177-341W and 173-236; the latter has a bright area in the west side of its cusp. The ratio becomes smaller in the tail (∼10), which is traced by [S ii] λ6731. The values of the ionization front and the tail cannot be distinguished in the subfigure for proplyd 168-326, which is a binary proplyd system (Henney 2002) with their emission blending together in the ratio map. Proplyd 203-504 has a bright edge on the Orion Bar-facing side. For 244-440, subregions with a lower ratio (∼6) appear inside its cocoon. A brighter subregion lies northeast from the center of the proplyd. Its ionization front stands out from the rest of the proplyd, with a value of roughly 13. The maps for targets 154-346 and 167-325 lack the same clarity as for the rest of the sample; these proplyds cover <1" in the FOV and are excluded from the description.

The ratio values are significantly lower for the [O i]/[S ii] ratios, with the brightest parts mostly corresponding to the disk and the cusp (values ∼1–2) and the tail ratio lowering to <1. As described in Sect. 4.1, the [O i] λ6300 line is known to trace the disk and the ionization front. The [O i]/[S ii] ratio allows us to see particularly interesting structures in the proplyd 244-440, with filament-like parts extending from south to southwest of the disk, and wider subregions surrounding the disk in the northern side. The disk itself appears brighter than the rest of the proplyd. The jet knots, identified in Kirwan et al. (2023), are also visible.

In summary, spatially unresolved ratios—particularly [N ii]/[S ii]—provide a valuable tracer. The spatially resolved data contain additional information, which we use to gain insights into the physical properties, as discussed in the next section.

4.3.2 Temperature and density diagnostics

Henney & O'Dell (1999) used high-resolution spectroscopic data of proplyds 170-337, 177-341W, 244-440 (the three overlapping with our sample) and 182-413, as well as theoretical models to measure proplyd properties. They used extinction-corrected Hα intensities, and converted them into emission measures assuming an Hα emission coefficient, to estimate peak densities in the cusps. Their values are in the range 0.0785–1.31$\times$ 10^6 cm^{-3}. Ballering et al. (2023) found $n_e = 0.7 - 3 \times 10^6$ cm^{-3} by using the brightness of the 3.1 mm free-free emission to compute the density of the outflow. Boyden et al. (2025) measured line fluxes of H41α emission and combined them with measurements of free-free flux. They derived T$_e$ in the range 3500–12,300 K and n$_e$ on the order of $10^6 - 10^7$ cm^{-3} in the ionization fronts of H41α-detected proplyds; proplyds 177-341W, 170-337, and 168-326 overlap with our sample. These densities, as discussed also by e.g., Henney (2002), Mesa-Delgado et al. (2012), and Tsamis et al. (2013) are higher than the critical densities of many forbidden lines typically used as density and temperature diagnostics in other astrophysical analyses, which limits the use of these diagnostics. Here, we discuss the possibilities available given our data.

Following Osterbrock (1989) and Vasconcelos et al. (2005b), the emission lines of [N ii] can be used to relate the ratio to the electron temperature, T_e, and density, n_e:

$$\frac{[\mathrm{N\,II}]\,\lambda\lambda(6548+6583)}{[\mathrm{N\,II}]\,\lambda5754} = \frac{6.91\exp\left(\frac{2.5\times10^4}{T_e}\right)}{1+(2.5\times10^{-3})\left(\frac{N_e}{T_e^{1/2}}\right)} \tag{4.2}$$

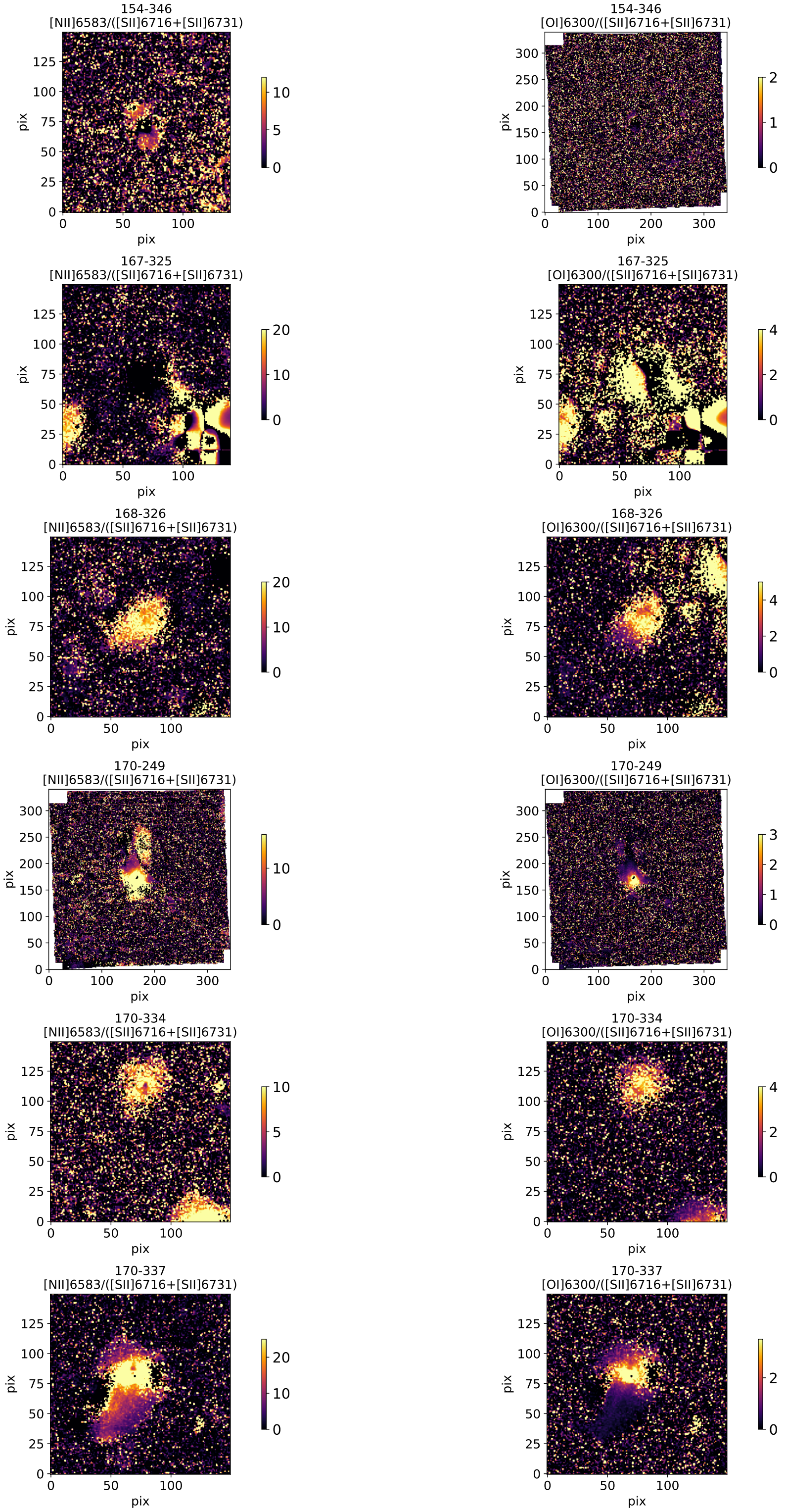

Figure 4.3: Ratio maps for 12 ONC proplyds. Figures for 154-346, 167-325, 168-326, 170-334, 170-337, 171-340, and 174-414 are zoomed in.

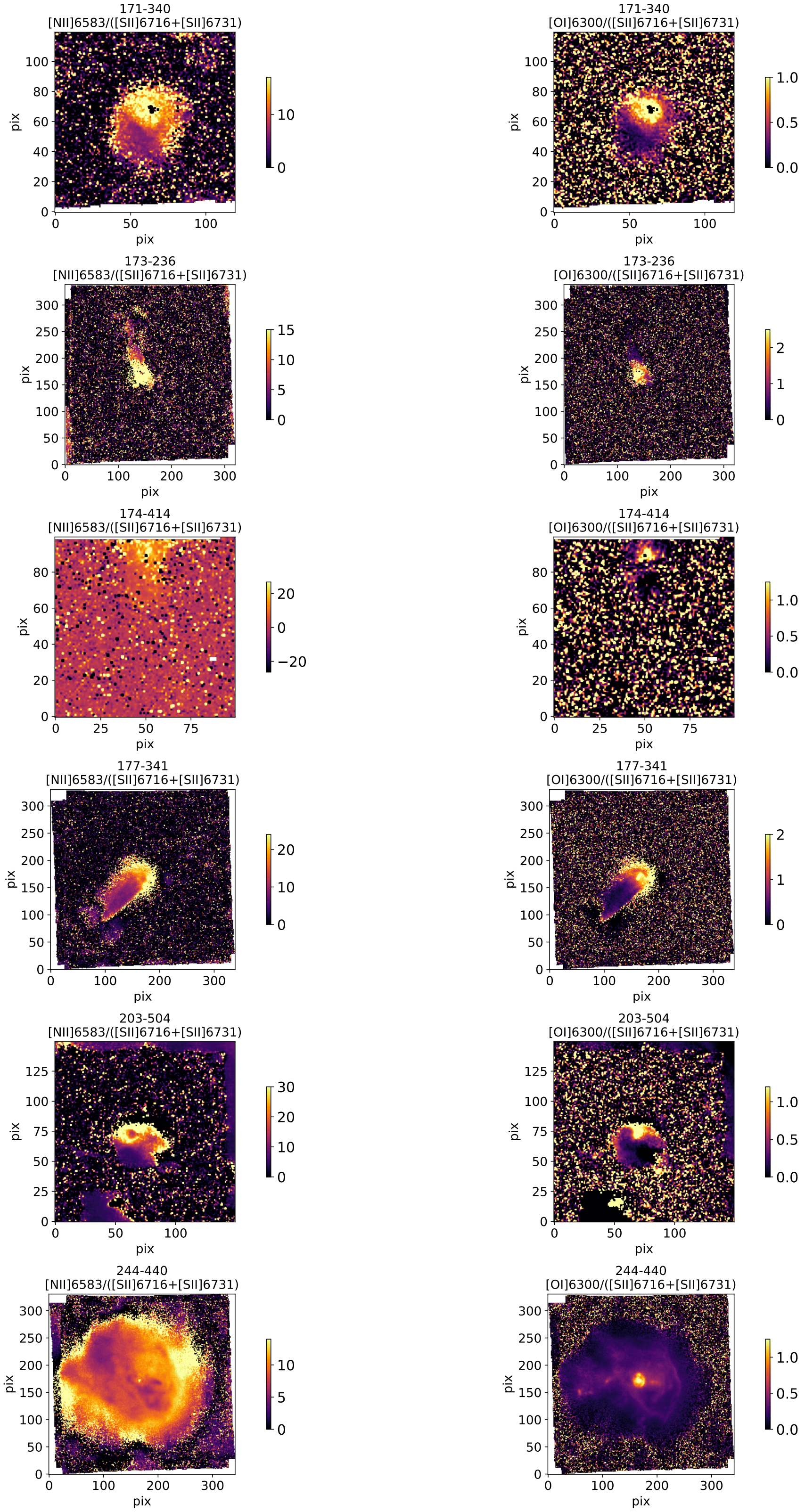
171-340
[NII]6583/([SII]6716+[SII]6731)
171-340
[OI]6300/([SII]6716+[SII]6731)
173-236
[NII]6583/([SII]6716+[SII]6731)
173-236
[OI]6300/([SII]6716+[SII]6731)
174-414
[NII]6583/([SII]6716+[SII]6731)
174-414
[OI]6300/([SII]6716+[SII]6731)
177-341
[NII]6583/([SII]6716+[SII]6731)
177-341
[OI]6300/([SII]6716+[SII]6731)
203-504
[NII]6583/([SII]6716+[SII]6731)
203-504
[OI]6300/([SII]6716+[SII]6731)
244-440
[NII]6583/([SII]6716+[SII]6731)
244-440
[OI]6300/([SII]6716+[SII]6731)
pix
pix
0
10
0.0
0.5
1.0
0
5
10
15
0
1
2
−20
0
20
0
10
20
0
10
20
30
0
5
10

Figure 4.4

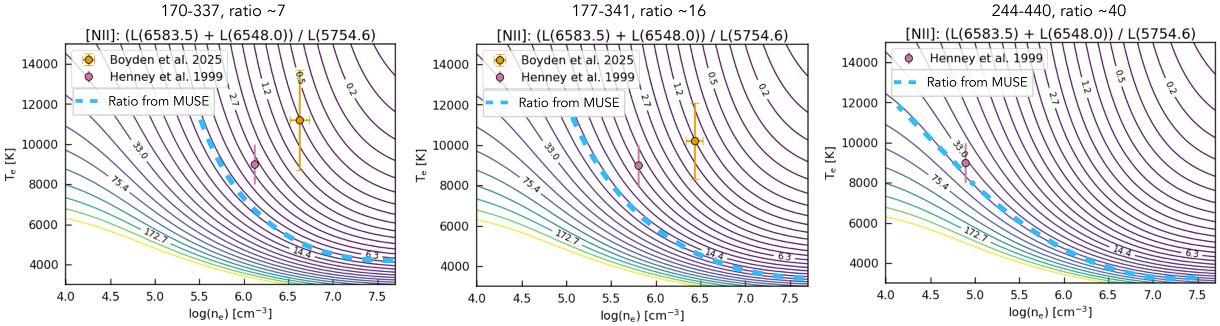

Figure 4.5: Measurements of electron temperature T_e and density n_e on a T_e-n_e grid generated in PyNeb for [N II] ($\lambda\lambda$6583.5,6548)/λ5754.6. The orange point marks n_e derived by Boyden et al. (2025); pink point marks the peak density from Henney & O'Dell (1999), and the blue curve marks the ratio value found with MUSE.

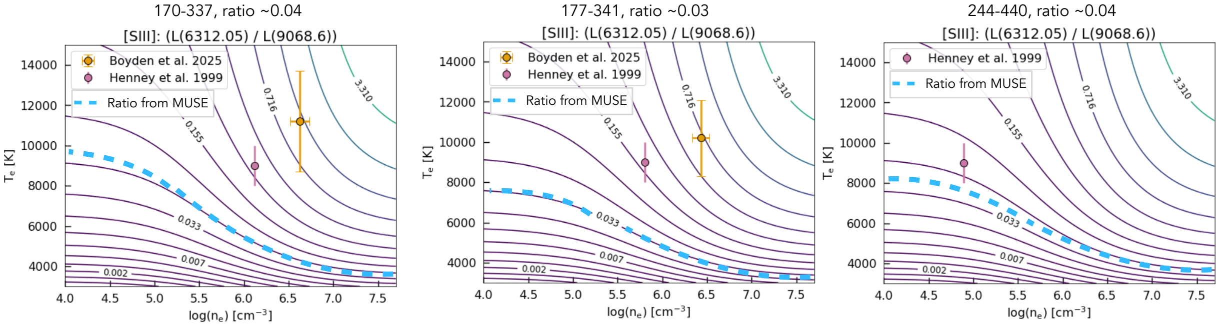

Figure 4.6: Same as Fig. 4.5 for [S III] λ6312/9069.

In Fig. 4.5, we show the T_e-n_e diagnostic plot for T_e in the range 4000–14,000 and n_e in the range 10^4–$10^{7.5}$ cm^{-3}, created with `PyNeb`. In this figure, we also include the T_e, n_e values for the proplyd 170-337, 177-341W, and 244-440 as listed by Boyden et al. (2025) and Henney & O'Dell (1999), and highlight the contour corresponding to the ratio measured from our data. For 170-337 and 177-341W, MUSE ratios corresponds to a lower n_e value than for the two other measurements (considering T ~8000 K and higher); n_e remains $>10^{5.5}$ cm^{-3} at ~10,000 K for 170-337, and n_e $>10^{5.1}$ cm^{-3} for 177-341W. In the case of 244-440, the largest proplyd in our sample, the ratio is in line with the peak density measured by Henney & O'Dell (1999), ranging from ~ $10^{4.6}$ cm^{-3} at ~10,000 K to ~ $10^{4.9}$ cm^{-3} at T~8000 K.

Figure 4.8 shows the typical [N II] ($\lambda\lambda$6548,6583)/λ5754 ratios for our sample. We report the ratios observed in the cusp of the proplyds in Table 4.2. We observe that the highest ratios are found for the largest proplyd 244-440. Higher ratio values correspond to lower densities (as seen in Fig. 4.5), and a lower density is indeed expected for larger proplyds.

Boyden et al. (2025) identified a negative correlation between electron density and projected separation. Although our sample is small, the low ratios for the proplyd closest to the UV source (168-326) and higher for the rest of the targets may hint at an empirical agreement with this trend.

Proplyd	Ratio
168-326	5
170-249	20
173-236	20-25
171-340	30
203-504	30-50
244-440	60-70

Table 4.2: Proplyds and [N ɪɪ] ($\lambda\lambda$6548,6583)/λ5754 ratios in the cusp.

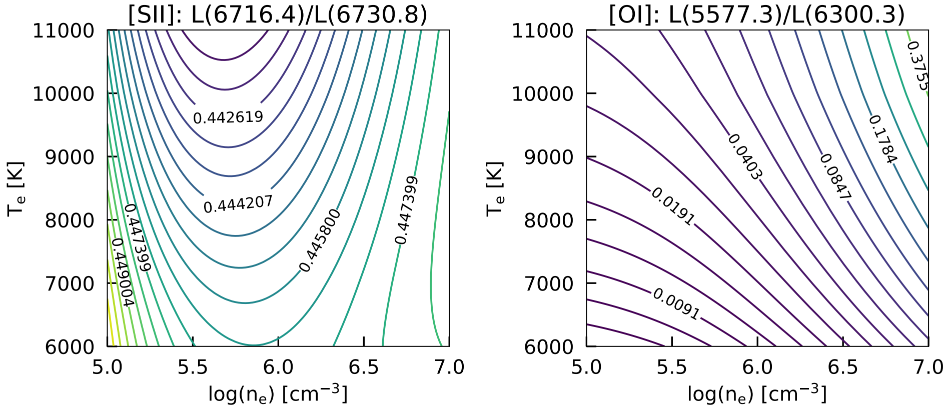

Figure 4.7: Electron temperature and density grids generated in PyNeb.

Another ratio we consider is [S ɪɪɪ] λ6312/λ9069. Similarly to Fig. 4.5, we plot the T_e-n_e range in Fig. 4.6. For 170-337 and 177-341, the ratio differs from the values that the literature T_e and n_e would produce. For 244-440, the MUSE ratio is more similar to the literature one, corresponding to electron density $\sim 10^{4.6}$ cm^{-3}, similarly to the value from Fig. 4.2.

We also look into the argon ratio proposed in literature, [Ar ɪɪɪ] (7135 + 7751)/ 5192 (Keenan et al. 1988). The 7135 Å and 7751 Å lines clearly trace the ionization front in our data. However, the 5192 Å line is too faint to inform us on whether or where it is emitted. This ratio is hence not applicable for our data.

Mesa-Delgado et al. (2012) used [Fe ɪɪɪ] lines to derive the density in proplyd 177-341. Later studies have shown that ionized iron emission is observed in the jet (as seen in Aru et al. (2024a) for 177-341W) and cannot be used to trace density in the cocoon. We therefore refrain from using this ratio for our purposes.

Finally, we look into the ratio [S ɪɪ] λ6716/λ6731. The observational ratios of [S ɪɪ] are ~0.4–0.5. The theoretical ratio is confined within ~0.4 for the expected physical properties (Fig. 4.7), and therefore in agreement with the measured ratio value. However, the contours have values too close to each other to derive n_e or T_e information.

Mesa-Delgado et al. (2012) combined the ratios of multiple species to create n_e-T_e diagnostic curves; given suitable ratios, the intersection of those curves can yield a solution for n_e-T_e.

They used the following ratios: [N II] λ6583/λ5755, [O III] λ5007/λ4363, [S II] ($\lambda\lambda$6717,6731) / ($\lambda\lambda$4068,4076) and [S II] λ6717/λ6731. Several of these lines are outside the range of MUSE, in the bluer part of the spectrum, and therefore not applicable here.

The ratio [O I]λ5577/λ6300 instructs us on the density at the base of the wind, as the [O I]5577 is emitted only on the disk surface, similarly to the [C I] line (Aru et al. 2024a). The observational ratios span from ~0.025–0.3, making the [O I] 6300 line up to ~30 times brighter. Comparing these values with the theoretical expectation for the ratio reported by Natta et al. (2014), the density at the base of the wind must be higher than $n_e \sim 10^6$ cm^{-3}. While this is a very conservative estimation, it does agree with with the density derived from a 1D model of the PDR by Champion et al. (2017).

4.4 Conclusions

We analyzed the MUSE data of ONC proplyds, which allows us to trace where different emission lines originate within the proplyd. Our focus was on the commonly observed forbidden-line ratios, which have previously shown promise to identify external photoevaporation. Our main findings are the following:

- The ratio [N II] λ6583/([S II]($\lambda\lambda$6716,6731) is a more robust tracer for external winds than [O I] λ6300/([S II]($\lambda\lambda$6716,6731). Plotting the ratios for the ONC proplyds as a function of the UV field strength, along with the ratios measured for the targets in σ Orionis (Maucó et al. 2025), shows that the ratios increase with higher UV radiation.

- The line ratio maps show that ratios vary significantly within the proplyds. The ratio is dependent on which species is bright in the cusp, and which species is associated with the tail, implying different physical conditions in these parts.

- The ratios can be used to estimate the order of electron densities, which are in agreement with the general ranges reported in literature. The ratios measured in the giant proplyd 244-440 suggest the lowest densities in the sample, ranging from $\sim 10^{4.6}$ cm^{-3} to $\sim 10^{4.9}$ cm^{-3} (depending on the ratio and the assumed temperature). For the other proplyds, we estimate the electron density on the order of 10^5 cm^{-3}.

In order to link the measured ratios and their spatial variation to physical processes, model predictions are needed—this will be carried out in a future paper. The available optical ratios for both temperature- and density-sensitive diagnostics remain limited. Therefore, future observations should provide access to a wider set of lines. Among the planned instrumentation, BlueMUSE is going to cover lines with higher n_{cr} which will be key to further constrain the physical properties of proplyds.

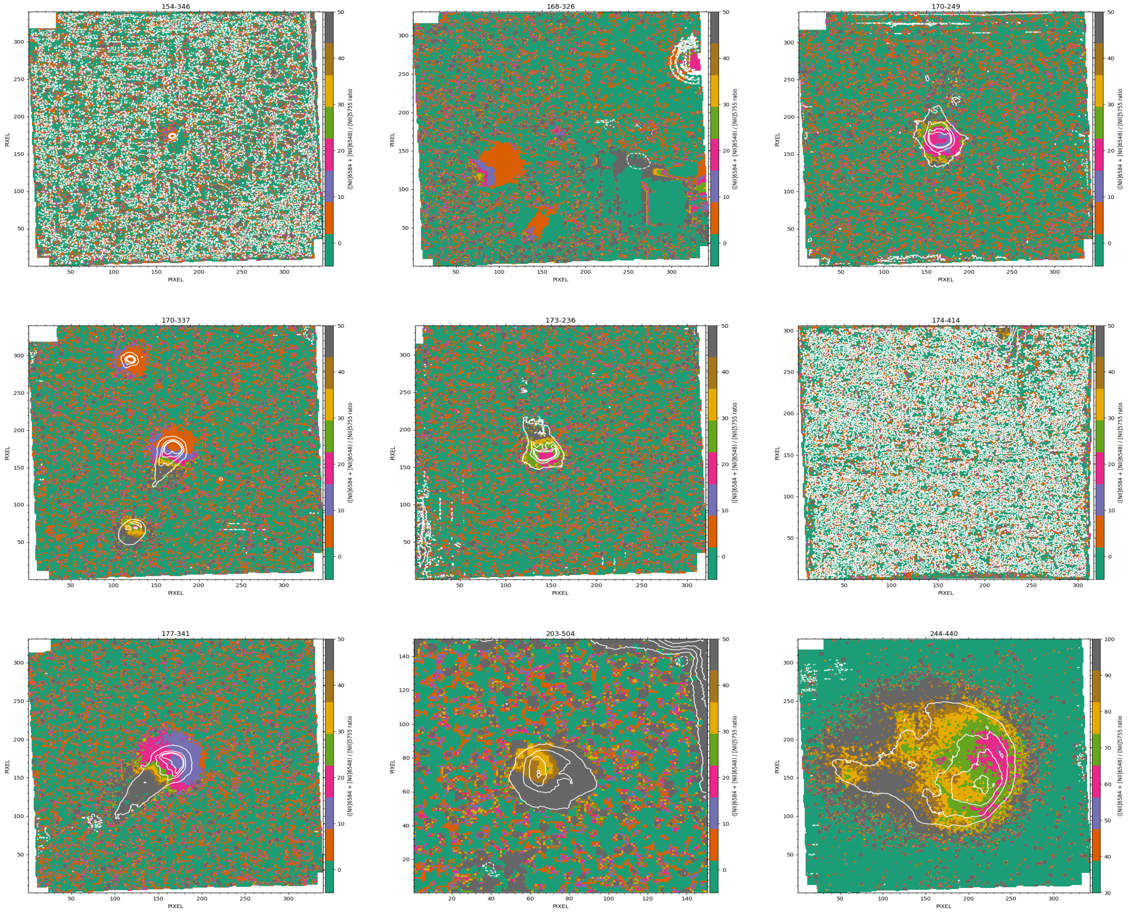

Figure 4.8: [N II] emission line ratios for 12 ONC proplyds.

Acknowledgements

MLA acknowledges funding from the European Union (ERC, WANDA, 101039452). Views and opinions expressed are however those of the author(s) only and do not necessarily reflect those of the European Union or the European Research Council Executive Agency. Neither the European Union nor the granting authority can be held responsible for them.

4.5 Appendix

4.5.1 Additional figures

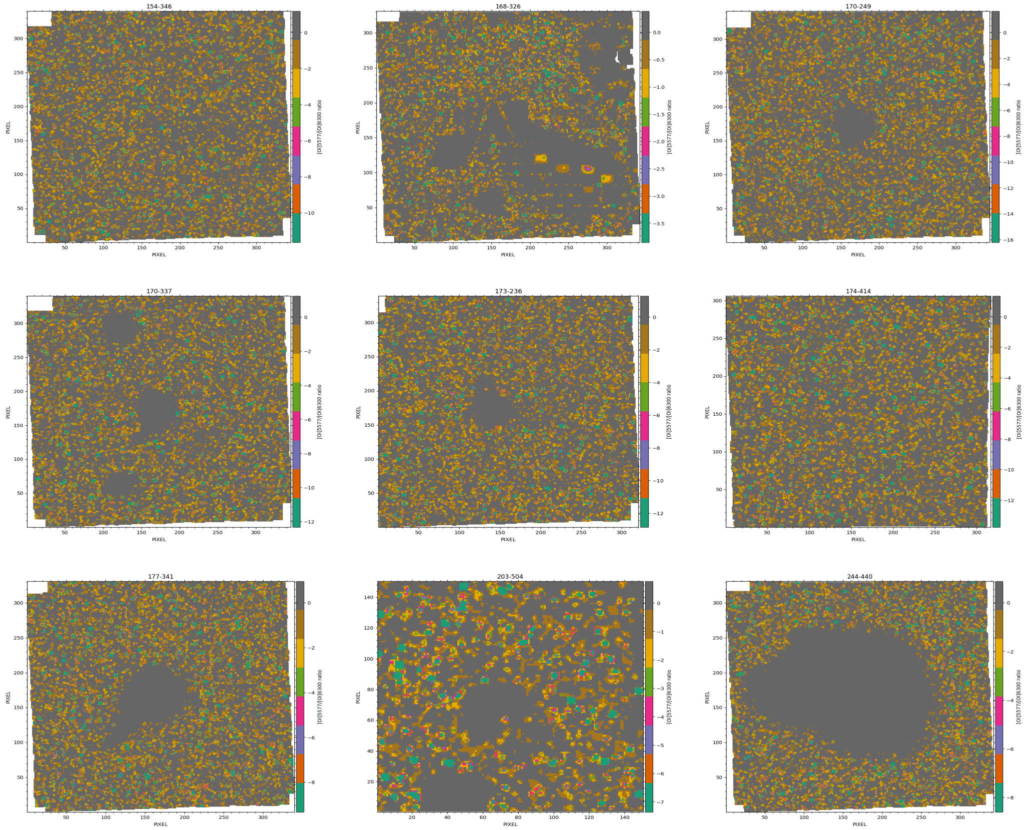

Figure 4.9: [O I] emission line ratios for 12 ONC proplyds.

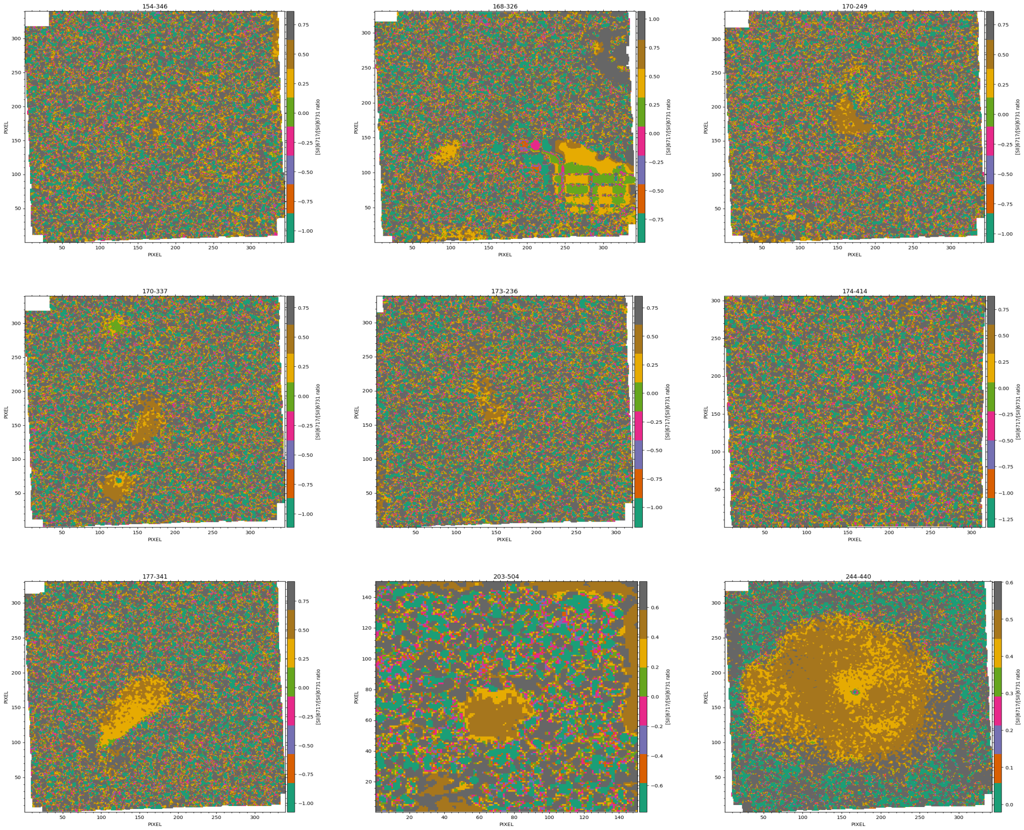

Figure 4.10: [S II] emission line ratios for 12 ONC proplyds.

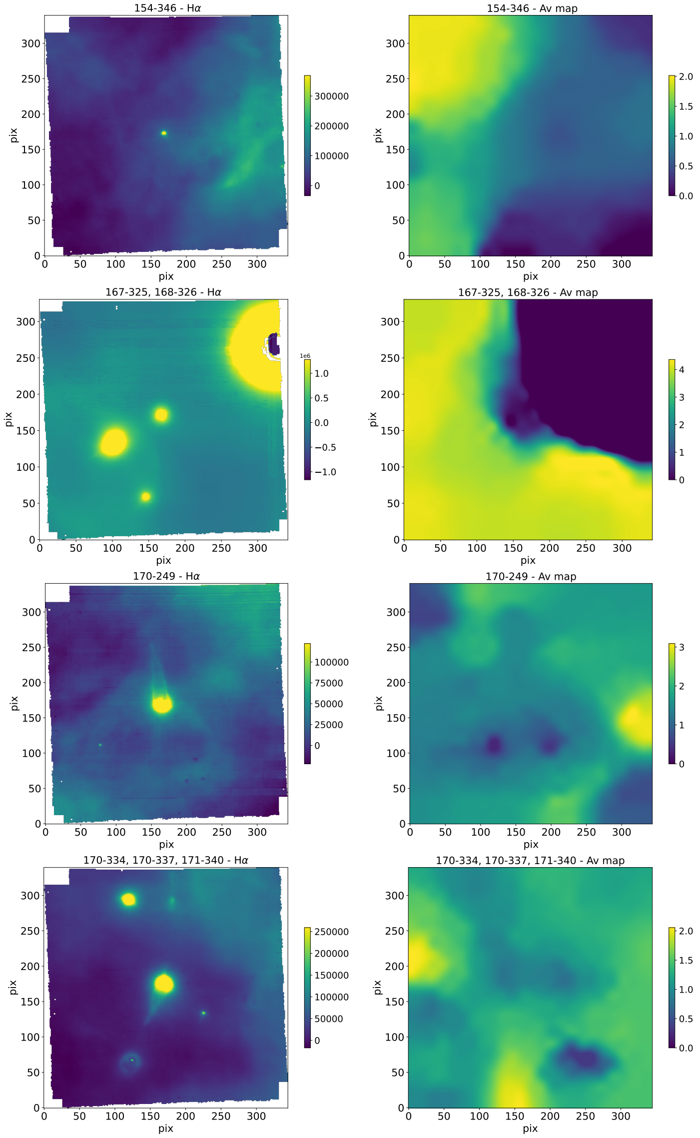

Figure 4.11: Left: Raw moment0 maps of the sample. Right: Extinction maps, which exclude the proplyds and other sources in each field of view.

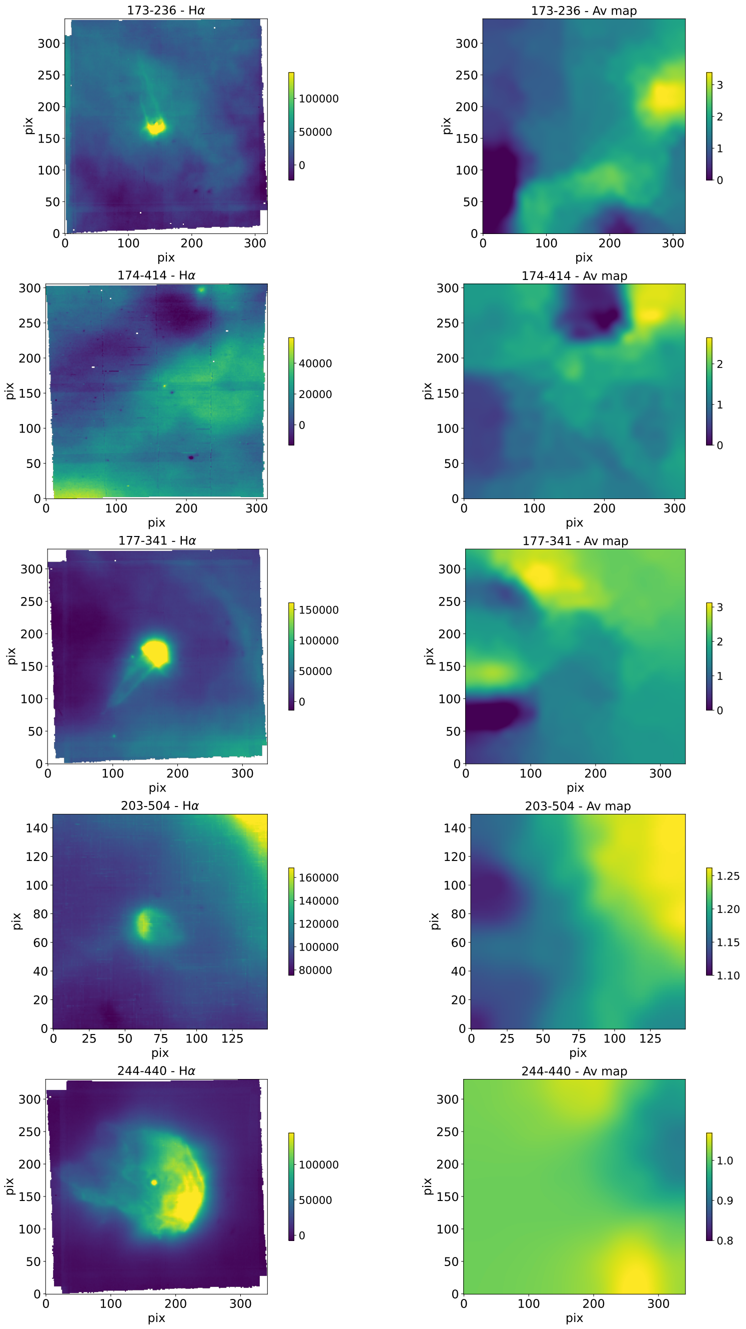

Figure 4.12: Same as Fig. 4.11 for the rest of the sample.

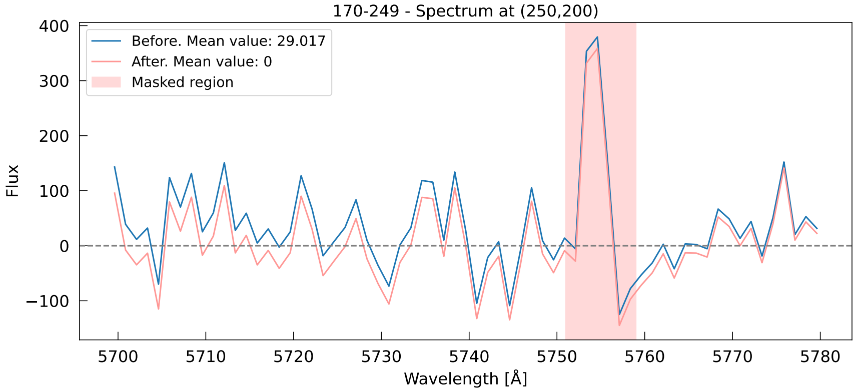

Figure 4.13: Example of the continuum subtraction.

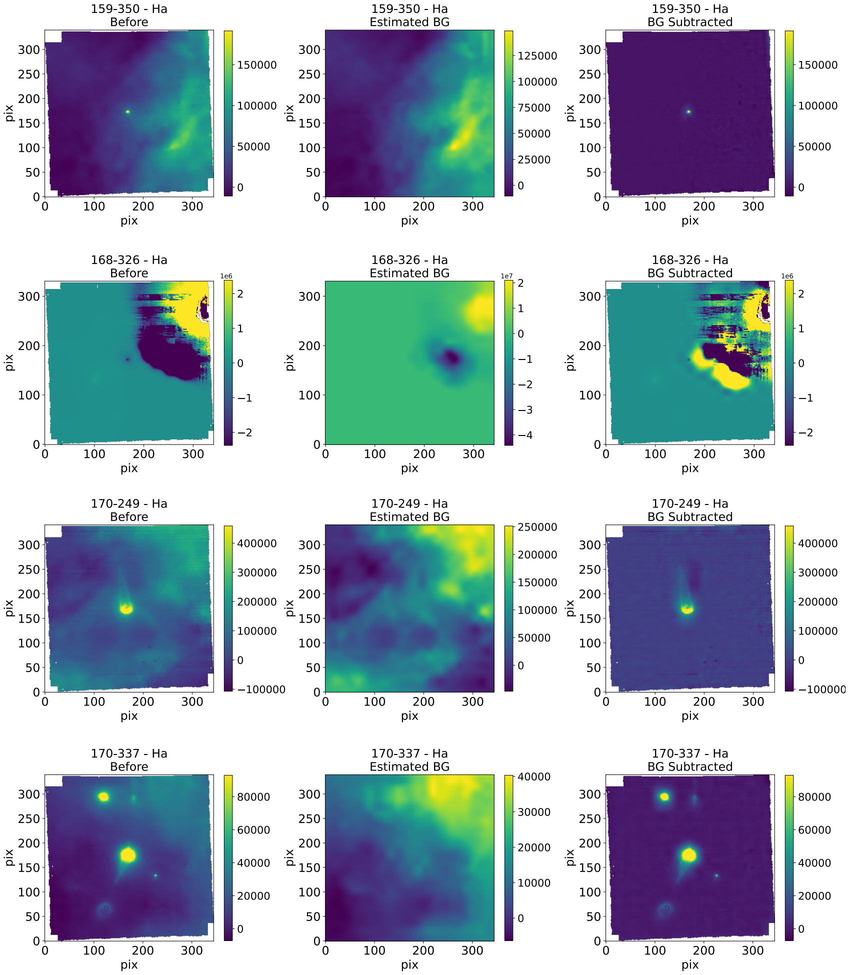

Figure 4.14: Outcome of background subtraction. Left: extinction-corrected Hα moment0 map, middle: estimated 2D background, right: background-subtracted moment0 map.

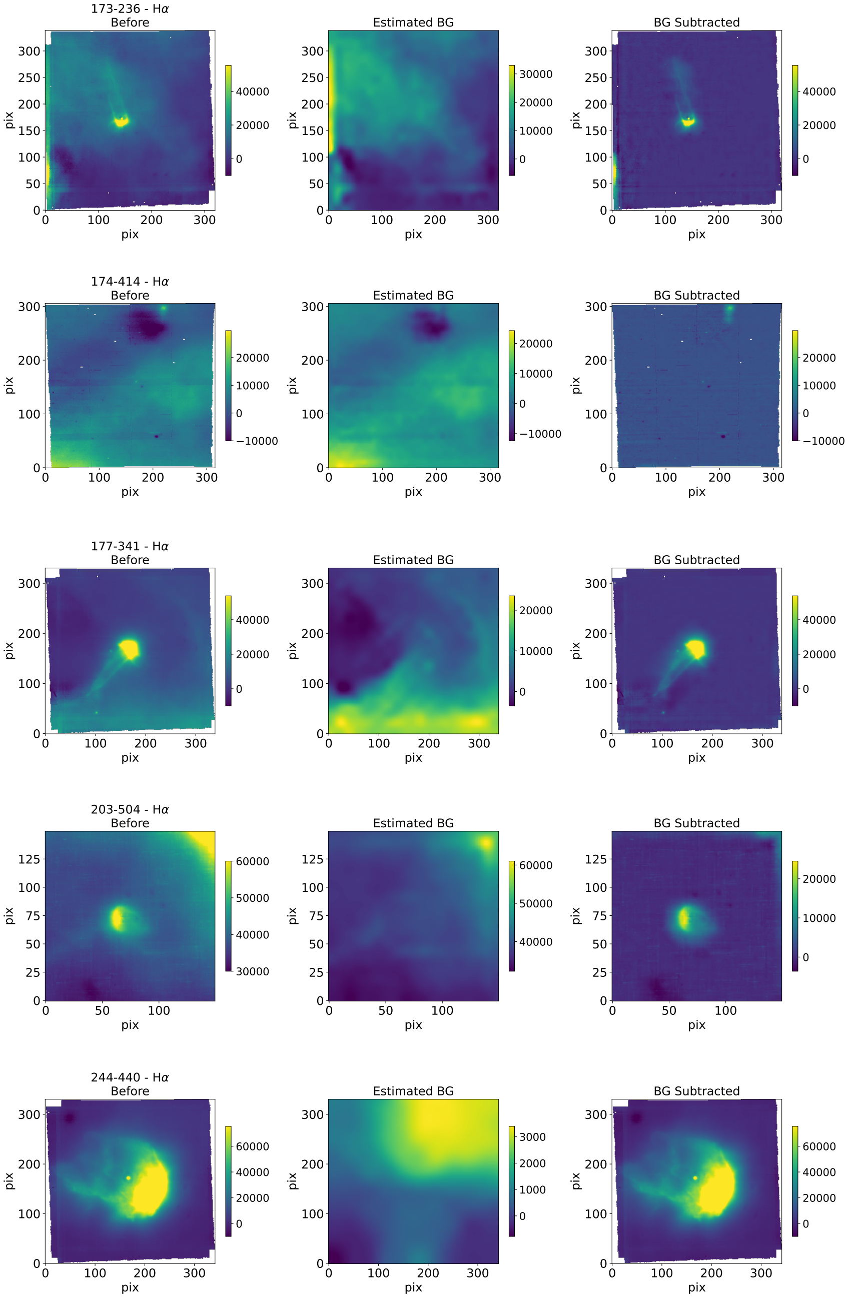

Figure 4.15: Same as Fig. 4.14 for the rest of the sample.

5

Conclusion

5.1 Summary and conclusions

In this thesis, I presented the study of ONC proplyds by using a kaleidoscopic view onto these objects made possible by integral field spectrography. This technique constructs spatially and spectrally resolved data-cubes, in which each pixel of the 2D view comprises a spectrum across the instrument's wavelength range. The data analyzed and studied here was provided by the Multi Unit Spectrographic Explorer MUSE observations (PI: Manara) of a dozen proplyds. MUSE, installed on the ESO Very Large Telescope in Chile, covers the optical wavelength range from about 4800 Å to 9300 Å with a field of view of 7.5×7.5 arcminutes. The data-cubes give the means to spatially distinguish different parts of the proplyds, and determine where emission lines of various degrees of ionization arise from: the ionization front, the cusp, the disk, or the comet-like tail.

The motivation for this thesis was to disentangle internal and external photoevaporation. As the prerequisite of using the data for measurements, I produced sub-cubes containing the emission lines of interest, and applied continuum-subtraction. In the first part of the analysis, the continuum-subtracted, single-line-integrated moment-zero maps were used to measure the ionization-front radii of the targets for four tracers, from neutral to doubly ionized species. Based on these measurements, the mass-loss rates in the range $\sim 1.1-94.5\times10^{-7}M_{\odot}\mathrm{yr}^{-1}$ were derived. This was a necessary step for a comparison with results from other observational techniques; the measurements were indeed in agreement.

The second part of this work focused on the forbidden line of neutral atomic carbon, [C I] 8727 Å. For the first time, the spatial location of the emission in the [O I] 5577 Å, [O I] 6300 Å, and [C I] 8727 Å lines (traced by VLT/MUSE-NFM) was compared with the ALMA Band 7 continuum disk emission. The result of this study was twofold. Firstly, the spatial location of the [C I] 8727 Å line emission was shown to be co-spatial with the disk emission. The [O I] 5577 Å and [O I] 6300 Å lines also coincide with the disk region, but the latter is blended with the emission from the ionization front. In some of the cases, the [C I] line traced the disk shape most clearly. Secondly, the study presented the lack of the carbon line's detection in isolated disks in low-mass star-forming regions, as opposed to the commonly detected [O I] lines. These findings strongly suggest that the [C I] 8727 Å line is a tell-tale tracer of externally driven photoevaporative winds, which agrees with recent excitation models.

The third part of the thesis continues with the exploration of tracers for external photoevaporation, but for the case of commonly observed forbidden-line ratios. I set out by further processing the sub-cubes, correcting line intensities for extinction. I then applied a novel background-

subtraction method (adapting it for the given dataset) to the continuum-subtracted, extinction-corrected moment-zero maps.
The emission lines of [O I] 6300 Å, [N II] 6583 Å, and [S II] 6731,6716 Å are detected in both isolated and irradiated disks, and were therefore principal for comparability. By comparing the [O I]/[S II] and [N II]/[S II] ratios with the values measured in other star-forming regions, the [N II]/[S II] ratio stood out with its high values in the ONC and further confirmed its use as a more reliable tracer of external winds (as previously suggested in two studies based in the Sigma Orionis cluster). The observed values were found to increase with higher incident UV field strengths, further demonstrating the UV environment's impact on disks.
Additionally, the trend above was shown to be in agreement with theoretical predictions, which were presented in a separate study, "Line ratio identification of external photoevaporation". In the aforementioned work, the CLOUDY photoionization code was used to approximately model the emission lines emitted from the hot ionized wind of a proplyd. I was involved as a co-author, providing the data of proplyd 177-341W, which the model was benchmarked against.
In the literature, the measurements of line ratios are based on spatially unresolved observations of slit spectroscopy. The ratios above were based on integrated over the whole proplyd to reproduce similar measurements for comparison. By using line ratio maps, MUSE allows to further determine how the ratios vary in different parts of the proplyds. For example, the [N II]/[S II] ratio is highest near the ionization front and much smaller in the tail: this reconnects to the proplyd morphology presented in Chapter 2 of this thesis (the [S II] $\lambda\,6731$ line is bright in the tail of the proplyd). Finally, the ratios were used to derive rough estimates for the electron densities. The available optical ratios for diagnostics remain limited, and future BlueMUSE observations would provide access to a wider set of diagnostic emission lines.

To conclude, the goal of this thesis was met with the identification of tracers for external irradiation. At the same time, the MUSE dataset comprises many more line ratio combinations that can be explored in the future.
The observations have motivated new proposals and projects already under way, including (1) a study of the giant proplyd 244-440 in K-band as observed with VLT/ERIS; (2) a spectral analysis of the [C I] 8727 Å line of proplyds with the VLT/UVES spectrograph; (3) exploration of a more distant region and applying the presented background subtraction method to the data; (4) continuation of the observation benchmark in proplyd emission models.

Bibliography

Abel, N., Ferland, G., & O'Dell, C. 2019, ApJ, 881, 130

Adams, F. C. 2010, Annual Review of A & A, 48, 47

Adams, F. C., Hollenbach, D., Laughlin, G., & Gorti, U. 2004, ApJ, 611, 360

Alcalá, J. M., Manara, C. F., Natta, A., et al. 2017, A&A, 600, A20

Alexander, R., Pascucci, I., Andrews, S., Armitage, P., & Cieza, L. 2014, in Protostars and Planets VI, ed. H. Beuther, R. S. Klessen, C. P. Dullemond, & T. Henning, 475–496

Alexander, R. D. & Pascucci, I. 2012, MNRAS: Letters, 422, L82

ALMA Partnership, Brogan, C. L., Pérez, L. M., et al. 2015, ApJ, 808, L3

Anania, R., Winter, A. J., Rosotti, G., et al. 2025, A&A, 695, A74

André, P. 2002, in EAS Publications Series, Vol. 3, EAS Publications Series, ed. J. Bouvier & J.-P. Zahn, 1–38

Andrews, S. M., Huang, J., Pérez, L. M., et al. 2018, ApJ, 869, L41

Ansdell, M., Williams, J. P., Manara, C. F., et al. 2017, The Astronomical Journal, 153, 240

Aru, M. L., Maucó, K., Manara, C. F., et al. 2024a, A&A, 692, A137

Aru, M. L., Maucó, K., Manara, C. F., et al. 2024b, A&A, 687, A93

Bacon, R., Accardo, M., Adjali, L., et al. 2010, in Society of Photo-Optical Instrumentation Engineers (SPIE) Conference Series, Vol. 7735, Ground-based and Airborne Instrumentation for Astronomy III, ed. I. S. McLean, S. K. Ramsay, & H. Takami, 773508

Bae, J., Isella, A., Zhu, Z., et al. 2023, in ASP Conference Series, Vol. 534, Protostars and Planets VII, ed. S. Inutsuka, Y. Aikawa, T. Muto, K. Tomida, & M. Tamura, 423

Bai, X.-N. & Stone, J. M. 2013, ApJ, 769, 76

Bajaj, N. S., Pascucci, I., Gorti, U., et al. 2024, The Astronomical Journal, 167, 127

Balega, Y. Y., Chentsov, E., Rzaev, A. K., & Weigelt, G. 2015, Physics and Evolution of Magnetic and Related Stars, 494, 57

Ballabio, G., Haworth, T. J., & Henney, W. J. 2023, MNRAS, 518, 5563

Ballering, N. P., Cleeves, L. I., Haworth, T. J., et al. 2023, ApJ, 954, 127

Bally, J. 2008, Overview of the Orion Complex

Bally, J., O'Dell, C. R., & McCaughrean, M. J. 2000, The Astronomical Journal, 119, 2919

Bally, J. & Reipurth, B. 2001, ApJ, 546, 299

Bally, J., Sutherland, R. S., Devine, D., & Johnstone, D. 1998, The Astronomical Journal, 116, 293

Bally, J., Youngblood, A., & Ginsburg, A. 2012, ApJ, 756, 137

Banzatti, A., Pascucci, I., Edwards, S., et al. 2019, ApJ, 870, 76

Beccari, G., Petr-Gotzens, M. G., Boffin, H. M. J., et al. 2017, A&A, 604, A22

Berné, O., Habart, É., Peeters, E., et al. 2022, Publications of the ASP, 134, 054301

Berné, O., Habart, E., Peeters, E., et al. 2024, Science, 383, 988

Berné, O., Martin-Drumel, M.-A., Schroetter, I., et al. 2023, , 621, 56

Bernstein, G. M., Trilling, D. E., Allen, R. L., et al. 2004, The Astronomical Journal, 128, 1364

Birnstiel, T. 2024, Annual Review of A & A, 62, 157

Blagrave, K. P., Martin, P., Rubin, R., et al. 2007, ApJ, 655, 299

Blandford, R. D. & Payne, D. G. 1982, MNRAS, 199, 883

Boyden, R. D. & Eisner, J. A. 2020, ApJ, 894, 74

Boyden, R. D., Emig, K. L., Ballering, N. P., et al. 2025, ApJ, 983, 81

Brasser, R., Duncan, M. J., & Levison, H. F. 2006, , 184, 59

Brown, M. E., Trujillo, C., & Rabinowitz, D. 2004, ApJ, 617, 645

Bruderer, S., van Dishoeck, E. F., Doty, S. D., & Herczeg, G. J. 2012, A&A, 541, A91

Calvet, N., D'Alessio, P., Hartmann, L., et al. 2002, ApJ, 568, 1008

Cardelli, J. A., Clayton, G. C., & Mathis, J. S. 1989, ApJ, 345, 245

Carpenter, J. M., Mamajek, E. E., Hillenbrand, L. A., & Meyer, M. R. 2006, ApJ, 651, L49

Chakraborty, S., Muskatel, B. H., Jackson, T. L., et al. 2014, Proceedings of the National Academy of Sciences, 111, 14704

Champion, J., Berné, O., Vicente, S., et al. 2017, A&A, 604, A69

Chown, R., Sidhu, A., Peeters, E., et al. 2024, A & A, 685, A75

Churchwell, E., Wood, D. O. S., Felli, M., & Massi, M. 1987, ApJ, 321, 516

Clarke, C. J., Gendrin, A., & Sotomayor, M. 2001, MNRAS, 328, 485

Connelly, J. N., Bizzarro, M., Krot, A. N., et al. 2012, Science, 338, 651

Cordiner, M. A., Darnell, K., Bockelée-Morvan, D., et al. 2024, The Planetary Science Journal, 5, 221

Cosmovici, C. B., Strafella, F., & Iijima, T. 1981, A&A, 101, 397

Courtes, G. 1982, 123–128

Da Rio, N., Gouliermis, D. A., & Gennaro, M. 2010, ApJ, 723, 166

Da Rio, N., Robberto, M., Soderblom, D. R., et al. 2010, ApJ, 722, 1092

Dahm, S. E. & Hillenbrand, L. A. 2007, The Astronomical Journal, 133, 2072

Dearborn, D. S. P. & Blake, J. B. 1988, ApJ, 332, 305

Dobbs, C. L., Krumholz, M. R., Ballesteros-Paredes, J., et al. 2014, Formation of Molecular Clouds and Global Conditions for Star Formation (University of Arizona Press)

Draine, B. T. 2011, Physics of the Interstellar and Intergalactic Medium

Dwarkadas, V. V., Dauphas, N., Meyer, B., Boyajian, P., & Bojazi, M. 2017, ApJ, 851, 147

Eisner, J. A., Arce, H. G., Ballering, N. P., et al. 2018, ApJ, 860, 77

Eisner, J. A., Arce, H. G., Ballering, N. P., et al. 2018, ApJ, 860, 77

Eisner, J. A., Bally, J. M., Ginsburg, A., & Sheehan, P. D. 2016, ApJ, 826, 16

Elmegreen, B. G. & Falgarone, E. 1996, ApJ, 471, 816

Elmegreen, B. G. & Lada, C. J. 1977, ApJ, 214, 725

Ercolano, B. & Owen, J. E. 2010, MNRAS, no

Ercolano, B. & Pascucci, I. 2017, Royal Society Open Science, 4, 170114

Ercolano, B. & Pascucci, I. 2017, Royal Society Open Science, 4, 170114

Escalante, V., Sternberg, A., & Dalgarno, A. 1991, ApJ, 375, 630

Evans, N. J., Dunham, M. M., Jørgensen, J. K., et al. 2009, ApJ Supplement Series, 181, 321

Facchini, S., Clarke, C. J., & Bisbas, T. G. 2016, MNRAS, 457, 3593

Fang, M., Kim, J. S., Pascucci, I., & Apai, D. 2021, ApJ, 908, 49

Fang, M., Pascucci, I., Edwards, S., et al. 2018, ApJ, 868, 28

Fang, M., van Boekel, R., King, R. R., et al. 2012, A&A, 539, A119

Ferland, G. J., Henney, W. J., O'Dell, C. R., et al. 2012, ApJ, 757, 79

Forbrich, J., Rivilla, V. M., Menten, K. M., et al. 2016, ApJ, 822, 93

Frediani, J., Bik, A., Ramírez-Tannus, M. C., et al. 2025, arXiv e-prints, arXiv:2507.13921

Freudling, W., Romaniello, M., Bramich, D. M., et al. 2013, A&A, 559, A96

Füri, E. & Marty, B. 2015, Nature Geoscience, 8, 515

Gangi, M., Nisini, B., Manara, C. F., et al. 2023, A&A, 675, A153

Goicoechea, J. R., Le Bourlot, J., Black, J. H., et al. 2024, A&A, 689, L4

Goicoechea, J. R., Pety, J., Cuadrado, S., et al. 2025, A & A, 696, A100

Gorti, U. & Hollenbach, D. 2002, ApJ, 573, 215

Gorti, U. & Hollenbach, D. 2009, ApJ, 690, 1539

Gounelle, M. & Meynet, G. 2012, A&A, 545, A4

Greene, T. P., Wilking, B. A., Andre, P., Young, E. T., & Lada, C. J. 1994, ApJ, 434, 614

Guarcello, M. G., Drake, J. J., Wright, N. J., et al. 2023, ApJ Supplement Series, 269, 13

Guillot, T. & Hueso, R. 2006, MNRAS: Letters, 367, L47

Habart, E., Peeters, E., Berné, O., et al. 2024, A&A, 685, A73

Habart, E., Peeters, E., Berné, O., et al. 2023, arXiv e-prints, arXiv:2308.16732

Habart, Emilie, Le Gal, Romane, Alvarez, Carlos, et al. 2023, AA, 673, A149

Habing, H. J. 1968, Bulletin of the Astronomical Institutes of the Netherlands, 19, 421

Haisch, Jr., K. E., Lada, E. A., & Lada, C. J. 2001, ApJ, 553, L153

Haro, G. 1953, ApJ, 117, 73

Harries, T., Haworth, T., Acreman, D., Ali, A., & Douglas, T. 2019, Astronomy and Computing, 27, 63

Hartigan, P., Edwards, S., & Ghandour, L. 1995, ApJ, 452, 736

Hartmann, L., Calvet, N., Gullbring, E., & D'Alessio, P. 1998, ApJ, 495, 385

Hartmann, L., Herczeg, G., & Calvet, N. 2016, Annual Review of A & A, 54, 135

Haworth, T. J. 2021, MNRAS, 503, 4172

Haworth, T. J., Boubert, D., Facchini, S., Bisbas, T. G., & Clarke, C. J. 2016, MNRAS, 463, 3616

Haworth, T. J. & Clarke, C. J. 2019, MNRAS, 485, 3895

Haworth, T. J., Clarke, C. J., Rahman, W., Winter, A. J., & Facchini, S. 2018, MNRAS, 481, 452

Haworth, T. J., Coleman, G. A. L., Qiao, L., Sellek, A. D., & Askari, K. 2023a, MNRAS, 526, 4315

Haworth, T. J. & Harries, T. J. 2012, MNRAS, 420, 562

Haworth, T. J., Kim, J. S., Qiao, L., et al. 2022, MNRAS, 512, 2594

Haworth, T. J., Kim, J. S., Winter, A. J., et al. 2021, MNRAS, 501, 3502

Haworth, T. J., Reiter, M., O'Dell, C. R., et al. 2023b, MNRAS, 525, 4129

Hendler, N., Pascucci, I., Pinilla, P., et al. 2020, ApJ, 895, 126

Henney, W. J. 2002, , 38, 71

Henney, W. J. & Arthur, S. J. 1998, The Astronomical Journal, 116, 322

Henney, W. J., Meaburn, J., Raga, A. C., & Massey, R. 1997, Optical emission line profiles of the LV knots (proplyds) in Orion, Tech. rep.

Henney, W. J. & O'Dell, C. R. 1999, The Astronomical Journal, 118, 2350

Henney, W. J., O'Dell, C. R., Meaburn, J., Garrington, S. T., & Lopez, J. A. 2002, ApJ, 566, 315

Herczeg, G. J. & Hillenbrand, L. A. 2014, ApJ, 786, 97

Hernandez, J., Calvet, N., Briceno, C., et al. 2007, ApJ, 671, 1784

Hillenbrand, L. A. 1997, The Astronomical Journal, 113, 1733

Hillenbrand, L. A. & Carpenter, J. M. 2000, ApJ, 540, 236

Hillenbrand, L. A. & Hartmann, L. W. 1998, ApJ, 492, 540

Hippelein, H. & Muench, G. 1978, A&A, 68, L7

Hogerheijde, M. R., Jansen, D. J., & van Dishoeck, E. F. 1995, A & A (ISSN 0004-6361), vol. 294, no. 3, p. 792-810, 294, 792

Hollenbach, D., Johnstone, D., Lizano, S., & Shu, F. 1994, ApJ, 428, 654

Itrich, D., Testi, L., Beccari, G., et al. 2024, A&A, 685, A100

Jacobsen, S. B., Chakrabarti, R., Ranen, M. C., & Petaev, M. I. 2008, in 39th Annual Lunar and Planetary Science Conference, Lunar and Planetary Science Conference, 1999

Jeffries, R. D., Littlefair, S. P., Naylor, T., & Mayne, N. J. 2011, MNRAS, 418, 1948

Jerabkova, T., Beccari, G., Boffin, H. M. J., et al. 2019, A & A, 627, A57

Johnstone, D., Hollenbach, D., & Bally, J. 1998, ApJ, 499, 758

Keenan, F. P., Johnson, C. T., & Kingston, A. E. 1988, A&A, 202, 253

Kim, J. S., Clarke, C. J., Fang, M., & Facchini, S. 2016, ApJ Letters, 826, L15

Kirwan, A., Manara, C. F., Whelan, E. T., et al. 2023, A&A, 673, A166

Kounkel, M., Hartmann, L., Loinard, L., et al. 2017, ApJ, 834, 142

Kroupa, P. 2000, New Astronomy, 4, 615

Krumholz, M. R., McKee, C. F., & Bland-Hawthorn, J. 2019, Annual Review of A & A, 57, 227

Kuffmeier, M., Jensen, S. S., & Haugbølle, T. 2023, The European Physical Journal Plus, 138, 272

Kuhn, M. A., Hillenbrand, L. A., Sills, A., Feigelson, E. D., & Getman, K. V. 2019, ApJ, 870, 32

Lada, C. J. 1987, Symposium - International Astronomical Union, 115, 1

Laques, P. & Vidal, J. L. 1979, A & A, 73, 97

Law, C. J., Alarcón, F., Cleeves, L. I., Öberg, K. I., & Paneque-Carreño, T. 2023, ApJ, 959, L27

Lesur, G., Flock, M., Ercolano, B., et al. 2023, in ASP Conference Series, Vol. 534, Protostars and Planets VII, ed. S. Inutsuka, Y. Aikawa, T. Muto, K. Tomida, & M. Tamura, 465

Lesur, G. R. J. 2021, Journal of Plasma Physics, 87, 205870101

Liffman, K. 2003, Publications of the Astronomical Society of Australia, 20, 337

Luhman, K. L. 2018, The Astronomical Journal, 156, 271

Luridiana, V., Morisset, C., & Shaw, R. A. 2015, A&A, 573, A42

Luu, J. X. & Jewitt, D. C. 2002, Annual Review of A & A, 40, 63

Lyons, J. R. & Young, E. D. 2005, Nature, 435, 317

MacPherson, G. J., Davis, A. M., & Zinner, E. K. 1995, Meteoritics, 30, 365

Mamajek, E. E., Usuda, T., Tamura, M., & Ishii, M. 2009, in AIP Conference Proceedings (AIP), 3–10

Manara, C. F., Ansdell, M., Rosotti, G. P., et al. 2023, in Protostars and Planets VII, Vol. 534, 539

Manara, C. F., Ansdell, M., Rosotti, G. P., et al. 2023, in ASP Conference Series, Vol. 534, Protostars and Planets VII, ed. S. Inutsuka, Y. Aikawa, T. Muto, K. Tomida, & M. Tamura, 539

Manara, C. F., Frasca, A., Alcalá, J. M., et al. 2017a, A&A, 605, A86

Manara, C. F., Frasca, A., Venuti, L., et al. 2021, A&A, 650, A196

Manara, C. F., Robberto, M., Da Rio, N., et al. 2012, ApJ, 755, 154

Manara, C. F., Testi, L., Herczeg, G. J., et al. 2017b, A & A, 604, A127

Manara, C. F., Testi, L., Rigliaco, E., et al. 2013, A&A, 551, A107

Mann, R. K., Andrews, S. M., Eisner, J. A., et al. 2015, ApJ, 802, 77

Mann, R. K., Di Francesco, J., Johnstone, D., et al. 2014, ApJ, 784, 82

Mann, R. K. & Williams, J. P. 2010, ApJ, 725, 430

Massey, R. M. & Meaburn, J. 1995, MNRAS, 273, 615

Matzner, C. D. 2002, ApJ, 566, 302

Maucó, K., Manara, C. F., Ansdell, M., et al. 2023, A&A, 680, C1

Maucó, K., Manara, C. F., Bayo, A., et al. 2025, A&A, 693, A87

Mayor, M. & Queloz, D. 1995, Nature, 378, 355

McCaughrean, M. & Pearson, S. 2023, arXiv preprint arXiv:2310.03552

McCaughrean, M. J. & O'Dell, C. R. 1996, The Astronomical Journal, 111, 1977

McCaughrean, M. J. & Stauffer, J. R. 1994, The Astronomical Journal, 108, 1382

McClure, M. K. 2019, A&A, 632, A32

McClure, M. K., Dominik, C., & Kama, M. 2020, A&A, 642, L15

McKee, C. F. & Ostriker, J. P. 1977, ApJ, 218, 148

McLeod, A. F., Ali, A. A., Chevance, M., et al. 2021, MNRAS, 508, 5425

McLeod, A. F., Dale, J. E., Ginsburg, A., et al. 2015, MNRAS, 450, 1057

McLeod, A. F., Weilbacher, P. M., Ginsburg, A., et al. 2016, MNRAS, 455, 4057

Meaburn, J. 1988, MNRAS, 233, 791

Menten, K., Reid, M., Forbrich, J., & Brunthaler, A. 2007a, A & A, 474, 515

Menten, K. M., Reid, M. J., Forbrich, J., & Brunthaler, A. 2007b, A&A, 474, 515

Mesa-Delgado, A., Núñez-Díaz, M., Esteban, C., et al. 2012, MNRAS, 426, 614

Michel, A., van der Marel, N., & Matthews, B. C. 2021, ApJ, 921, 72

Miotello, A., Kamp, I., Birnstiel, T., Cleeves, L. C., & Kataoka, A. 2023, in ASP Conference Series, Vol. 534, Protostars and Planets VII, ed. S. Inutsuka, Y. Aikawa, T. Muto, K. Tomida, & M. Tamura, 501

Miotello, A., Robberto, M., Potenza, M. A. C., & Ricci, L. 2012, ApJ, 757, 78

Monga, N. & Desch, S. 2014, ApJ, 798, 9

Morbidelli, A., Marrocchi, Y., Ali Ahmad, A., et al. 2024, A&A, 691, A147

Muench, A., Getman, K., Hillenbrand, L., & Preibisch, T. 2008, Star Formation in the Orion Nebula I: Stellar Content

Natta, A., Testi, L., Alcalá, J. M., et al. 2014, A&A, 569, A5

Navarete, F., Damineli, A., Ramirez, A. E., Rocha, D. F., & Almeida, L. A. 2022, MNRAS, 516, 1289

Nisini, B., Antoniucci, S., Alcalá, J. M., et al. 2018, A&A, 609, A87

Nisini, B., Gangi, M., Giannini, T., et al. 2024, A&A, 683, A116

O'Dell, C., Henney, W., Abel, N., Ferland, G. J., & Arthur, S. 2008, The Astronomical Journal, 137, 367

O'Dell, C. R. 2001, , 39, 99

O'Dell, C. R., Abel, N. P., & Ferland, G. J. 2020, ApJ, 891, 46

O'Dell, C. R., Henney, W. J., Abel, N. P., Ferland, G. J., & Arthur, S. J. 2009, The Astronomical Journal, 137, 367

O'Dell, C. R. & Wen, Z. 1994, ApJ, 436, 194

O'Dell, C. R., Wen, Z., & Hu, X. 1993, ApJ, 410, 696

O'Dell, C. R. & Wong, K. 1996, The Astronomical Journal, 111, 846

O'Donnell, J. E. 1994, ApJ, 422, 158

Osterbrock, D. E. 1989, Astrophysics of gaseous nebulae and active galactic nuclei (University Science Books)

Osterbrock, D. E. & Ferland, G. J. 2006, Astrophysics of gaseous nebulae and active galactic nuclei (University Science Books)

Owen, J. E., Clarke, C. J., & Ercolano, B. 2012, MNRAS, 422, 1880

Owen, J. E., Ercolano, B., & Clarke, C. J. 2011, MNRAS, 412, 13

Owen, J. E., Ercolano, B., Clarke, C. J., & Alexander, R. D. 2010, MNRAS, 401, 1415

O'Dell, C. 2001, Publications of the ASP, 113, 29

O'Dell, C. R., Kollatschny, W., & Ferland, G. J. 2017, ApJ, 837, 151

Palla, F. & Stahler, S. W. 1999, ApJ, 525, 772

Parker, R. J. 2020, Royal Society open science, 7, 201271

Pascucci, I., Cabrit, S., Edwards, S., et al. 2023, in ASP Conference Series, Vol. 534, Protostars and Planets VII, ed. S. Inutsuka, Y. Aikawa, T. Muto, K. Tomida, & M. Tamura, 567

Pascucci, I. & Sterzik, M. 2009, ApJ, 702, 724

Peake, T., Haworth, T. J., Aru, M.-L., & Henney, W. J. 2025, MNRAS, 541, 2917

Peeters, E., Habart, E., Berné, O., et al. 2024, A&A, 685, A74

Persson, M. V. 2014

Pfalzner, S., Davies, M. B., Gounelle, M., et al. 2015, Physica Scripta, 90, 068001

Pfalzner, S., Dehghani, S., & Michel, A. 2022, ApJ Letters, 939, L10

Pfalzner, S. & Dincer, F. 2024, ApJ, 963, 122

Picogna, G., Ercolano, B., Owen, J. E., & Weber, M. L. 2019, MNRAS, 487, 691

Piqueras, L., Conseil, S., Shepherd, M., et al. 2017, arXiv e-prints, arXiv:1710.03554

Piralla, M., Villeneuve, J., Schnuriger, N., Bekaert, D. V., & Marrocchi, Y. 2023, Icarus, 394, 115427

Planet formation environments collaboration, Allen, M., Anania, R., et al. 2025, The Open Journal of Astrophysics, 8

Portegies Zwart, S. 2019, A&A, 622, A69

Ramírez-Tannus, M. C., Bik, A., Cuijpers, L., et al. 2023, ApJ, 958, L30

Ramírez-Tannus, M. C., Bik, A., Getman, K. V., et al. 2025, arXiv e-prints, arXiv:2505.06093

Reggiani, M., Robberto, M., Da Rio, N., et al. 2011, A&A, 534, A83

Reggiani, M., Robberto, M., Da Rio, N., et al. 2011, A&A, 534, A83

Reiter, M. & Parker, R. J. 2022, The European Physical Journal Plus, 137, 1071

Ribas, , Bouy, H., & Merín, B. 2015, A&A, 576, A52

Ribas, , Merín, B., Bouy, H., & Maud, L. T. 2014, A&A, 561, A54

Ricci, L., Robberto, M., & Soderblom, D. R. 2008, The Astronomical Journal, 136, 2136

Richling, S. & Yorke, H. W. 2000, ApJ, 539, 258

Rigliaco, E., Natta, A., Randich, S., & Sacco, G. 2009, A&A, 495, L13

Rigliaco, E., Pascucci, I., Gorti, U., Edwards, S., & Hollenbach, D. 2013, ApJ, 772, 60

Robberto, M., Clampin, M., Ligori, S., Paresce, F., & Staude, H. J. 1993, A&A, 280, 241

Robberto, M., Gennaro, M., Da Rio, N., et al. 2024, 960, 49

Robberto, M., Soderblom, D. R., Scandariato, G., et al. 2010, The Astronomical Journal, 139, 950

Scally, A. & Clarke, C. 2001, MNRAS, 325, 449

Schwamb, M. E., Brown, M. E., Rabinowitz, D. L., & Ragozzine, D. 2010, ApJ, 720, 1691

Sellek, A. D., Bajaj, N. S., Pascucci, I., et al. 2024, The Astronomical Journal, 167, 223

Sheehan, P. D., Eisner, J. A., Mann, R. K., & Williams, J. P. 2016, ApJ, 831, 155

Shu, F. H., Johnstone, D., & Hollenbach, D. 1993, Icarus, 106, 92

Siess, L., Dufour, E., & Forestini, M. 2000, A & A, 358, 593

Simon, M. N., Pascucci, I., Edwards, S., et al. 2016, ApJ, 831, 169

Simón-Díaz, S., Herrero, A., Esteban, C., & Najarro, F. 2006, A&A, 448, 351

Skrutskie, M. F., Dutkevitch, D., Strom, S. E., et al. 1990, The Astronomical Journal, 99, 1187

Stolte, A., Brandner, W., Brandl, B., Zinnecker, H., & Grebel, E. K. 2004, The Astronomical Journal, 128, 765

Störzer, H. & Hollenbach, D. 1998, ApJ, 502, L71

Storzer, H. & Hollenbach, D. 1999, ApJ, 515, 669

Testi, L., Birnstiel, T., Ricci, L., et al. 2014, in Protostars and Planets VI (University of Arizona Press)

Tielens, A., Meixner, M., Van der Werf, P., et al. 1993, Science, 262, 86

Trappitsch, R., Boehnke, P., Stephan, T., et al. 2018, ApJ Letters, 857, L15

Tsamis, Y. G., Flores-Fajardo, N., Henney, W. J., Walsh, J. R., & Mesa-Delgado, A. 2013, MNRAS, 430, 3406

Tsamis, Y. G., Flores-Fajardo, N., Henney, W. J., Walsh, J. R., & Mesa-Delgado, A. 2013, MNRAS, 430, 3406

Tsamis, Y. G. & Walsh, J. R. 2011, MNRAS, 417, 2072

Tsamis, Y. G., Walsh, J. R., Vílchez, J. M., & Péquignot, D. 2011, MNRAS, no

Van De Putte, D., Meshaka, R., Trahin, B., et al. 2024, A & A, 687, A86

van der Marel, N. 2023, The European Physical Journal Plus, 138, 225

Van der Werf, P., Stutzki, J., Sternberg, A., & Krabbe, A. 1996, A & A, v. 313, p. 633-648, 313, 633

van Terwisga, S. E. & Hacar, A. 2023, A&A, 673, L2

van Terwisga, S. E., van Dishoeck, E. F., Mann, R. K., et al. 2020, A&A, 640, A27

Vasconcelos, M. J., Cerqueira, A. H., Plana, H., Raga, A. C., & Morisset, C. 2005a, The Astronomical Journal, 130, 1707

Vasconcelos, M. J., Cerqueira, A. H., Plana, H., Raga, A. C., & Morisset, C. 2005b, The Astronomical Journal, 130, 1707

Vicente, S. M. & Alves, J. 2005, A&A, 441, 195

Vicente, S. M. H. 2009, PhD thesis, University of Lisbon, Portugal; European Southern Observatory, Germany

Villenave, M., Ménard, F., Dent, W. R. F., et al. 2020, A&A, 642, A164

Walmsley, C. M., Natta, A., Oliva, E., & Testi, L. 2000, A&A, 364, 301

Weber, M. L., Ercolano, B., Picogna, G., Hartmann, L., & Rodenkirch, P. J. 2020, MNRAS, 496, 223

Weilbacher, P. M., Monreal-Ibero, A., Kollatschny, W., et al. 2015, A&A, 582, A114

Weilbacher, P. M., Palsa, R., Streicher, O., et al. 2020, A&A, 641, A28

Whelan, E. T., Pascucci, I., Gorti, U., et al. 2021, ApJ, 913, 43

Wilhelm, M. J. C., Portegies Zwart, S., Cournoyer-Cloutier, C., et al. 2023, MNRAS, 520, 5331

Williams, J. P. & Cieza, L. A. 2011, Annual Review of A & A, 49, 67

Winter, A. J., Clarke, C. J., Rosotti, G. P., Hacar, A., & Alexander, R. 2019, MNRAS, 490, 5478

Winter, A. J. & Haworth, T. J. 2022, European Physical Journal Plus, 137, 1132

Wolszczan, A. & Frail, D. A. 1992, Nature, 355, 145

Yasui, C., Kobayashi, N., Tokunaga, A. T., & Saito, M. 2014, MNRAS, 442, 2543

Young, E. D. 2007, Earth and Planetary Science Letters, 262, 468

Yurimoto, H. & Kuramoto, K. 2004, Science, 305, 1763

Acknowledgements

Every big climb is easier with support, and I want to thank my loved ones, advisors, friends, and colleagues for lifting me up throughout the various steps that took me here.

To go into the beginning of the PhD, I would like to give my sincerest thanks to Carlo Manara for trusting me with a treasure trove of data, which made these projects possible. His supervision and enthusiasm remained constant throughout each year that followed. Thank you, Carlo, for your bold vision and most of all: for believing in my potential, often beyond what I would've imagined myself (the first half here would've been perfect for a WandaVision pun, wouldn't it?). Being part of the group you brought together was a great honor. I'll never forget that croissant with a reminder to eat, either!

This PhD was supported just as much by Karina, whose encouragement and kind words meant so much to me. Our chats on life, laughs, and conference-ing will always be dear to me. You know I'm beaming with pride about everything you have accomplished! Office E.5.09, Justyn included, was a comfort space for chatter and postdoc wisdom: thank you both.

I acknowledge the helpful exchanges with my brilliant collaborators, both online and at the meetings of our Euro-tour, whose expertise improved this work. Especially Tom, Stefano, Andrew, and Giovanni who have listened to my talks *many* times. I'm grateful to the organizers of these meetings, with Megan in addition to the list above, and to my fellow attending PhD pals.

On the ESO community side: my thanks go to the SPF group and its members across career stages for providing a positive environment to be part of and to learn at. This gratitude also extends to the wider scientific body, whose contributions make this organization the lively, exciting place it is. I acknowledge the efforts and care of Nelma — our guiding light (and with a capybara lamp at that), Adele and Denisa in the day-to-day aspects of our research. I'd also like to mention the valuable opportunity of being part of a master's project in a guiding role — it was great to share this new experience with you, Martina!

My appreciation goes to all who've been there from stressful moments to milestones in Garching & Munich. Thank you, Giulia, for being there to share this experience in all its stages together, I cherish that and our bond! Alice, for your warm welcome from the start, and all the tips and cheerfulness since then. Lara, for your positive presence and kindness, for the trips and memories that I'm so glad to have shared with you. Sreejita, for the heartfelt conversations and checking in with me in the hectic writing period. Cristine, for brightening my time here, I'm feeling truly lucky we had a longer overlap. And also Elena, Silvia, and Claudia — it's been inspiring to be surrounded by so many brilliant women.

This period was more memorable thanks to my friends Josef and Patrie; Stephenie — our paths crossing during this time was a true gift (plus, thank you for the iconic PS work) and Rik; Danny. A special mention to Amedeo, Bibiana and Rita who felt close even if we were based at different countries. Miguel, who has cheered me on the entire academic path. Amanda, who holds the power to turn people into bookworms: I've never read so consistently in my life thanks to the book club you started.

For my family. Tänan oma pere ja lähedasi. Eriti armsaid Kaja ja Rauli, kes on mu suurimad toetajad ja tunnustajad. Aitäh, ema, näitamast et ükskõik kui keeruline elu võib olla, me saame kõigest välja tulla ja seejuures oma huumorimeele säilitada. Aitäh, Raul, näitamast milline on tõeline hoolivus ja oma lähedaste jaoks olemas olemine. Olgu see koju tulek või jutu-

ja naerusessioonid teiega facetime'is, väärtustan seda rohkem, kui oskan sõnades väljendada. Aitäh, Enelin: olles välismaal, meie mitmetunnised kõned ja sinu julgustavad sõnad on alati tujutõstjad. Aitäh nii sulle, Andole, Hannale: te ei hoia toetavate sõnadega kunagi tagasi. Olen teie üle uhked ja hindan teid väga!

Next to all of the science, I've been supported by Greg, which made a world of difference. If I could issue an honorary doctorate for you, I definitely would — I'd like to put in that category of awards for supportive partners. You've come along on the research rollercoaster and been the backbone of these years, someone I could always count on. There aren't enough words to thank you.

I also want to acknowledge the friends who have been cheering me on from distance, and the friends with whom I can always pick up from where we left off, wherever we meet. To the online community: each kind comment and message has been uplifting and reminded me of the bigger picture of doing research. Thanks for coming along on the journey!